Max-Planck-Institut für Meteorologie
*Max Planck Institute for Meteorology*

MAX-PLANCK-GESELLSCHAFT

IMPRS

# Ocean Tides and the Earth's Rotation - Results of a High-Resolving Ocean Model forced by the Lunisolar Tidal Potential

Philipp Weis

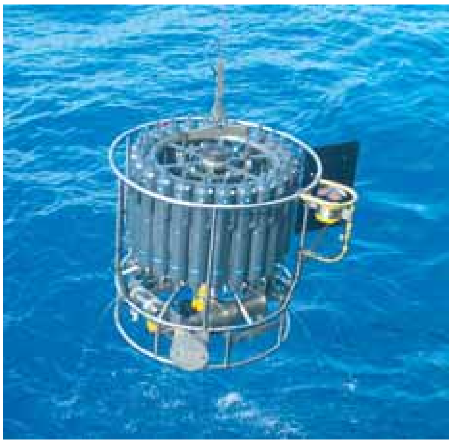

Berichte zur Erdsystemforschung 36/2006

*Reports on Earth System Science*

## Hinweis

Die Berichte zur Erdsytemforschung werden vom Max-Planck-Institut für Meteorologie in Hamburg in unregelmäßiger Abfolge herausgegeben.

Sie enthalten wissenschaftliche und technische Beiträge, inklusive Dissertationen.

Die Beiträge geben nicht notwendigerweise die Auffassung des Instituts wieder.

Die "Berichte zur Erdsystemforschung" führen die vorherigen Reihen "Reports" und "Examensarbeiten" weiter.

## *Notice*

*The Reports on Earth System Science are published by the Max Planck Institute for Meteorology in Hamburg. They appear in irregular intervals.*

*They contain scientific and technical contributions, including Ph. D. theses.*

*The Reports do not necessarily reflect the opinion of the Institute.*

*The "Reports on Earth System Science" continue the former "Reports" and "Examensarbeiten" of the Max Planck Institute.*

## Anschrift / Address

Max-Planck-Institut für Meteorologie
Bundesstrasse 53
20146 Hamburg
Deutschland

Tel.: +49-(0)40-4 11 73-0
Fax: +49-(0)40-4 11 73-298
Web: www.mpimet.mpg.de

## Layout:

Bettina Diallo, PR & Grafik

Titelfotos:
vorne:
Christian Klepp - Jochem Marotzke - Christian Klepp
hinten:
Clotilde Dubois - Christian Klepp - Katsumasa Tanaka

Berichte zur Erdsystemforschung 36/2006

# Ocean Tides and the Earth's Rotation - Results of a High-Resolving Ocean Model forced by the Lunisolar Tidal Potential

Dissertation zur Erlangung des Doktorgrades der Naturwissenschaften
im Departement Geowissenschaften der Universität Hamburg
vorgelegt von

Philipp Weis
aus Heidelberg
Hamburg 2006

*Reports on Earth System Science* 36/2006

ISSN 1614-1199

Philipp Weis
International Max Planck Research School on Earth System Modelling
Max-Planck-Institut für Meteorologie
Bundesstrasse 53
20146 Hamburg
Germany

Universität Hamburg
Zentrum für Meeres- und Klimaforschung
Institut für Meereskunde
Bundesstr. 53
20146 Hamburg
Germany

Als Dissertation angenommen
vom Departement Geowissenschaften der Universität Hamburg

auf Grund der Gutachten von
Prof. Dr. Jürgen Sündermann
und
Prof. Dr. Wilfried Zahel
Hamburg, den 1. Dezember 2006
Prof. Dr. Kay-Christian Emeis
Leiter des Departements für Geowissenschaften

ISSN 1614-1199

# Ocean Tides and the Earth's Rotation - Results of a High-Resolving Ocean Model forced by the Lunisolar Tidal Potential

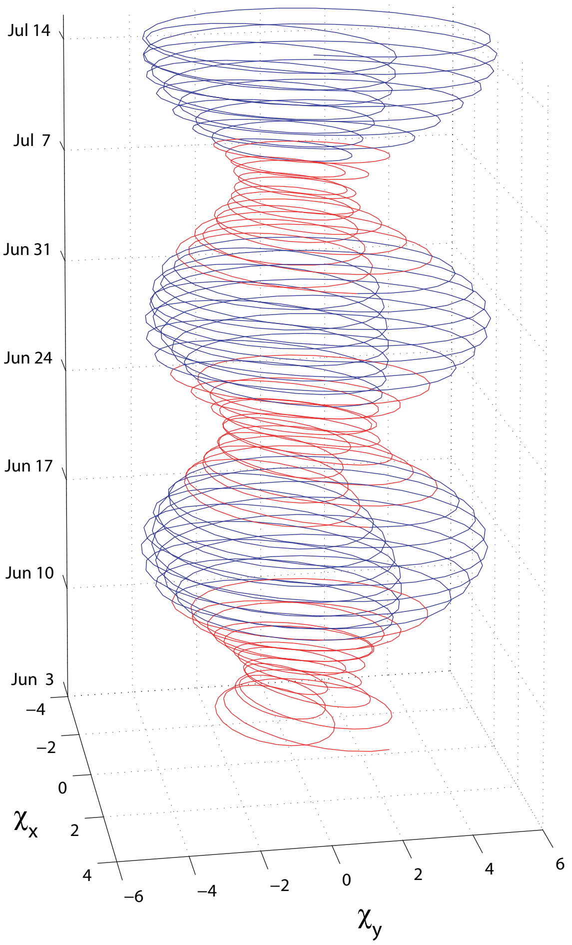

## Philipp Weis

Hamburg 2006

# Abstract

The Tidal Model forced by Ephemerides (TiME) has been developed. TiME is a hydrodynamic, global ocean model based on shallow water equations incorporating the complete lunisolar tidal potential of second degree. The spatial resolution has been chosen to be 5 minutes globally (2 - 10 kilometres). Tidal currents and sea surface elevations are calculated in real-time as opposed to most existing tidal models that utilise selected partial tides. The application of complete forcing and non-linear model equations allows for interactions between partial tides and, consequently, the generation of shallow-water tides. The results of the real-time simulations have been divided into partial tides through harmonic analysis in order to compare the results of this study with others. TiME has been evaluated with a set of pelagic measurements of the sea surface elevations. Correlation coefficients are higher than 0.88 for all partial tides considered, showing that the tidal oscillation system is well-captured by this new modelling approach.

The model's high horizontal resolution reveals a detailed picture of tidal propagation on shelf areas worldwide where non-linearities are shown to be most significant. Comparisons of the old partial tide approach with the new approach with complete forcing show that amplitude values of selected partial tides can locally differ by up to 50%. For the first time, global charts of a selection of non-linear shallow-water tides were predicted by an ocean model for both sea surface elevations and tidal currents.

The total energy dissipated by the complete tidal oscillation system has been calculated to be about 4.8 Terawatts (TW). The contribution of ocean tides to tidal friction, which results in an acceleration of lunar angular velocity, has been estimated to be about 4.1 TW. This value lies within the range of available measurements. Most recent studies, however, agree on a lower value of 3 TW.

TiME can calculate the contribution of the entire range of frequencies of the ocean tides to the earth rotation parameters (ERP). This further leads to a novel determination of the oceanic tidal angular momentum (OTAM) taking into account the entire tidal spectrum. The improved description of the ocean tides' influence on OTAM and ERP have been assessed. Comparisons with measurements included tidal constituents which were not investigated by a numerical model study before and show good to excellent agreement. The effects on ERP of some additional astronomical partial tides as well as a selection of shallow-water tides not yet included in any measurement or modelling study have also been calculated.

# Zusammenfassung

Im Rahmen der vorliegenden Doktorarbeit wurde das globale hydrodynamische Ozeanmodell ”TiME” (Tidal Model forced by Ephemerides) entwickelt. Es basiert auf nichtlinearen Flachwassergleichungen und wird von dem vollständigen lunisolaren Potential zweiten Grades angetrieben; seine räumliche Gitterauflösung beträgt weltweit 5 Minuten (2 - 10 Kilometer). Gezeitenströme und Meeresspiegelauslenkungen werden somit in Echtzeit simuliert. Dieser neue Ansatz steht damit im Gegensatz zu den meisten existierenden Gezeitenmodellen, welche mit ausgewählten Partialtiden angetrieben werden. Die Anwendung des vollständigen Antriebs in Verbindung mit den nichtlinearen Termen der Modellgleichungen ermöglicht es, Wechselwirkungen zwischen einzelnen Partialtiden darzustellen und folglich auch nichtlineare Seichtwassertiden abzubilden. Ergebnisse dieser Echtzeitsimulationen wurden mittels harmonischer Analyse in Partialtiden zerlegt, um sie einem Vergleich mit Ergebnissen anderer Studien unterziehen zu können. Zur Einschätzung der Güte der Modellergebnisse wurde ein Standard-Datensatz pelagischer Wasserstandsmessungen herangezogen. Korrelationskoeffizienten mit Werten über 0.88 für alle untersuchten Partialtiden zeigen, dass das Schwingungssystem der Ozeangezeiten durch den neuen Modellansatz gut abgebildet wird.

Die hohe horizontale Modellauflösung gewährt einen detaillierten Einblick in die Ausbreitung von Gezeitenströmen in den Randmeeren weltweit. Eben diese Schelfmeere sind stark von Nichtlinearitäten geprägt. Vergleiche von Ergebnissen des alten Partialtidenantriebs mit dem neuen vollständigen Antrieb zeigen, dass die Amplitudenwerte der gezeitenbedingten Meeresspiegelschwankungen je nach Modellansatz lokal um bis zu 50% voneinander abweichen. Erstmalig wurden globale Strömungs- und Auslenkungsfelder einiger ausgewählter nichtlinearer Seichtwassertiden von einem numerischen Ozeanmodell berechnet.

Die durch das vollständige Schwingungssystem der Gezeiten insgesamt vernichtete Energie wurde mit etwa 4,8 Terawatt (TW) berechnet. Der Anteil der Ozeangezeiten an der Gezeitenreibung, welche beschleunigend auf die Mondumlaufbahn wirkt, wurde auf 4,1 TW geschätzt. Dieser Wert liegt innerhalb der Spanne bekannter Messwerte. Neueste Messungen stimmen jedoch eher in einem vergleichweise niedrigeren Wert von ungefähr 3 TW überein.

Mit TiME lässt sich der Einfluss der gesamten Spanne von hoch- bis niederfrequenten Tiden auf die Erdrotationsparameter (ERP) berechnen. Das führt zu einer neuen Bewertung der durch Ozeangezeiten verursachten Drehimpulse (oceanic tidal angular momentum, OTAM), welche zeitgleich das gesamte Gezeitenspektrum berücksichtigt. Die verfeinerte und erweiterte Beschreibung der Einflüsse von Ozeangezeiten auf OTAM und ERP wurde abgeschätzt und bewertet. In den Vergleichen mit Messungen wurden auch Partialtiden berücksichtigt, welche bislang noch nicht von numerischen Modellen beschrieben wurden. Sie weisen zumeist gute bis hervorragende Übereinstimmungen auf. Die Einflüsse auf die ERP einiger zusätzlicher astronomischer Partialtiden sowie einer Auswahl von Seichtwassertiden, welche bislang noch in keinerlei Modell- oder Messstudien Erwähnung fanden, wurden ebenfalls berechnet.

# Contents

# Chapter 1

# Introduction

Ocean tides are forced by the gravitation of the moon and sun. The moon's orbit around the earth and the earth's orbit around the sun determine where, how strong and in which direction these tidal forces act on the water masses of the oceans. The respective orbits are characterised by a number of strict periodicities with different frequencies. A dynamic oscillation system of tidal currents and elevations forms where favourable basin dimensions produce pronounced resonance.

These periodic displacements of water masses lead to variations in the rotational behaviour of the earth. Both sea surface elevations and currents have their effect on the earth's rotation: elevations by changes in the oceanic tensor of inertia; currents by their motion relative to the earth's body-fixed frame. These variations result in changes in the earth's angular velocity and its axis orientation.

Additionally, a long-term trend can be observed as a secular deceleration of the earth's rotation. It is related to an acceleration of the mean angular velocity of the moon which eventually results in an increase of the distance of the moon from the earth. This effect is known as tidal friction. It results from tidal energy which is dissipated in the earth system due to frictional processes.

## 1.1 Measurements

With the improvements of modern geodetic measurement techniques, changes in the sea surface elevation and the earth's rotation can now be determined with an accuracy of microseconds and centimetres and are approaching nanoseconds and millimetres. Several studies have focused on the determination of the aforementioned changes in the earth's rotation due to tides from very long baseline interferometry (VLBI), lunar laser ranging (LLR) and global positioning system (GPS) and have calculated the effect of up to 40 partial tides on the earth rotation (e.g. Sovers et al., 1993; Herring and Dong, 1994; Gipson, 1996; Rothacher et al., 1998; Chapront et al., 2002).

The amount of available satellite data has been increasing over the years. Satellite altimetry studies are now moving part of their focus towards selected shelf areas, such as th North Sea and the Patagonian Shelf. First studies have demonstrated the importance of non-linearities within the dynamics of ocean tides in these areas of shallow water depth (e.g. Andersen, 1999).

## 1.2 Modelling Approaches

Theoretical studies have been conducted with the help of numerical ocean tide models in order to better understand the physical dynamics that lead to these variations. Seiler (1991) calculated variations in the oceanic tidal angular momentum (OTAM) with an ocean tide model of 1°-resolution globally forced by selected partial tides. Gross (1993) has utilised these OTAM to calculate their effect on the earth's rotation.

As measurements of the sea surface elevations (pelagic and derived from satellite altimetry) have become more abundant in recent years, ocean tide models assimilating data have been developed (e.g. Egbert et al., 1994; Zahel, 1995). The predictions of the sea surface elevation due to ocean tides have been improved dramatically with this approach (Shum, 1997). The data assimilation process compensates the deficiency in the description of the physical processes in the model and can be characterised by dynamical residuals (Zahel, 1995). These have been shown to be of dissipative nature and in many cases take large values where bottom topography is not properly resolved due to the relatively coarse spatial resolution of the model (Zahel et al., 2000). Some of these studies have also focused on the determination of OTAM and calculated the tides effect on the earth's rotation (e.g. Desai, 1996; Chao and Ray, 1997; Kantha et al., 1998; Zahel et al., 2000) and tidal friction (e.g. Egbert and Ray, 2000).

An alternative approach has been developed by forcing a general circulation model with the full lunisolar tidal potential rather than just single partial tides (Thomas, 2001). Such an approach allows for interactions of tidal currents with other ocean currents. Seitz (2004) further took the influence of the solid earth into account and developed a dynamic earth system model for the investigation of the earth's rotation which also allows for feedbacks between the respective components.

## 1.3 Objectives and Outline of this Study

The objective of this study is to develop an unconstrained ocean model in order to investigate the complete effect of ocean tides on the earth's rotation. To this end, the position of the moon and sun (ephemerides) are calculated to force an ocean model with their tidal potential. This leads to real-time simulations.

As the oscillation system of ocean tides strongly depends on the topography of the oceans, the model resolution has been chosen to be as high as computationally feasible. A maximum resolution of 1/12 of a degree (5 minutes) has been used for the experiments. The actual distance between two grid points ranges from 2 to 10 kilometres. The model also includes the Arctic Ocean which is often neglected in other model approaches.

The set-up of the newly developed model enables a unique feature by describing non-linearities in ocean tide dynamics. These non-linearities are due to interactions between partial tides. The novel approach with the forcing by the complete lunisolar tidal potential presented in this study includes all partial tides simultaneously. The non-linear terms of the model equations are most influential in shallow waters which are resolved by the model due to its high spatial resolution. Throughout this study, special attention will be turned to the significance of these non-linearities.

The model will be presented in Chapter 2 together with a description of the methodology for harmonic analysis, statistics and calculation of angular momentum and earth rotational parameters. Chapter 3 will describe the improvements implemented into the precursor ocean tide model (Seiler, 1989) in order to ensure the feasibility to perform simulations with the 5' resolution and evaluates the model results with measurements.

Results of the tidal oscillation system as simulated by the new model will be presented in Chapter 4 and will also have a focus on selected regions in order to illustrate the non-linearities captured by the new approach. Chapter 5 describes the angular momenta calculated from the simulations and discusses the tides' effect on the earth's rotation.

Chapter 6 summarises the main findings and presents an outlook for current and future studies and developments.

# Chapter 2

# Model Description and Methods of Analysis

A global ocean tide model, the Tidal Model forced by Ephemerides (TiME), has been developed. Its major part consists of a vertically-integrated barotropic ocean module (Section 2.1). It is forced by an astronomic module calculating the gravitational potential (Section 2.2) and accompanied by a geodetic module calculating instantaneous angular momentum budgets (Section 2.3). TiME can be run with the user's choice of either a single selected partial tide or the complete lunisolar tidal potential calculated from the exact position of the moon and sun (ephemerides) (Fig. 2.1). This second option represents "real-time" simulations.

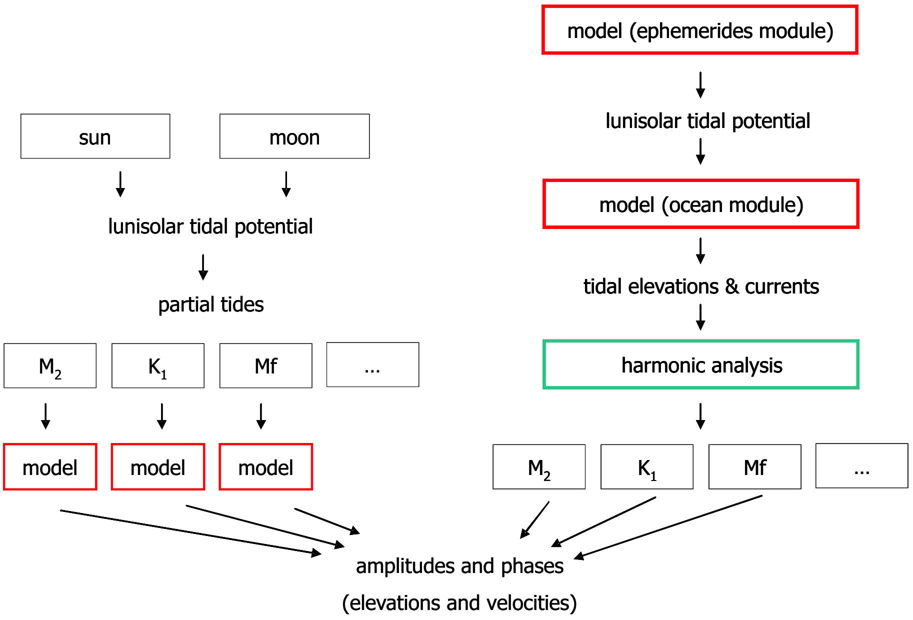

Figure 2.1: Flow diagram of the two optional set-ups of TiME. The left path represents the classical partial tide forcing. The right path is the novel approach of the complete forcing with subsequent harmonic analysis.

Until now, most research on ocean tides has been done using only partial tide forcing. Thus, the results of simulations utilising the complete forcing have to be post-processed so that the results are comparable with the results from other studies. The amplitude and phase values of selected partial tides are derived from the time series of the real-time simulations through a harmonic analysis (Section 2.4).

The two model set-ups are presented in Figure 2.1. For the traditional forcing (left path), the lunisolar tidal potential is divided into partial tides, each one describing a certain aspect of the orbits of moon or earth. They are defined by their respective astronomical arguments or Doodson coefficients which describe the frequency of each partial tide (see Appendix A.2). A description of the theoretical derivation of partial tides through harmonic analysis can be found in Bartels (1957). The resulting elevations and velocities are attributed to the period of the specific partial tide and can be represented by amplitude and phase values. Results which relate to partial tides will be referred to as ”frequency-domain”.

The path on the right-hand side of Figure 2.1 characterises the novel approach with complete forcing which is the focus of this work. With the newly implemented ephemerides module (Section 2.2.2), the model calculates the position of the tide-generating bodies, the moon and sun, determines their complete tidal potential of second degree (see Section 2.2) and uses this total forcing to drive the ocean module of TiME. As these real-time results can only be represented in the form of time-series, they will be referred to as belonging to the ”time-domain”. By extracting the frequencies of certain partial tides from these time-series through a harmonic analysis, the results of the real-time forcing can be transferred from the time-domain to the frequency-domain.

The methods used for comparing model results with measurements are described in Section 2.5. The methodology for investigating the tides’ influence on the earth rotation parameters can be found in Section 2.6.

## 2.1 Ocean Module

The main part of TiME is a barotropic ocean model based on the Navier-Stokes-equations. The equations of motion and continuity define the horizontal velocities $u$ (zonal) and $v$ (meridional) in $\frac{m}{s}$ and the sea surface elevation $\zeta$ in $m$ (Zahel, 1970; Seiler, 1989).

$$\begin{aligned}\frac{\partial u}{\partial t} - f \cdot v = \frac{\gamma}{a\cos\phi}\frac{\partial \Phi_x}{\partial \lambda} - \left(\frac{u}{a\cos\phi}\frac{\partial u}{\partial \lambda} + \frac{v}{a}\frac{\partial u}{\partial \phi}\right) - \\ -\frac{g'}{a\cos\phi}\frac{\partial \zeta}{\partial \lambda} - \frac{r}{H}u\sqrt{u^2+v^2} + R_\lambda\end{aligned} \tag{2.1}$$

$$\begin{aligned}\frac{\partial v}{\partial t} + f \cdot u = \frac{\gamma}{a}\frac{\partial \Phi_y}{\partial \phi} - \left(\frac{u}{a\cos\phi}\frac{\partial v}{\partial \lambda} + \frac{v}{a}\frac{\partial v}{\partial \phi}\right) - \\ -\frac{g'}{a}\frac{\partial \zeta}{\partial \phi} - \frac{r}{H}v\sqrt{u^2+v^2} + R_\phi\end{aligned} \tag{2.2}$$

$$\frac{\partial\zeta}{\partial t} - \left(\frac{\partial(H \cdot u)}{a\cos\phi \cdot \partial\lambda} + \frac{\partial(H \cdot v)}{a \cdot \partial\phi}\right) = 0 \tag{2.3}$$

These include the Coriolis parameter $f = 2\Omega\sin\phi$, the mean angular velocity of the earth $\Omega = 7.292 \times 10^{-5}\,\frac{rad}{s}$, the mean radius of the earth $a$, the bottom friction coefficient $r$ and the total depth of the water column $H = d + \zeta$ (where $d$ is the undisturbed depth). The influence of the tides of the solid earth on the tidal potential is defined by the Love numbers $k = 0.302$ and $h = 0.612$ resulting in the factor $\gamma$.

$$\gamma = 1 + k - h \tag{2.4}$$

The tidal forcings $\Phi_x$ and $\Phi_y$ are calculated by the astronomic module of TiME and will be discussed in Section 2.2.

The effect of load and self-attraction of water masses $\Phi_{LSA}$ is taken into account in a parameterised form (Accad and Pekeris, 1978) defined as

$$\Phi_{LSA} = g \cdot \epsilon \cdot \zeta \tag{2.5}$$

eventually leading to the “reduced gravity” $g'$

$$g' = (1 - \epsilon) \cdot g \tag{2.6}$$

referring to the gravitational acceleration $g = 9.806\frac{m}{s^2}$. Values of $\epsilon$ are in the range of about 0.08 to 0.12 (Parke, 1982). Calculating the full LSA-effect (e.g. Zahel, 1978) is very expensive in computational time. Müller (2003) gives a detailed description of the computational requirements for the calculation of normal modes of eigen-oscillations of a global 1°-ocean when including the full effect. It can be expected that a similar computational effort would also be needed for calculations of ocean tides. As Chapter 3 will illustrate, TiME is at the upper limit of computational feasibility. Fortunately, experiments with the parameterised form of the LSA-effect have shown that this approach is a good approximation (Parke, 1982; Seiler, 1989; Müller, 2003). This study focuses on the implications of ocean tides and the earth rotation on a global scale and the parameterised LSA-effect can be regarded as sufficient for this purpose.

Turbulent effects are prescribed in the eddy-viscosity terms $R_\lambda$ and $R_\phi$.

$$R_\lambda = \frac{A_H}{a^2}\left[\frac{\partial^2 u}{\cos\phi \cdot \partial\lambda^2} + \frac{\partial^2 u}{\partial\phi^2} - \tan\phi\frac{\partial u}{\partial\phi} - (1 + \tan^2\phi)u - 2\tan\phi\frac{\partial v}{\partial\lambda}\right] \tag{2.7}$$

$$R_\phi = \frac{A_H}{a^2}\left[\frac{\partial^2 v}{\cos\phi \cdot \partial\lambda^2} + \frac{\partial^2 v}{\partial\phi^2} - \tan\phi\frac{\partial v}{\partial\phi} - (1 + \tan^2\phi)v - 2\tan\phi\frac{\partial u}{\partial\lambda}\right] \tag{2.8}$$

The eddy-viscosity-coefficient $A_H$ will be discussed in Section 3.5.

The ocean module was taken in large parts from the partial tide model of Seiler (1989) which is based on the equations of Zahel (1977) (Equations 2.1 - 2.3) and utilises a semi-implicit algorithm as described in Backhaus (1983). The resolution has been changed from the original one degree (Seiler, 1989) to a series of higher resolving versions. The user can now choose between resolutions of 20, 15, 10 or 5 minutes based on either the GEBCO (IOC et al., 2003) or

ETOPO topographies (NOAA, 1988). Although the simulations for this study were performed on the high-performance computer of the DKRZ (Deutsches Klimarechenzentrum) the 5 minute resolution version of TiME is still at the upper limit of manageable run times. Chapter 3 will describe improvements implemented for the model performance.

The equations of Seiler (1989) were reformulated in a slightly different semi-implicit numerical scheme (Backhaus, 1985) which has the general form

$$\begin{pmatrix} U \\ V \end{pmatrix}^{n+1} = R_1 \cdot \begin{pmatrix} U \\ V \end{pmatrix}^{n} - R_2 \cdot g' \cdot \begin{pmatrix} \underline{\zeta}_x \\ \underline{\zeta}_y \end{pmatrix}^{n+\frac{1}{2}} + \Delta t \cdot \begin{pmatrix} X \\ Y \end{pmatrix} \tag{2.9}$$

with the Coriolis rotation matrices $R_1$ and $R_2$.

$$R_1 = \begin{pmatrix} \alpha & \beta \\ -\beta & \alpha \end{pmatrix} \quad , \quad R_2 = \frac{1}{f} \cdot \begin{pmatrix} \beta & \gamma \\ -\gamma & \beta \end{pmatrix}$$

The index $n$ refers to the former time-step, $n+1$ to the following and $n+\frac{1}{2}$ to the intermediate time-step of the semi-implicit scheme. The rotation matrices are defined by $\alpha = \cos(f\Delta t)$, $\beta = \sin(f\Delta t)$ and $\gamma = 1 - \alpha$. The terms $X$ and $Y$ include the remaining parts of Equations 2.1 and 2.2. $\underline{\zeta}_x$ and $\underline{\zeta}_y$ represent the meridional and zonal derivatives, respectively.

The main difference between the algorithms of Backhaus (1983) and Backhaus (1985) is that now the pressure gradient is also included in the Coriolis rotation (matrix $R_2$). Note that earlier the Coriolis rotation was defined by $\beta = f$ and that the $\alpha$-term of $R_1$ was not included (Equations 2.1 and 2.2). The advantages of the new scheme will be illustrated in Section 3.1 and the full formulation of the difference equations can be found in Appendix A.1.1.

## 2.2 Astronomic Module

Ocean tides mainly develop due to the gravitational forces of the moon and sun and can be formulated as the second degree astronomical tidal potential $V_2$ (Bartels, 1957):

$$\begin{aligned} V_2 = G(\varrho) \cdot \left(\frac{c}{R}\right)^3 \cdot \big[ & (1 - 3\sin^2\delta)(1 - 3\cos^2\phi) - \\ & \sin(2\phi)\sin(2\delta)\cos\tau + \\ & \cos^2\phi\cos^2\delta\cos(2\tau) \big] \end{aligned} \tag{2.10}$$

where $G(\varrho)$ is the gravitational constant, $\varrho = 6371.221$ km the mean radius of the earth, $R$ the geocentric distance, $c$ the greater half axis of the orbit, $\delta$ the declination, and $\phi$ the geographical latitude. The local hour angle $\tau$ is related to the right ascension $\alpha$ of the respective celestial body through

$$\tau = T_{sid} - \alpha = T_{Gsid} + \lambda - \alpha \tag{2.11}$$

where $\lambda$ is the geographical longitude, $T_{sid}$ the local sidereal time and $T_{Gsid}$ the Greenwich sidereal time. For the lunar tidal potential, the gravitational constant is given with $G(\varrho) = 26206\frac{cm^2}{s^2}$ and the solar tidal potential is $G_S(\varrho) = 0.46051 \cdot G(\varrho)$ (Bartels, 1957).

The three terms of Equation 2.10 represent different groups of spherical harmonics and define the tidal bands:

1. the zonal term reflecting the long-period tides, i.e. fortnightly to annual;
2. the tesseral term describing the band of diurnal tidal constituents; and
3. the sectorial term comprising the semi-diurnal tides.

From Equation 2.10 there are now two approaches for forcing an ocean tide model, both of which are options within TiME. The traditional forcing utilises single partial tides (Section 2.2.1) whereas real-time forcing incorporates the full lunisolar tidal potential (Section 2.2.2).

### 2.2.1 Partial Tide Forcing

Each of the three tidal bands from Equation 2.10 can be broken up into partial tides. The equation for the partial tide forcing reads

$$\Phi(\lambda, \phi, t) = k_{pt} G_m(\phi) \cos(\sigma_{pt} t + m\lambda) \tag{2.12}$$

with the tidal frequency $\sigma_{pt}$ and a specific constant for any partial tide $k_{pt}$. The zonal wavenumber $m$ is determined by the respective tidal band ($m = 0$ for long-period, $m = 1$ for diurnal and $m = 2$ for semi-diurnal tides). The geodetic function $G_m(\phi)$ is given by

$$G_0(\phi) = G \cdot \left( \frac{3}{2} \cos^2(\phi) - 1 \right) \ , \quad G_1(\phi) = G \cdot \sin(2\phi) \ , \quad G_2(\phi) = G \cdot \cos^2(\phi).$$

The main advantage of using partial tides is the characteristics of fixed periods. Once the ocean tide model has adjusted to the constantly perturbing force, e.g. the $M_2$-tide, the system will respond in the exact same way every subsequent period. It is straightforward to perform such simulations and the analyses. In remote sensing and field campaigns, the fixed periods of the partial tides allow the most significant tides to be extracted from collected series of sea surface elevation measurements.

### 2.2.2 Complete Lunisolar Forcing

In order to perform real-time simulations with the complete lunisolar tidal potential, the exact positions of the moon and sun with respect to the centre of the earth have to be known. The module for the complete lunisolar forcing utilised in TiME has been taken from Thomas (2001) and Hellmich (2003) where a detailed description of the theory, the computational calculations and a thorough validation of the module are provided.

The module independently describes the orbits of both the moon and earth according to an algorithm based on fundamental angles. Hellmich (2003) discusses the advantages of this algorithm compared with an alternative one based on Kepler's orbital elements by evaluating the results with the data-set DE200 of numerical ephemerides provided by the Jet Propulsion Laboratory (JPL). Celestial coordinates are formulated in an equatorial system with the earth as its centre and an equatorial plane spanning the x- and y-directions and the earth's axis defining the

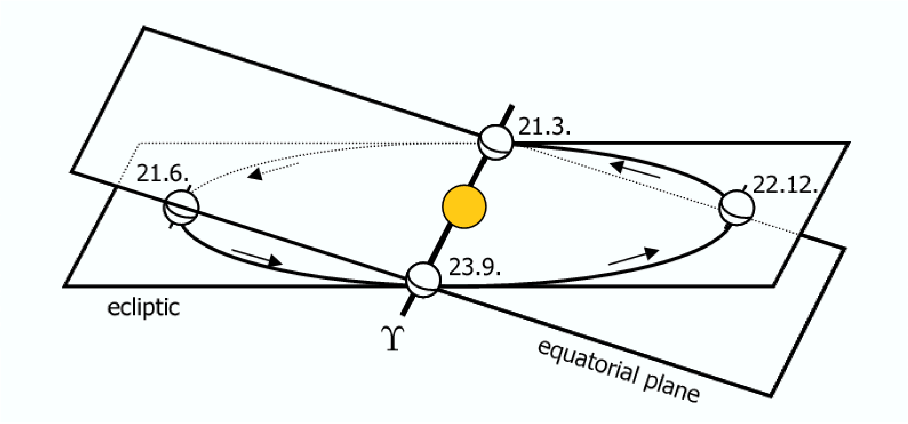

Figure 2.2: The ecliptic is defined by the earth's orbit around the sun; the equatorial plane by the earth's equator, i.e. normal to the axis of the earth's rotation. The intersection of these planes marks the line between the autumnal and vernal equinox. The latter is also known as the Aries point ♈ and is the reference point for the right-ascension $\alpha$ (see Figure 2.3) (after Montenbruck, 1987).

z-direction (Fig. 2.2). The position of any celestial body is then perfectly defined by its declination, right ascension and actual distance (Fig. 2.3). The earth's rotation is taken into account through the local hour angle (Equation 2.11).

With the ephemerides module defining these four values for both the moon and sun for every model time-step the complete tidal forcing on any point on the globe can be calculated with Equation 2.10 directly. As TiME is discretised on a spherical global Arakawa-C grid (Arakawa and Lamb, 1977), the potential has to be divided into a zonal and a meridional component. The tidal acceleration as computed in the module (Bartels, 1957; Hellmich, 2003) reads

$$\begin{aligned}\Phi_x(\phi,\lambda,t) = -\frac{G(\varrho)}{\varrho}\cdot\left(\frac{c}{R}\right)^3\cdot\Big[&\sin(2\phi)(1-3\sin^2\delta)+\\ &2\cos(2\phi)\sin(2\delta)\cos\tau+\\ &\sin(2\phi)\cos^2\delta\cos(2\tau)\Big]\end{aligned} \tag{2.13}$$

$$\begin{aligned}\Phi_y(\phi,\lambda,t) = 2\cdot\frac{G(\varrho)}{\varrho}\cdot\left(\frac{c}{R}\right)^3\cdot\big[&\sin\phi\sin(2\delta)\sin\tau-\\ &\cos\phi\cos^2\delta\cos(2\tau)\big]\,.\end{aligned} \tag{2.14}$$

The advantage of the full forcing is that all partial tides from the second degree tidal potential are included simultaneously and thus can be regarded as representing the complete dynamics. This also allows for non-linear interactions between partial tides which leads to the formation of shallow-water tides (see Chapter 4.3). These are not directly forced by the lunisolar tidal potential. They mainly form in areas of low water depth where the non-linear terms of the

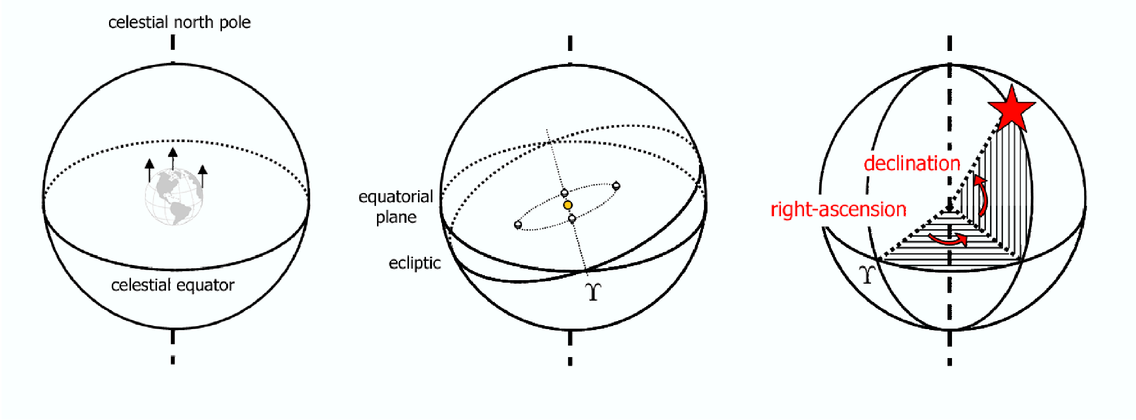

Figure 2.3: The position of the celestial bodies moon and sun have to be formulated in relation to the spherical notation of the earth, i.e. in relation to $\phi$ and $\lambda$. Within an imaginary sphere with infinite radius around the earth all vectors pointing north will meet at the celestial north pole (left). Inserting Figure 2.2 into this celestial sphere (where the equatorial plane intersects with the celestial equator) defines the position of $\Upsilon$ and the ecliptic (middle). The right-ascension $\alpha$ describes the angle from $\Upsilon$ along the celestial equator and the declination $\delta$ the angle along the great circle towards the celestial north pole (right) (after Struve, 1962).

shallow-water equations in TiME gain importance in comparison with the open ocean. By adding or subtracting the astronomical arguments of the partial tides involved, the resulting frequency of the respective shallow-water tide can be determined. Any combination of partial tides is possible (see Appendix A.2). The most significant ones are the fourth-diurnal ”compound tides” which result from the addition of two semi-diurnal tides, e.g. the $MS_4$-tide results from interactions of $M_2 + S_2$. The interaction of the $M_2$ with itself results in the special case of a compound tide, the ”overtide” $M_4$.

## 2.3 Geodetic Module

The geodetic module calculates the kinetic and potential energy within the system, the oceanic tidal angular momentum (OTAM, Section 2.3.1), and instantaneous angular momentum budgets (IAMB, Section 2.3.2).

### 2.3.1 Oceanic Tidal Angular Momentum

Sea surface elevations and ocean currents both affect the oceanic angular momentum. Sea surface heights cause variations in the oceanic tensor of inertia and therefore directly influence the earth’s rotational behaviour (rotational angular momentum). The effect of the ocean currents is due to motion relative to the body-fixed frame (relative angular momentum).

The oceanic tidal angular momentum can be written as (Seiler, 1991):

$$\vec{M} = \Theta \cdot \vec{\omega} + \vec{M}_{rel} \tag{2.15}$$

where $\Theta$ is the oceanic tensor of inertia and $\vec{\omega}$ the rotation vector of the earth. Formulated on a body-fixed reference frame with $x$ and $y$ spanning the equatorial plane and $z$ being the axial component this leads to:

$$M_x = -\Omega\, a^2 \int_A \zeta \cos\phi \sin\phi \cos\lambda \; dA + a \int_A H \,(v \sin\lambda - u \sin\phi \cos\lambda)\, dA \tag{2.16}$$

$$M_y = -\Omega\, a^2 \int_A \zeta \cos\phi \sin\phi \sin\lambda \; dA - a \int_A H \,(v \cos\lambda - u \sin\phi \sin\lambda)\, dA \tag{2.17}$$

$$M_z = \Omega\, a^2 \int_A \zeta \cos^2\phi \; dA + a \int_A H u \cos\phi \; dA. \tag{2.18}$$

For real-time simulations with the complete lunisolar forcing, instantaneous values can be calculated (time-domain). This approach, however, does not provide closed periods. OTAM can also be recalculated after harmonic analysis (Section 2.4) for extracted partial tides (frequency-domain).

### 2.3.2 Instantaneous Angular Momentum Budgets

For the investigation of the instantaneous angular momentum budgets, the balance equations of angular momentum can be formulated as (Seiler, 1991):

$$\frac{d\,\vec{M}_{rel}}{dt} + \frac{d\,\vec{M}_{\Theta}}{dt} + \Omega \times M_{rel} \; = \vec{L}_{rel} + \vec{L}_{cor} = -\left(\vec{L}_{pr} + \vec{L}_{tid} + \vec{L}_{fr}\right) \tag{2.19}$$

where $\vec{L}_{rel}$ and $\vec{L}_{cor}$ describe the torques due to acceleration and Coriolis force. $\vec{L}_{pr}$ denotes the pressure torque, $\vec{L}_{tid}$ the tidal torque and $\vec{L}_{fr}$ the frictional torque.

As the current algorithm also applies the Coriolis rotation to the pressure gradient term ($R_2$ of Equation 2.9), Equation 2.19 should be slightly reformulated as

$$\vec{L}_{rel} + \vec{L}_{cor} = -\left(\vec{L}_{pc} + \vec{L}_{pr} + \vec{L}_{tid} + \vec{L}_{fr}\right) \tag{2.20}$$

where $\vec{L}_{pc}$ includes the "rotated part" of the pressure gradient. However, $\vec{L}_{pc}$ is negligibly small compared to the remaining torques making it irrelevant whether it should be attributed to $\vec{L}_{cor}$ or $\vec{L}_{pr}$. Similarly, a small quantity of $\vec{L}_{rel}$ would, in contrast with Seiler (1991) now be attributed to $\vec{L}_{cor}$ due to the $\alpha$-terms of $R_1$ in Equation 2.9. It is more convenient to look at the total $\vec{L}_s$=$\vec{L}_{rel} + \vec{L}_{cor}$.

The individual torques are calculated from their respective terms in Equations 2.1 and 2.2 (here represented as $f_x$ and $f_y$) by integrating over the volume of the ocean and dividing every torque into body-fixed components.

$$L_x = a \int_A H \left( f_y \sin\lambda - f_x \sin\phi \cos\lambda \right) dA \tag{2.21}$$

$$L_y = -a \int_A H \left( f_y \cos\lambda - f_x \sin\phi \sin\lambda \right) dA \tag{2.22}$$

$$L_z = a \int_A H f_x \cos\phi \sin\lambda \; dA \tag{2.23}$$

In this study, the frictional torque contains the terms of eddy-viscosity and bottom friction; the pressure torque includes the reduction due to LSA and the rotated pressure torque mentioned above.

In the real-time simulations with the complete forcing, the balance equations can only be balanced in the time-domain. In the frequency-domain, the tidal torque cannot be determined. For example, the tidal torque derived from the tidal potential of the $M_2$ partial tide will not be balanced with the heights and currents of the $M_2$ extracted from the real-time simulations due to interactions with other partial tides (see Chapter 4). Theoretically, the balance equation for the frequency-domain should be formulated as Equation 2.24.

$$\overset{\rightarrow eph}{L}_{tid} = -\sum_{pt} \left( \overset{\rightarrow pt}{L}_{rel} + \overset{\rightarrow pt}{L}_{cor} + \overset{\rightarrow pt}{L}_{pr} + \overset{\rightarrow pt}{L}_{pc} + \overset{\rightarrow pt}{L}_{fr} \right) \tag{2.24}$$

## 2.4 Harmonic Analysis

The results of experiments with the complete lunisolar tidal potential are real-time values and do not form fixed periods such as is the case for the partial tide simulations. However, the frequencies included in the time-series of the sea surface elevations and ocean currents can be derived from the astronomical tidal potential. Therefore, in the special case of ocean tides, the classical Fourier analysis can be replaced by a harmonic analysis with a discrete number of well-defined partial tide frequencies. To this end, the time-series to be analysed can be regarded as having the form (Emery and Thompson, 1998)

$$x(t_n) = \overline{x} + \sum_{pt=1}^{M} \left[ A_{pt} \cos\left(2\pi\sigma_{pt} t_n\right) + B_{pt} \sin\left(2\pi\sigma_{pt} t_n\right) \right] + x_r(t_n) \tag{2.25}$$

where $\sigma_{pt}$ is the respective tidal frequency, $\overline{x}$ the mean value of the record and $x_r(t_n)$ the residual time series. The desired values of amplitude $C_{pt}$ and phase $\phi_{pt}$ of the respective partial tide are then derived via

$$C_{pt} = \sqrt{A_{pt}^2 + B_{pt}^2}$$

$$\phi_{pt} = \tan^{-1}\left(B_{pt}/A_{pt}\right).$$

The calculation requires a $(M+1) \times (M+1)$ matrix $D$ containing the selected frequencies and a $(M+1)$ data vector $y$. The vector $z = D^{-1} \cdot y$ returns the values of $A_{pt}$ and $B_{pt}$ (for a detailed description see Emery and Thompson (1998)).

The selection of determinable partial tides depends on two criteria: the relative significance of the given tide and the resolvability of two ”neighbouring” frequencies. Considering a time-step of one hour, the resolvability is determined by the length of the time-series $T$ with the criterion (Emery and Thompson, 1998)

$$T > \frac{1}{|\sigma_{pt_1} - \sigma_{pt_2}|}. \tag{2.26}$$

The two predominant partial tides $M_2$ and $S_2$ can be unambiguously distinguished with a time-series of 14.7 days. The longer the time-series the more constituents can be resolved, including long-period tides. The fortnightly tide $Msf$ for example can be extracted from any time-series longer than 14.8 days, $Mm$ (monthly) after 31.8 days and $Mf$ (fortnightly) after 182.6 days (Emery and Thompson, 1998).

Experiments conducted for this study demonstrated that all partial tides listed in Bartels (1957) (including the solar annual tide $Sa$) should be unambiguously distinguishable with a time-series of at least 366 days. The generation of an artificial time-series following Equation 2.27 and subsequent harmonic analysis of the same constituents confirmed this.

$$x(t_n) = \sum_{pt=1}^{M} C_{pt} \cos\left(2\pi\sigma_{pt}t_n - \phi_{pt}\right) \tag{2.27}$$

Experiments reveal that only if the constituents were absolutely identical in both generation and analysis is an identical solution achieved. Small variations such as extracting only $M_e = 60$ constituents from a time-series generated with $M_g = 61$ constituents produces small differences between start-values and end-values. The accuracy of the results increases as more resolvable constituents are included in the analysis.

For this study, time-series of 400 days length with a time-step of 30 minutes were recorded from each simulation (5, 10, 15 and 20 minute resolution). Two different harmonic analyses were performed. For the evaluation (103 ”wet points”) all astronomic tides described in Bartels (1957) were included in order to get the best possible extraction of the diurnal and semi-diurnal tides (see Section 3.6).

Further analyses contained the entire global fields of sea surface elevation and currents. For simulations performed with the 5 minute resolution, this means more than 6 Mio wet points for all three variables $\zeta$, $u$ and $v$. As the computational time of the harmonic analysis increases as the square of the number of constituents (Emery and Thompson, 1998), the number of primary astronomical partial tides considered was reduced and only a selection of the most significant compound and overtides were included (see Appendix A.2).

## 2.5 Statistical Methods

Correlation coefficients and RMS-residua (root mean square) were calculated for simulation results compared with measurement data. The complex-valued sea surface elevation of a partial tide can be described as

$$\zeta_{pt} = A_{pt} \cdot e^{i \cdot \sigma_{pt} \cdot t} \cdot e^{-i \cdot \phi_{pt}} \tag{2.28}$$

where $A_{pt}$ and $\phi_{pt}$ are the amplitude and phase values and $i = \sqrt{-1}$. The correlation coefficient is defined as

$$r_{xy} = \frac{\sum_{i=1}^{n} \left[ \left( \zeta_i^a - \overline{\zeta^a} \right) \cdot \left( \zeta_i^b - \overline{\zeta^b} \right) \right]}{\sqrt{\sum_{i=1}^{n} \left( \zeta_i^a - \overline{\zeta^a} \right)^2 \cdot \sum_{i=1}^{n} \left( \zeta_i^b - \overline{\zeta^b} \right)^2}} \tag{2.29}$$

with $a$ and $b$ referring to the compared data sets. $\overline{\zeta}$ denotes to the respective mean value of the $n$ samples. The RMS-residuum is calculated as

$$RMS = \sqrt{\frac{1}{n} \cdot \sum_{i=1}^{n} \left( \zeta_i^a - \zeta_i^b \right)^2}. \tag{2.30}$$

For correlation coefficients sufficiently close to 1, a complex linear regression method (Hufschmidt, 1995) can be applied to ascertain whether a systematic error is observed when comparing the two data sets.

Based on a least squares method, the complex linear regression searches for the function $f$ that fullfills

$$\sum_{i=1}^{n} \left( f\left( \zeta_i^a \right) - \zeta_i^b \right)^2 = min \tag{2.31}$$

and can be described as

$$f\left( \zeta^a \right) = m \cdot \zeta^b + c \tag{2.32}$$

with

$$m = |m| \cdot e^{-i \cdot \Psi} \tag{2.33}$$

$$c = |c| \cdot e^{-i \cdot \Theta} \tag{2.34}$$

describing the amplitude factor $|m|$, the phase correction $\Psi$ and the correction to the zero-point $c$ (with amount $|c|$ and direction $\Theta$). A detailed description can be found in Hufschmidt (1995).

A perfect fit of two independent data sets would be characterised by a correlation coefficient and an amplitude factor of value 1 and a RMS-residuum and a phase correction of value 0.

## 2.6 Earth Rotation Parameters

Variations in the oceanic tidal angular momentum produce changes in the earth's rotation through interactions of the oceans with the solid earth. The results of the ocean tide simulations and the oceanic angular momentum were calculated for both the time-domain and frequency-domain, so the earth rotation parameters can be investigated in both domains.

The rotation of the earth can be regarded as changes in the orientation of an earth-fixed system $\Gamma$ within a space-fixed system $\Pi$. With $e_i$ ($i = x, y, z$) defining the orthogonal axes of the respective systems the earth's rotation can be formulated as (Seitz, 2004, after Richter (1995)):

$$e_i^\Gamma = R \cdot e_i^\Pi \tag{2.35}$$

where $R$ is the rotational matrix which can be divided into a precession matrix $P$, a nutation matrix $N$, a matrix $S$ describing the rotation along the angle of the appearant Greenwich sidereal time, and a matrix $W$ for the wobble or polar motion (Seitz, 2004).

$$\begin{aligned} e_i^\Gamma &= W \cdot e_i^\Delta \\ e_i^\Gamma &= W \cdot S \cdot e_i^\Theta \\ e_i^\Gamma &= W \cdot S \cdot N \cdot e_i^\Xi \\ e_i^\Gamma &= W \cdot S \cdot N \cdot P \cdot e_i^\Pi \end{aligned} \tag{2.36}$$

Every part of the matrix $R$ refers to a different system: $\Delta$ denotes the terrestrial equatorial system, $\Theta$ the true celestial equatorial system and $\Xi$ the mean celestial system. The true celestial system refers to the celestial ephemeris pole (CEP).

The precession describes the variations in the orientation of the earth's axis with respect to the ecliptic pole (normal to the ecliptic plane shown in Figure 2.2). Due to the precession the Aries point $\Upsilon$ moves along the ecliptic with a full period around the celestial sphere taking about 25,800 years (platonic year). The nutation is caused by periodic variations in the orbits of the moon and earth. It consists of a combination of several constituents with different amplitudes and frequencies between 5 days and 18.6 years. The last two matrices, $W$ and $S$, describe the influence of the earth rotation parameters.

The variations of the earth's rotation computed in this study refer to the CEP and in the frequency-domain follow Gross (1993) who investigated the earth rotation parameters (ERP) on the basis of the results of Seiler (1991) - which is the main precursor model of TiME. A number of measurement studies refer to this method of calculation and are therefore suitable for comparison (including Sovers et al., 1993; Herring and Dong, 1994; Gipson, 1996; Rothacher et al., 1998).

This approach determines the variations in the length of day and polar motion separate from each other - the axial component of the OTAM, $M_z$ (Equation 2.18), being responsible for the former and the two equatorial components, $M_x$ and $M_y$ (Equations 2.16 and 2.17), for the latter. For the polar motion - or wobble - the free core nutation and the Chandler wobble are taken into account as the most significant variations of the earth rotation (Gross, 1993).

A uniform rotation in the absence of any external torques can be formulated as

$$\vec{\omega_0} = \begin{pmatrix} 0 \\ 0 \\ \Omega \end{pmatrix} \quad , \quad \vec{I_0} = \begin{pmatrix} A & 0 & 0 \\ 0 & A & 0 \\ 0 & 0 & C \end{pmatrix} \tag{2.37}$$

where $A$ and $C$ determine the least and greatest principal moments of the earth's inertia. As the changes in the earth's rotation $\Delta \vec{\omega_0}$ due to external torques are small in comparison to $A$ and $C$ they can be formulated by the linearised Liouville equations (Munk and MacDonald, 1960):

$$\Delta \vec{\omega_0} = \Omega \cdot \begin{pmatrix} m_1 \\ m_2 \\ m_3 \end{pmatrix} \tag{2.38}$$

$$m_1 - \frac{\dot{m}_2}{\sigma_{CW}} = \psi_1 \quad , \quad m_2 - \frac{\dot{m}_1}{\sigma_{CW}} = \psi_2 \quad , \quad \dot{m}_3 = \dot{\psi}_3$$

with $\dot{m}_i = dm_i/dt$ and the complex-valued frequency of the Chandler wobble:

$$\sigma_{CW} = \frac{2\pi}{T_{CW}} \cdot \left(1 + \frac{i}{2 \cdot Q}\right) \tag{2.39}$$

with $T_{CW} = 434.45\, sd$ (sidereal days) and the damping constant $Q = 170$ (Wilson and Vicente, 1980). The excitation functions $\psi_i$ can be written as (Wahr, 1982)

$$\psi_1 = \frac{1.12 \cdot \left(\Omega \cdot \Delta M_x^{\Theta} + \frac{d\Delta M_y^{\Theta}}{dt}\right) + 1.61 \cdot \left(\Omega \cdot \Delta M_x^{r} + \frac{d\Delta M_y^{r}}{dt}\right)}{\Omega^2 \cdot (C - A)} \tag{2.40}$$

$$\psi_2 = \frac{1.12 \cdot \left(\Omega \cdot \Delta M_y^{\Theta} + \frac{d\Delta M_x^{\Theta}}{dt}\right) + 1.61 \cdot \left(\Omega \cdot \Delta M_y^{r} + \frac{d\Delta M_x^{r}}{dt}\right)}{\Omega^2 \cdot (C - A)} \tag{2.41}$$

$$\psi_3 = -\frac{0.756 \cdot \Omega \cdot \Delta M_z^{\Theta} + \Omega \cdot \Delta M_z^{r}}{\Omega^2 \cdot C_m} \tag{2.42}$$

where $C_m$ is the greatest principal moment of inertia of the earth's crust and mantle, $M_{x,y,z}^{\Theta}$ the rotational and $M_{x,y,z}^{r}$ the relative angular momentum (Section 2.3.1).

Variations in the length of day $\Delta\Lambda(t)$ or in universal time (UT1) are defined as

$$\Delta\Lambda(t) = -\Lambda_0 \cdot \psi_3(t) \;, \qquad \frac{d\Delta UT1}{dt} = -\psi_3(t) \tag{2.43}$$

with the nominal length of day $\Lambda_0 = 86,400\, s$. In the frequency-domain, the variations can be formulated as

$$\Delta UT1 = A_{pt} \cos(\sigma_{pt} - \phi_{pt}).$$

The complex-valued variation in the orientation of the earth's axis is defined by $p(t) = pmx(t) - i \cdot pmy(t)$ where the y-component is positive towards 90°W. In the frequency-domain, Gross (1993) determines the variations with respect to CEP as

$$\begin{aligned} p(\sigma_{pt}) = & \left[ 2.554 \times 10^{-4} \frac{\Omega}{\sigma_{fcn} - \sigma_{pt}} + 2.686 \times 10^{-3} \frac{\Omega}{\sigma_{cw} - \sigma_{pt}} \right] \cdot \frac{M_x^{\Theta} + i \cdot M_y^{\Theta}}{A \Omega \tau} \\ & + \left[ 6.170 \times 10^{-4} \frac{\Omega}{\sigma_{fcn} - \sigma_{pt}} + 1.124 \frac{\Omega}{\sigma_{cw} - \sigma_{pt}} \right] \cdot \frac{M_x^{r} + i \cdot M_y^{r}}{A \Omega} \end{aligned} \quad (2.44)$$

where $\sigma_{fcn} = -1.0023203\, cpsd$ (cycles per sidereal day) is the frequency of the free core nutation (FCN), and $\tau = \Omega^2 a^5 / (3GA)$ with the mean radius of the earth $a$ and the universal gravitational constant $G$.

The variations of polar motion $p(t)$ due to the constant force of a well-defined frequency results in an elliptical motion which can be described by a prograde ($p$) and a retrograde ($r$) circular movement defined by amplitude $A$ and phase $\alpha$ values (Gross, 1993).

$$p(t) = A_p \cdot e^{i \cdot \alpha_p} \cdot e^{i \cdot \sigma \cdot t} + A_r \cdot e^{i \cdot \alpha_r} \cdot e^{-i \cdot \sigma \cdot t} \quad (2.45)$$

In the time-domain, it is preferential to illustrate the variations in polar motion with the effective angular momentum functions (EAM) (Barnes et al., 1983). They are related to $\psi$ as

$$\psi_c = \chi_c - i \cdot \frac{\dot{\chi}_c}{\Omega} \quad (2.46)$$

where $c$ indicates the complex-valued notation of the equatorial components. Zharkov et al. (1996) give a measure for polar motion with the so-called $\chi$-functions.

$$\chi_c = \frac{1.12 \cdot \left( M_x^{\Theta} + i \cdot M_y^{\Theta} \right) + 1.61 \cdot \left( M_x^{r} + i \cdot M_y^{r} \right)}{\Omega \cdot (C - A)} \quad (2.47)$$

Compared to the $\psi$-notation (Equations 2.40 and 2.41) the $\chi$-functions do not include the acceleration terms ($\frac{d\Delta M}{dt}$) which is very convenient for the calculations.

# Chapter 3

# Model Performance and Evaluation

The precursor models of TiME used a coarser spatial resolution of 1°. The newly implemented high resolution of 1/12 of a degree globally required modifications in the modules that were adapted for TiME (Chapter 2) to ensure the feasibility of the simulations. The three major changes introduced to the model set-up will be discussed in this chapter:

1. a more stable treatment of the Coriolis term (Section 3.1);
2. modifications of the iteration scheme (Section 3.2); and
3. a two-step poleward zonal resolution decrease in the northernmost latitudes (Section 3.3).

As simulations with the old algorithm could not be performed on a significantly higher resolution these changes were tested on a 1°-set-up before increasing the resolution. The model code was partly reworked in order to secure optimal vectorisation on the high-performance computer system (Section 3.4).

An independent set of pelagic measurements of tidal elevations has been compiled by Le Provost (1995). It serves as a standard data set for evaluating ocean tide models and has been used for the evaluation of TiME. It includes 103 stations in the open ocean (Fig. 3.1) which are characterised by the amplitude and phase values of up to 13 selected partial tides. As the stations have been compiled considering the shortcomings of coarser ocean models, the improvements of the fine resolution of the new model will not necessarily produce a better correlation. The model has been tuned with $M_2$-only simulations for the four selected resolutions (Section 3.5) before evaluating the simulations performed for this study (Section 3.6).

## 3.1 Coriolis Term

TiME's direct precursor, the partial tide model of Seiler (1989), used an adaption of the semi-implicit numerical scheme of a barotropic shelf ocean model (Backhaus, 1983). Backhaus (1983) already discussed the possibility of a more stable treatment of the Coriolis term (after Wais, unpublished) but did not include it in the scheme yet. The refined description of the semi-implicit numerical scheme can be found in a successive work describing a three-dimensional baroclinic shelf ocean model (Backhaus, 1985). This scheme was adapted for the barotropic

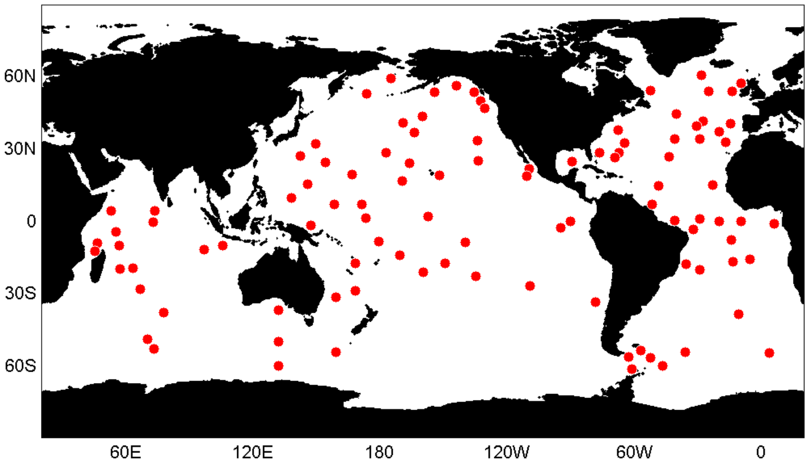

Figure 3.1: Locations of the 103 pelagic measurements of the MEOM data set (Le Provost, 1995).

model TiME. In general, the new scheme not only rotates the velocities (as in the previous approach) but also rotates the pressure gradient term (Section 2.1 and Appendix A.1.1).

In order to investigate the stability of the new and old scheme and their dependency on the model set-up, $M_2$-only simulations were performed on a series of different time-steps for both the new (red) and old (blue) algorithms (Fig. 3.2). The kinetic energy was calculated as global integration of the simulated ocean currents ($u$ and $v$) and the potential energies represents the sea surface elevations ($\zeta$).

For the smallest time-step of Figure 3.2 both algorithms calculate similar energy values. By gradually increasing the time-step from a few seconds to almost 7 minutes, both the kinetic and the potential energy have higher values in case of the simulations with the old algorithm. The kinetic energy has been increased by roughly 20% from $3$ to $3.6 \cdot 10^{24} \frac{g \cdot cm^2}{s^2}$. The time-step dependency is eliminated with the new scheme as the amounts of kinetic and potential energy remain at nearly constant values no matter which modelling time-step has been chosen. This clearly demonstrates the stability gained from the new algorithm.

## 3.2 Iteration Scheme

The semi-implicit algorithm used in this study requires an iterative calculation of the sea surface elevations which is done by successive over-relaxation (SOR, e.g. Press et al., 1987). As the algorithm has been reworked (see Section 2.1), the SOR-scheme had to be modified as well and was taken in parts from the one formulated in the Hamburg Shelf Ocean Model (HamSOM) which utilises a similar numerical scheme (Pohlmann, 1996). The SOR-problem can be formulated after Backhaus (1985):

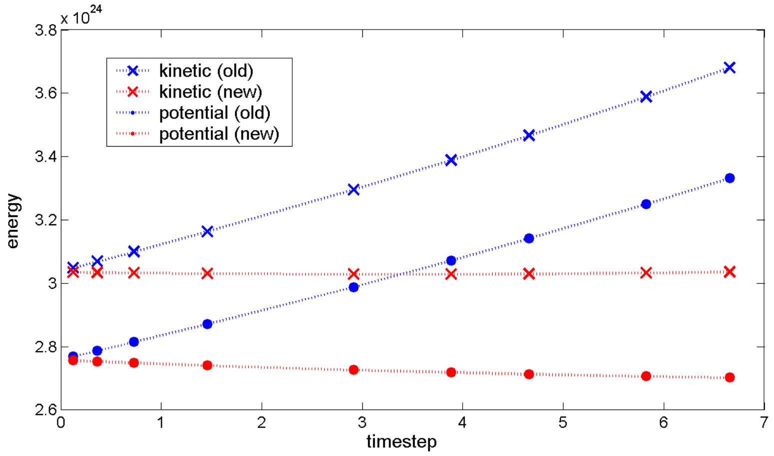

Figure 3.2: Reduced time-step dependency of the numerical scheme (timestep in minutes; energies in $\frac{g \cdot cm^2}{s^2}$).

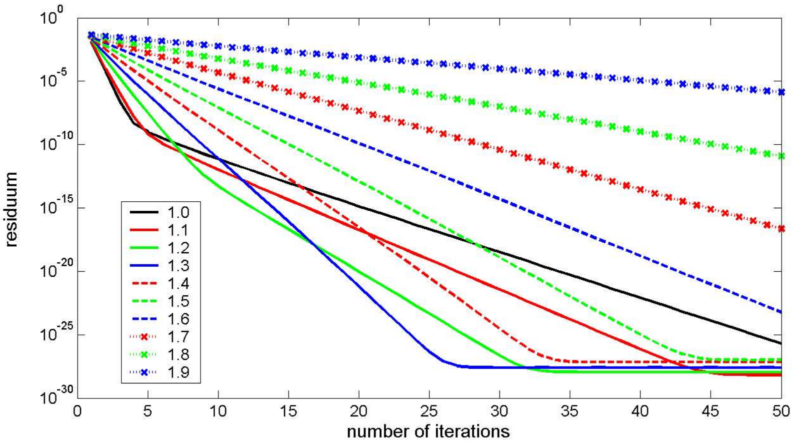

Figure 3.3: Experiments with different relaxation parameters $\omega$ of Equation 3.1.

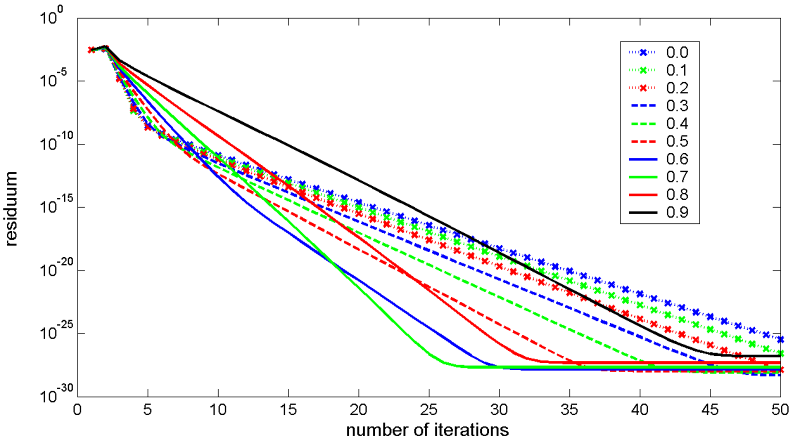

Figure 3.4: Experiments with different values for $\rho$ of Equation 3.3.

$$\zeta^{k+1} = (1-\omega)\cdot\zeta^k + \frac{\omega}{1+c_5}\cdot\left(B + C + c_2\zeta_N^{k+1} + c_4\zeta_W^{k+1} + c_6\zeta_E^{k+1} + c_8\zeta_S^{k+1}\right.$$
$$\left. + c_1\zeta_{NW}^k + c_3\zeta_{NE}^k + c_7\zeta_{SW}^k + c_9\zeta_{SE}^k\right) \qquad (3.1)$$

where $k$ denotes the iteration step and $\omega$ the relaxation parameter. For an illustration of how to calculate $B$, $C$ and the coefficients $c_i$ the reader is referred to Backhaus (1985) and Appendix A.1.1 of this study. The SOR-problem is formulated on a so-called chess-board-scheme leading to $k+1$-indices of the directly neighbouring $\zeta$-points. Figure 3.3 shows results from the experiments with different values for $\omega$. The residuum was calculated as $R = \sum_A |\Delta\zeta^{k-1} - \Delta\zeta^k|$.

Depending on the desired accuracy of the results, the best $\omega$ to ensure the fastest iteration is $1.2$ to $1.3$ (for the first iteration steps simulations with $\omega$-values of $1.0$ or $1.1$ are faster converging but these results would be of too low accuracy).

In order to improve convergence, two further alterations were introduced. First, as tidal elevations are fairly regular and predictable in the sign and value of changes from one time-step to the next, one might begin the iteration with a ”first guess” $\Delta\zeta_{fg}^n$ as a starting value of the iteration (Maier-Reimer, pers. comm.).

$$\Delta\zeta_{fg}^n = 2\cdot\Delta\zeta^{n-1} - \Delta\zeta^{n-2} \qquad (3.2)$$

Second, a Chebyshev acceleration has been implemented using a ”flexible” relaxation parameter $\omega^k$ (after Press et al., 1987, and Maier-Reimer, pers. comm.).

$$\begin{aligned} \omega^{\frac{1}{2}} &= 0.5 \\ \omega^1 &= 1 \\ \omega^{k+\frac{1}{2}} &= \frac{1}{\sqrt{1-\frac{\rho^2\cdot\omega^k}{4}}} \\ \omega^\infty &\longrightarrow \omega_{optimal} \end{aligned} \qquad (3.3)$$

The parameter $\rho$ basically defines to which $\omega_{optimal}$ the flexible $\omega$ will converge. Consequently, the results from the experiments with different values for $\rho$ (Figure 3.4) reveal a similar pattern as Figure 3.3. The simulations with $\rho = 0.6$ will lead to a $\omega_{optimal}$ of about $1.2$ and $\rho = 0.7$ to a $\omega_{optimal}$ of about $1.3$. In the following, either a constant value of $\omega = 1.3$ or a flexible $\omega$ with $\rho = 0.7$ have been used.

Comparing the different alterations (Figure 3.5) reveals that the new algorithm converges significantly faster than the old one. Experiments with a time-step of about 4 minutes were performed with the old (dashed black) and the new (solid black) numerical scheme. The first guess (red) and the flexible relaxation parameter (green) were introduced separately and in combination (purple). The introduction of a first guess seems to replace the first 15 to 20 iteration steps and has a strong effect on reducing iteration time. The flexible $\omega$ gives slightly better results for only the first 30 iterations.

Experiments with different convergence criteria of $\Delta\zeta$, i.e. the desired accuracy of the iteration, were performed with the old numerical scheme for two different time-steps: about 4 minutes

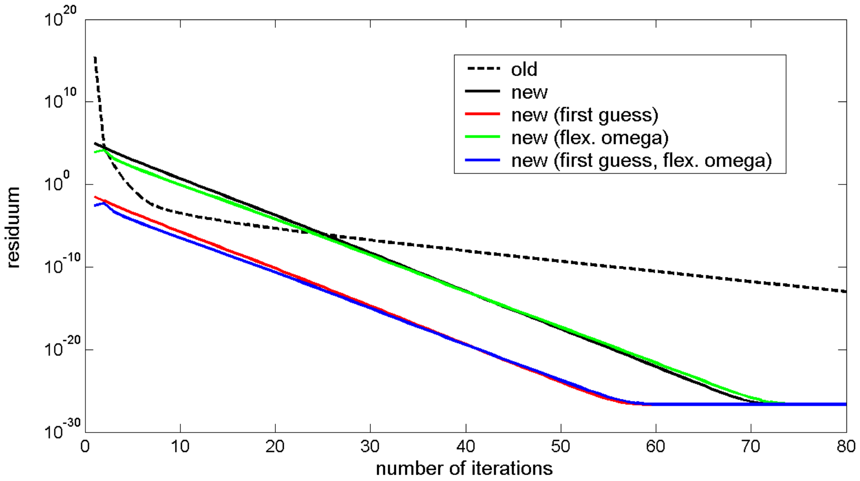

Figure 3.5: Convergence of the iteration scheme.

(green) and about 6.5 minutes (black) (Fig. 3.6). Experiments with the new scheme incorporated both the first guess and the flexible $\omega$ and utilised the same time-steps (blue and red). Note that the old algorithm iterated in blocks of 20 iterations before investigating whether the criterion is matched.

Simulations with the old algorithm on a time-step of about 4 minutes (green) show that iteration time roughly increases by another block of 20 iterations with every order of magnitude in decrease of the criterion. For simulations with a time-step of about 6.5 minutes the number of iterations increases dramatically. For the new scheme (blue and red) the number of iterations needed to match a certain accuracy only increases by 3 to 5 per order of magnitude of the criterion. This clearly reveals the improved convergence of the new scheme and its reduced time-step dependency. Eventually, a criterion of $10^{-7}\,cm$ has been chosen for the experiments performed for this study.

## 3.3 Poleward Resolution Changes

The numerical equations of the ocean module are formulated on a spherical grid, so the actual meridional distance (north-south-direction) between two neighbouring grid points has a constant value of about 10 kilometres at 5 minute resolution. In the zonal (east-west) direction the grid narrows towards the poles. As the minimum distance between two grid points constrains the largest possible time-step with which the model can be run, the grid of the North Pole region had to be altered so that the smallest distance does not fall below 2 kilometres. The problem was solved by decreasing the zonal resolution by a factor of two towards the North Pole at two latitudes of the user's choice. The principle of the resolution change follows Zahel (1970) and was formulated for the numerical scheme of TiME. At the North Pole itself the system of equations is tied together by a polar cap represented by a single sea surface elevation grid point and is variable in size.

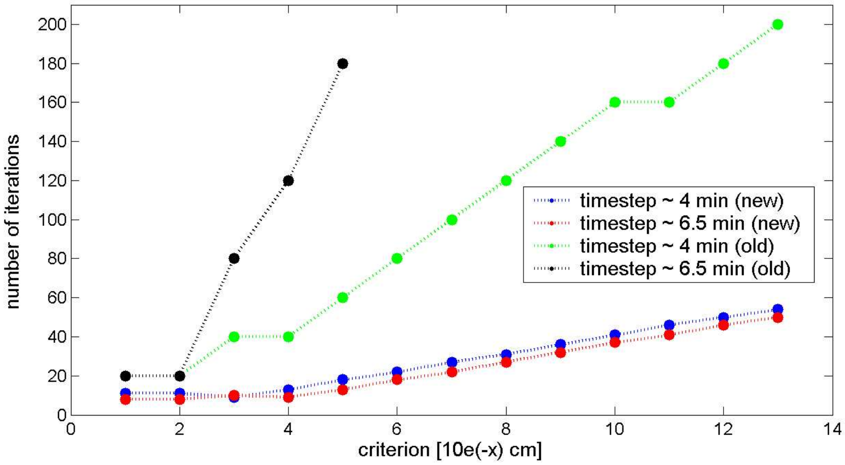

Figure 3.6: Experiments with different convergence criteria.

The equations of motion and continuity of the ocean part are formulated as finite-difference equations in the semi-implicit scheme. Their application at the latitudes of the resolution change and at the polar cap are described in detail in Appendix A.1.2 and A.1.3.

The resolution change towards the North Pole has been tested on an "aqua planet" which is an artificial globe with the southern hemisphere completely covered by land and the northern hemisphere covered by water with a uniform depth of 500 metres. Three different experiments were conducted:

A) constant zonal resolution of 4°;

B) zonal resolution of 1° changing to 2° at 66.5°N and further to 4° at 76.5°N; and

C) as in B except that resolution changes occur at 76.5°N and 82.5°N.

The meridional resolution has a constant value of 1° and the polar cap a radius of 2.5° in all three simulations. All three experiments were forced with the $M_2$ partial tide. Figure 3.7 shows the amplitude and phase values of the three set-ups A, B and C. The results reveal that the resolution changes do not disrupt the pattern. No phase distortion occurs at the boundaries.

Figure 3.8 illustrates the differences between the three simulations. The maximum difference in amplitudes are found in A-B and A-C with differences of up to 0.1 cm in areas south of the location of the resolution changes of B and C. Almost no changes remain in B-C. This supports the interpretation that the changes in A-B and A-C are due to the different resolutions (with their respective parameterisations) and not due to the numerical solution of the boundary problem at the latitudes of the resolution change. No changes in amplitude due to reflections at the resolution changes are visible.

Set-up C was chosen for the simulations of this study so that the resolution changes are as far north as possible. As the South Pole is covered by land, it does not require a resolution change nor a polar cap.

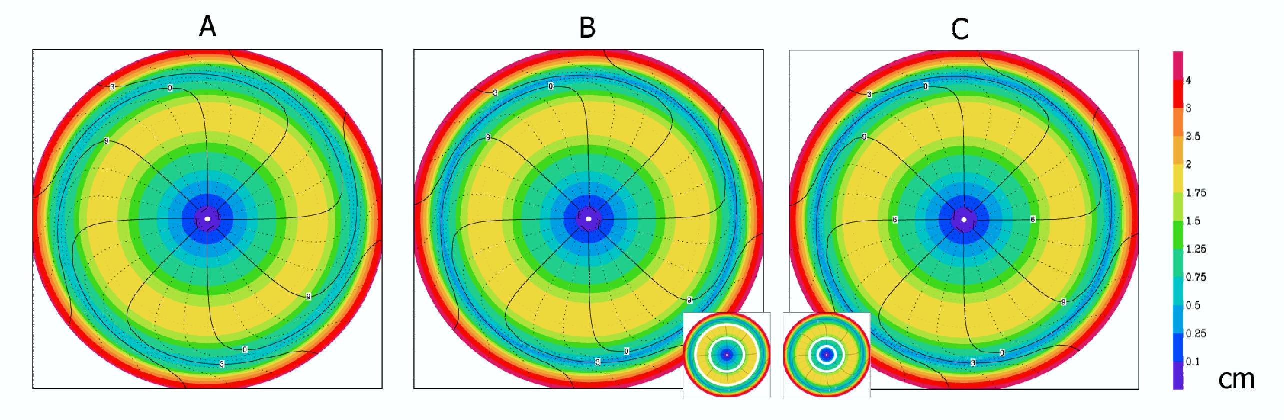

Figure 3.7: $M_2$ amplitudes and cotidal lines (in hours) for three different set-ups (A, B and C) of an "aqua planet". The plots show the North Pole area from 59°N to 90°N. The inset images indicate the position of the resolution change with a white circle.

## 3.4 Overall Model Performance

When TiME is run on 5' resolution with the complete lunisolar forcing and with a time-step of 2 minutes, it needs about 6 GB of storage space and 30 minutes of CPU-time (central processing unit) to simulate one calendar day. Within the DKRZ-system, only simulations of up to four hours of CPU time are permitted (for non-parallelised models). Hence, a "chain-job" structure has been implemented where only five days of simulation are performed within one batch job in order to provide some head room for any irregularities. A full simulation of 366 days (so that all partial tides can be extracted) takes about 183 hours of CPU-time.

The model spends more than 65% of the total CPU-time in the SOR-scheme, which stresses the importance and necessity of the modifications in the iteration scheme implemented in TiME (Section 3.2). As the simulations are carried out on a vector computer, vectorisation of the calculations is essential for the model performance. The average vector length of TiME is about 243 (with 256 being an optimal value) and the vector operation rate is 99.6% (100% would mean a perfect vectorisation).

## 3.5 Adjustments of Model Parameters

The equations of motion in TiME (Equations 2.2 and 2.1) include a number of parameterisations: namely the bottom friction (coefficient $r$), the influence of earth tides (Love Numbers), the effect of load and self-attraction ($\epsilon$), and the eddy-viscosity ($A_H$). Following the investigations of Seiler (1989) and Thomas (1996), only the eddy-viscosity has been used as a tuning parameter (keeping $r = 0.003$ and $\epsilon = 0.1$).

The value of $A_H$ determines the influence and importance of the eddy-viscosity within the

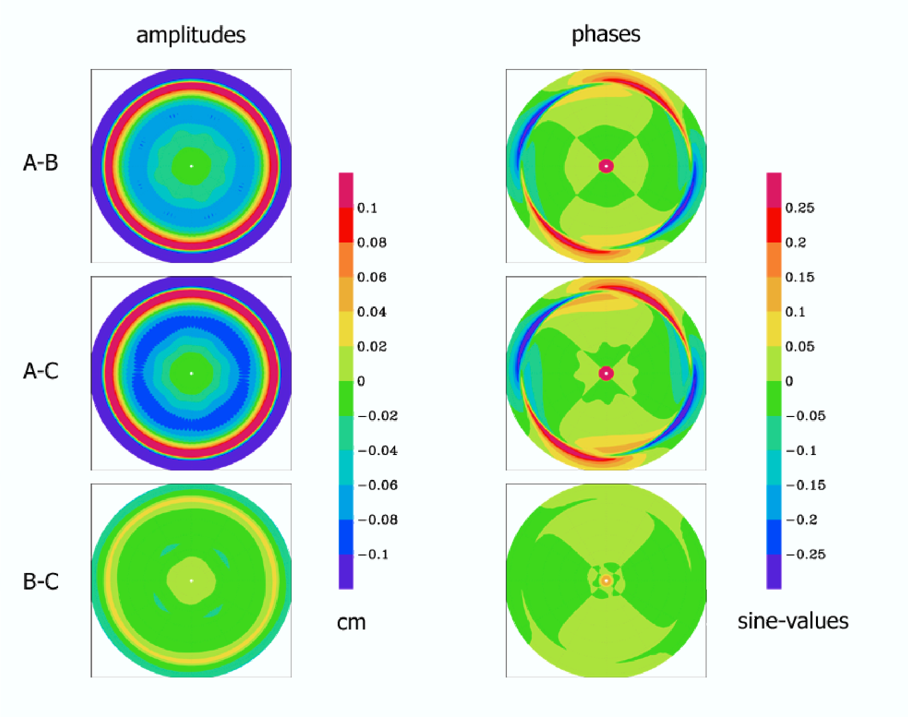

Figure 3.8: Differences in amplitudes and phases between the aqua planet simulations A, B and C.

equations of motion. This term, describing the horizontal exchange of water masses, is designed to parameterise small scale processes taking place within a model grid box and is consequently dependent on the spatial dimensions of the grid. Equations 2.7 and 2.8 already include a latitude dependency through

$$A_m = A_H \ , \quad A_z = A_H \cdot \cos\phi .$$

Tuning $A_H$ requires some experimentation. Figure 3.9 shows comparisons between a series of $M_2$-only simulations with different resolutions and different $A_H$-values compared to the ST103 data set (Le Provost, 1995, Fig. 3.1). $A_H$-values higher or lower than the ones plotted in the figure lead to numerical instability. For the 5'-resolution simulation (red) the range of numerical stable values of $A_H$ lies between $5$ and $45 \cdot 10^3 \, \frac{m^2}{s}$.

Most free numerical ocean tide models, i.e. those not assimilating data, have a tendency towards overestimating the heights of most partial tides. It is likely that some frictional processes are not included in the equations of the models leaving too much energy in the system (Egbert et al., 2004). As eddy-viscosity is an important frictional term and helps dampen the sea surface elevations, it is not surprising that the largest $A_H$-values produce the best RMS-values. The correlation coefficients indicate that the best results are achieved with slightly reduced values of $A_H$. In general, the results show very good to excellent correlation with measurements.

A linear regression analysis of these experiments reveals several systematic trends. Figure 3.9 (middle) shows a general improvement of both amplitude factors and phase corrections with

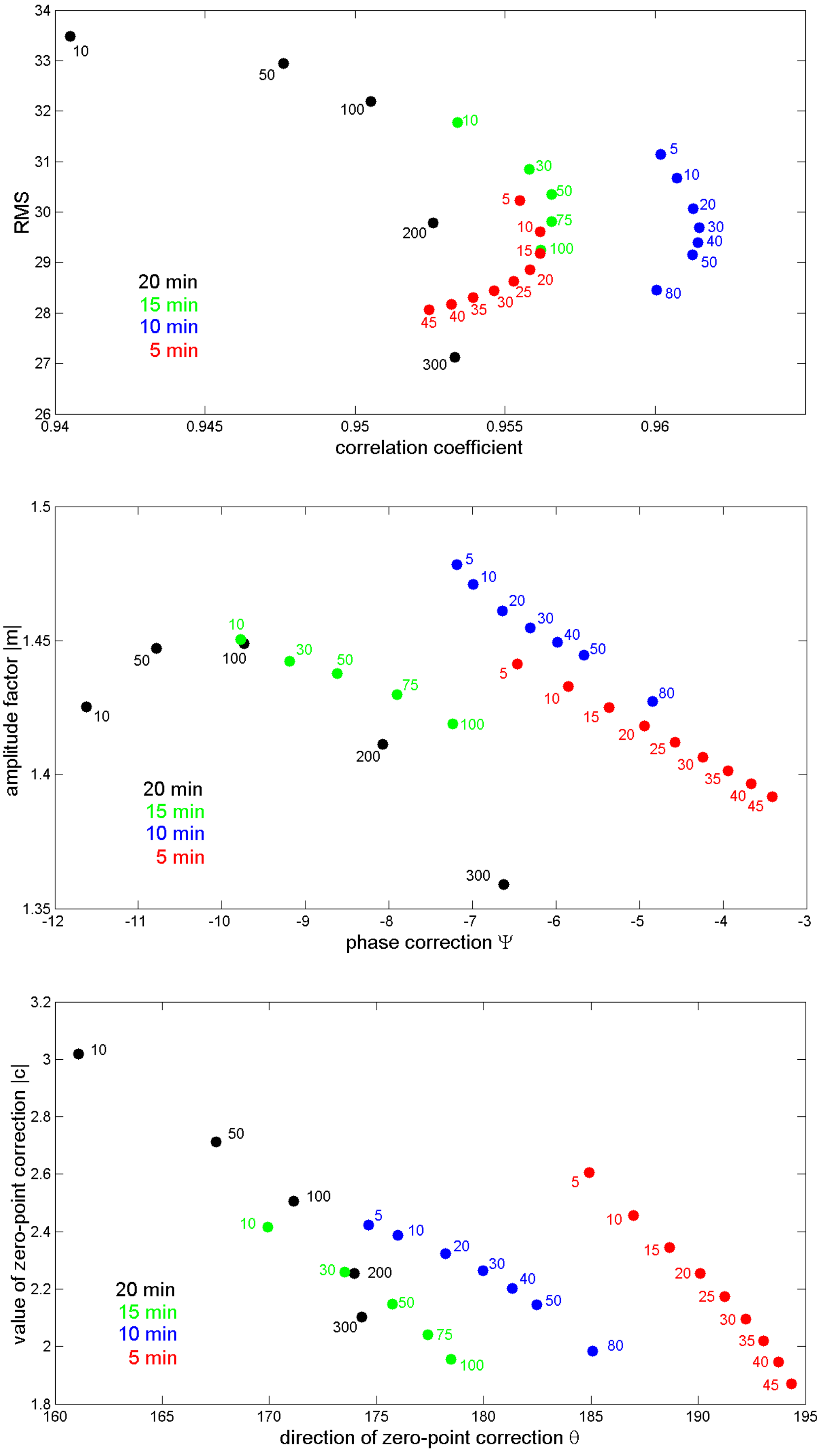

Figure 3.9: RMS-values and correlation coefficients for different model resolutions and eddy-viscosities compared with the ST103-data (top). Linear regression: Amplitude factors and phase corrections (middle) and zero-point correction (bottom). The numbers indicate the respective $A_H$-value ($x \cdot 10^3 \frac{m^2}{s}$).

increasing $A_H$-values, corresponding with the RMS-value-trends (top). The same holds for the amount of the zero-point correction $|c|$ (bottom). The value $\Theta$ determines the direction of the zero-point correction and is centred around 180°. Deviation from 180° leads to a loss in correlation (top) and may indicate a systematic shift in phases.

As a general impression, the higher-resolving versions of TiME (15' to 5') are less dependent on the choice of $A_H$. As a compromise between the best RMS-value and the best correlation coefficient, an $A_H$-value of $3 \times 10^4 \frac{m^2}{s}$ for the 5' resolution has been chosen. The values of the lower-resolving versions of TiME have then been chosen so that they produce results that agree best with the results of the next higher-resolving ones leading to $5 \times 10^4 \frac{m^2}{s}$ for 10', $7.5 \times 10^4 \frac{m^2}{s}$ for 15', and $10 \times 10^4 \frac{m^2}{s}$ for 20'.

## 3.6 Evaluation of Model Results

Simulations of four other partial tides have been performed ($S_2$, $N_2$, $O_1$ and $P_1$). From the results of simulations with the complete lunisolar tidal potential, all 13 partial tides considered in the MEOM data set were determined through harmonic analysis and compared analogously.

Figure 3.10 (top) shows RMS-values and correlation coefficients of the five partial tide runs as well as the extracted partial tides. Only results of the 10' and 5' resolutions are plotted as they are the most important ones for this study. With values of $r_{xy} > 0.88$ throughout, the correlation with the pelagic data set can be described as very good.

The RMS-values are relatively high, especially for the two main tides $M_2$ and $S_2$, which can be related to the tendency towards overestimation of most free models mentioned above. The $M_2$-tides extracted from the full forcing simulations are even higher than the partial tides. There is, however, no visible general trend when comparing partial tide simulations with full forcing simulations (see e.g. $S_2$-results). Instead, the resolution of the respective simulation seems to be more significant since often the partial 5' (green points) closely pair with the complete 5' (red) and the partial 10' (blue) with the complete 10' (black).

Most amplitude factors (Fig. 3.10, middle) are within 1.0 and 1.4 showing the expected tendency towards overestimation. Phase corrections predominantly have negative values suggesting that the simulated tidal waves have a slight lead compared to the measurements. The higher resolution improves the values in phase correction for a number of partial tides ($Q_1$, $O_1$, $N_2$, $M_2$, $K_1$ and $S_2$), but can not be regarded as a systematic trend as also the opposite can be observed ($K_2$, $L_2$ and $P_1$).

In general, comparisons with the pelagic measurements of the ST103 data-set show that the oscillation system can be regarded as well-captured by the model for all 13 diurnal and semi-diurnal partial tides considered. The model has a tendency towards overestimating sea surface heights.

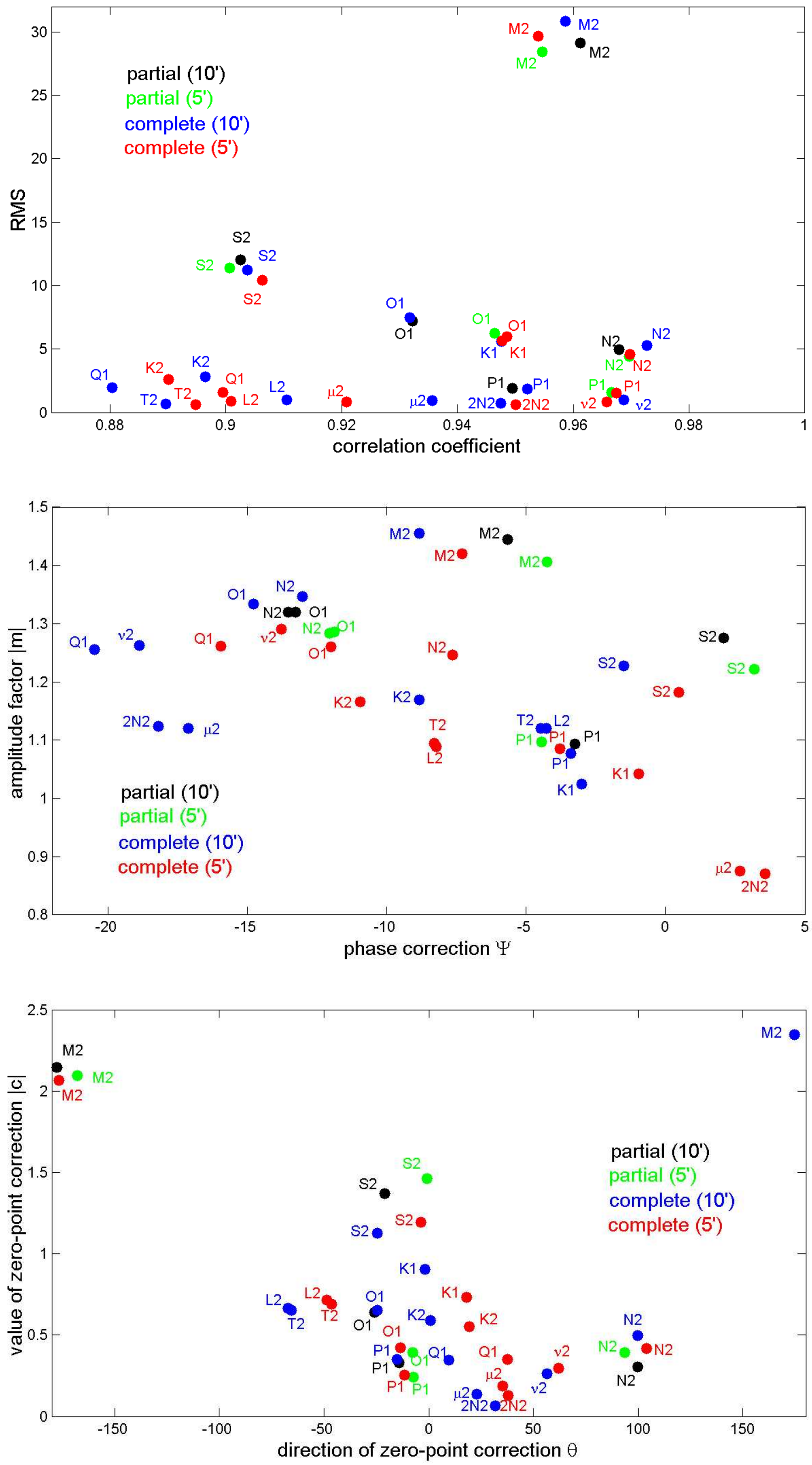

Figure 3.10: RMS-values and correlation coefficients for different partial tides and different resolutions (top). Linear regression: Amplitude factors and phase corrections (middle) and zero-point corrections (bottom).

# Chapter 4

# Ocean Tide Simulations

The oscillation system of the ocean tides as represented by the new model TiME will be discussed with examples of the influence of bathymetry and spatial resolution (Section 4.1) and the influence of the complete forcing as compared to the traditional partial tide forcing (Section 4.2).

A global description of non-linear shallow-water tides is given in Section 4.3, a result of implementing the complete tidal potential of second degree in a high-resolving ocean model.

## 4.1 Influence of Bathymetry and Resolution

TiME has been run with two different bathymetries (GEBCO or ETOPO, see Figure 4.1) and four different resolutions (5', 10', 15' and 20'). The $M_2$-only simulations discussed in Sections 3.5 and 3.6 indicate that no significant improvement in the description of the global oscillation system can be expected for the open ocean with an increase of resolution. Rather, the implementation of higher resolution is expected to show the most significant improvements in shelf areas and possibly in some regions of the open ocean.

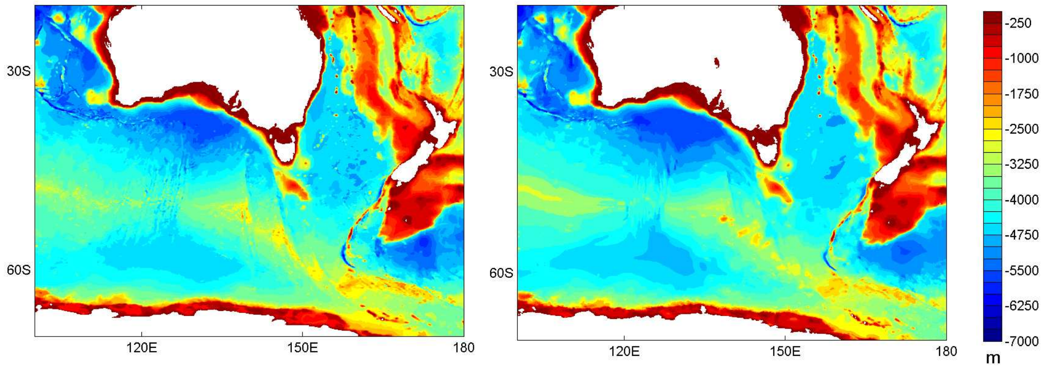

Figure 4.1: Bathymetries of 5' resolution: GEBCO (left) and ETOPO (right). Excerpted from global bathymetry showing the Southern Ocean between Australia, New Zealand and Antarctica.

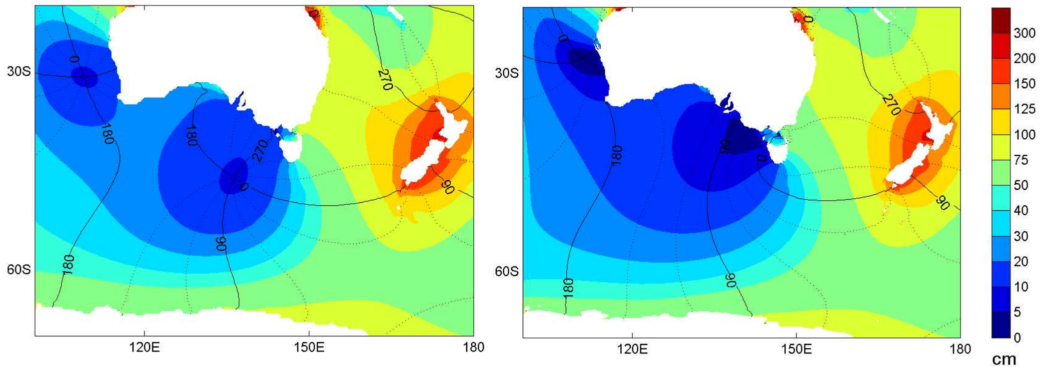

Figure 4.2: Amplitudes and phases (in degrees) of $M_2$-only simulations with the GEBCO bathymetry with 20' resolution (left) and 5' resolution (right). Excerpted region of global simulation same as in Figure 4.1.

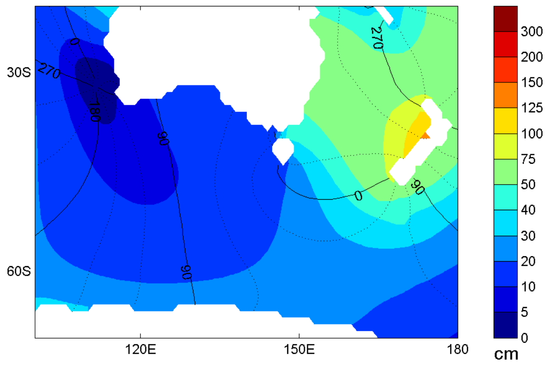

Figure 4.3: Amplitudes and phases of an $M_2$-only simulation with data assimilation on 60' resolution taken from Zahel et al. (2000). Excerpted region of global simulation same as in Figure 4.1.

The latter is shown to be the case with one interesting large scale feature improved via increased resolution. Almost all ”free” models, i.e. without any data assimilated, describe an amphidromic point of the $M_2$ in the Southern Ocean south of Australia [1]. Measurements, however, have shown that the $M_2$ travels westward throughout the entire region (Cartwright et al., 1979). Data assimilation models correct this inaccuracy displayed by free models (e.g. Zahel, 1995) and consequently mark this region with a pronounced dynamic residual (Zahel et al., 2000).

Model simulations with TiME display this feature correctly simply by increasing the resolution based on the GEBCO bathymetry (Fig. 4.2). The excerpts shown in the figure stem from global $M_2$-only simulations on 20' and 5' resolution. The oscillation system east and west of the part

---

[1] An amphidromic point, or amphidrome, is a point with almost no tidal elevation. It is the centre of a rotational wave pattern of the respective partial tide and is marked as a conjunction of phase lines (e.g. Pond and Pickard, 1983).

of the Southern Ocean between Australia and Antarctica is essentially the same for both resolutions. Only the direction of the tidal wave off the southern coast of Australia is reversed. The general oscillation pattern generated with 5‘ resolution matches the results of the data assimilation models excepting that the wave as described by TiME propagates faster. For comparison see Figure 4.3 where results from Zahel et al. (2000) are shown. The cotidal line of 90 degrees at the southern tip of New Zealand corresponds well with Figure 4.2. Some 360 degrees later, with the $M_2$-tide travelling westward, the next cotidal line of 90 degrees leads the data assimilation model by about 60 degrees. Note that the amplitudes in the results of the data assimilation model are significantly lower than in the results of TiME with the GEBCO topography. This can be explained with the dissipative nature of the dynamic residuals introduced due to the assimilation of data (Zahel et al., 2000).

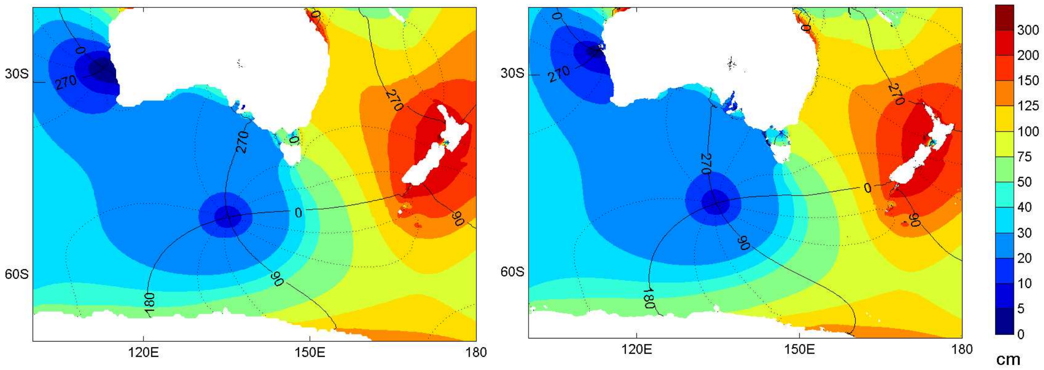

Figure 4.4: Amplitudes and phases of $M_2$-only simulations with the ETOPO bathymetry with 20’ resolution (left) and 5’ resolution (right). Excerpted region same as in Figure 4.1.

Repeating the experiments with the ETOPO bathymetry and an otherwise identical model set-up produces Figure 4.4. Two statements can be made: 1) Amplitudes are remarkably higher then in Figure 4.2; 2) The amphidromic point does not disappear with the resolution increase.

Experiments with ”mixed” topographies, i.e. replacing given regions of the ETOPO bathymetry with the respective part of the GEBCO bathymetry and vice-versa in various dimensions, were performed. They revealed that the presence of the amphidromic point does not seem to be governed by the immediate regional topography. The desired change is only achieved when almost the entire Southern Ocean is described by the GEBCO topography.

This demonstrates that the exact locations of amphidromes can be quite sensitive to changes in the model set-up and that they are determined by the general oscillation system.

In order to explain the differences in amplitudes between the GEBCO and ETOPO bathymetries, a thorough investigation of the raw data and algorithms applied for the generation of the maps would be required, which is beyond the scope of this study. Generally, the GEBCO bathymetry is ”rougher” and the ETOPO ”smoother”. Because the results obtained with GEBCO correlate better with measurements (not shown) and in light of the improvement indicated in Figure 4.2 this bathymetry has been chosen as more suitable for TiME.

## 4.2 Influence of the Complete Forcing

With the implementation of the complete lunisolar tidal potential, all partial tides from the second degree harmonics are included in the real-time simulations, allowing for interactions between partial tides. In the following, the tides extracted from the real-time simulations will be compared with the results from the partial tide forcings.

The principal solar diurnal tide $P_1$ will serve as the first example. It is shown as modelled using partial tide forcing (Figure 4.5, top) and as extracted from a simulation with complete forcing (Figure 4.5, middle). The simulations agree well with each other in their description of the global oscillation system.

The propagation of this tide in the Southern Ocean is characterised by a circumpolar Kelvin wave. The cotidal line of 0° is roughly at 0° longitude, the 180° line is at 180° longitude and the cotidal line of 270° is located at 90°E. This shows that the Kelvin wave travels with a quite uniform speed and a wavenumber of $m = 1$ around Antarctica without being much disturbed by the Drake Passage (between Antarctica and South America). Parts of the wave are deflected into the Atlantic and Pacific Ocean. The propagation in the Atlantic Ocean is determined by two cyclonic amphidromes. Amplitudes are relatively low compared to the other ocean basins because the Atlantic is not favourable to resonance for the $P_1$ (Zahel and Müller, 2005).

The Pacific Ocean is governed by a set of three amphidromic points, leading to a constant anti-clockwise propagation along the coasts from equatorial South America to East Asia. In the Northern Pacific the $P_1$ can reach amplitudes of up to 15 cm in the open ocean. In the adjacent seas of the Western Pacific the highest amplitudes are found with more than 60 cm. The Pacific is connected to the Southern Ocean by a Kelvin wave around New Zealand and an amphidrome near the Fiji-Islands. The Indian Ocean is characterised by an anti-clockwise amphidrome just south of India and roughly at the equator. The highest amplitudes are found in the Sea of Arabia with up to 15 cm. A second amphidrome at about 45°S and 60°E connects the Indian to the Southern Ocean.

As Figure 4.5 (top and middle) only shows every sixteenth data point of the 5' resolution some "distorted" looking cotidal lines (e.g. at 45°S, 70°E and 45°S, 175°W) indicate that at these locations the oscillation system is significantly influenced by regional bathymetry. Apart from these distortions, the global propagation pattern compares reasonably well with the results from other tidal models that also include a more detailed description of global oscillation systems (e.g. Schwiderski, 1981; Seiler, 1989).

Taking a closer look at the distortions southeast of New Zealand demonstrates the significance of the local topography (Figure 4.6). The amplitudes and phases (top) represent an excerpt of Figure 4.5 (middle). The patterns of the oscillation system resemble the ones calculated by Walters et al. (2001, Fig. 7 therein) with a regional barotropic ocean tide model forced by satellite altimetry data at the boundaries. In detail, however, the model results differ quite substantially.

The distribution of flow transport (Figure 4.6 (bottom)) shows the greatest values around 175°E, 57°S at the break of the New Zealand Plateau. Müller (in review) has recently shown that a topographic vorticity mode with a period of 32.56 hours exists in this area and that this mode

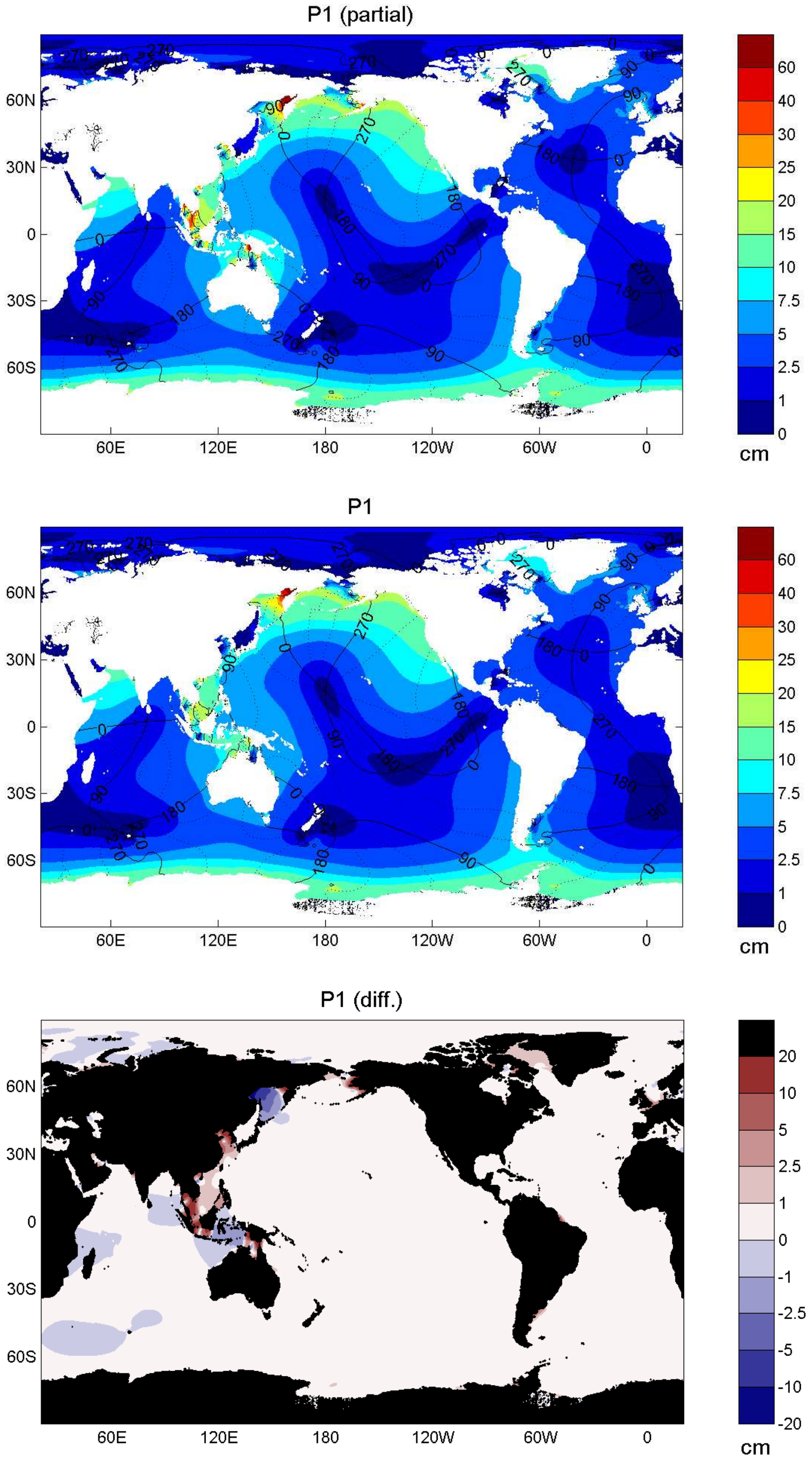

Figure 4.5: Amplitudes and phases (in degrees) of the $P_1$ with partial tide forcing (top) and extracted from simulation with complete forcing (middle) and their differences in amplitudes (bottom).

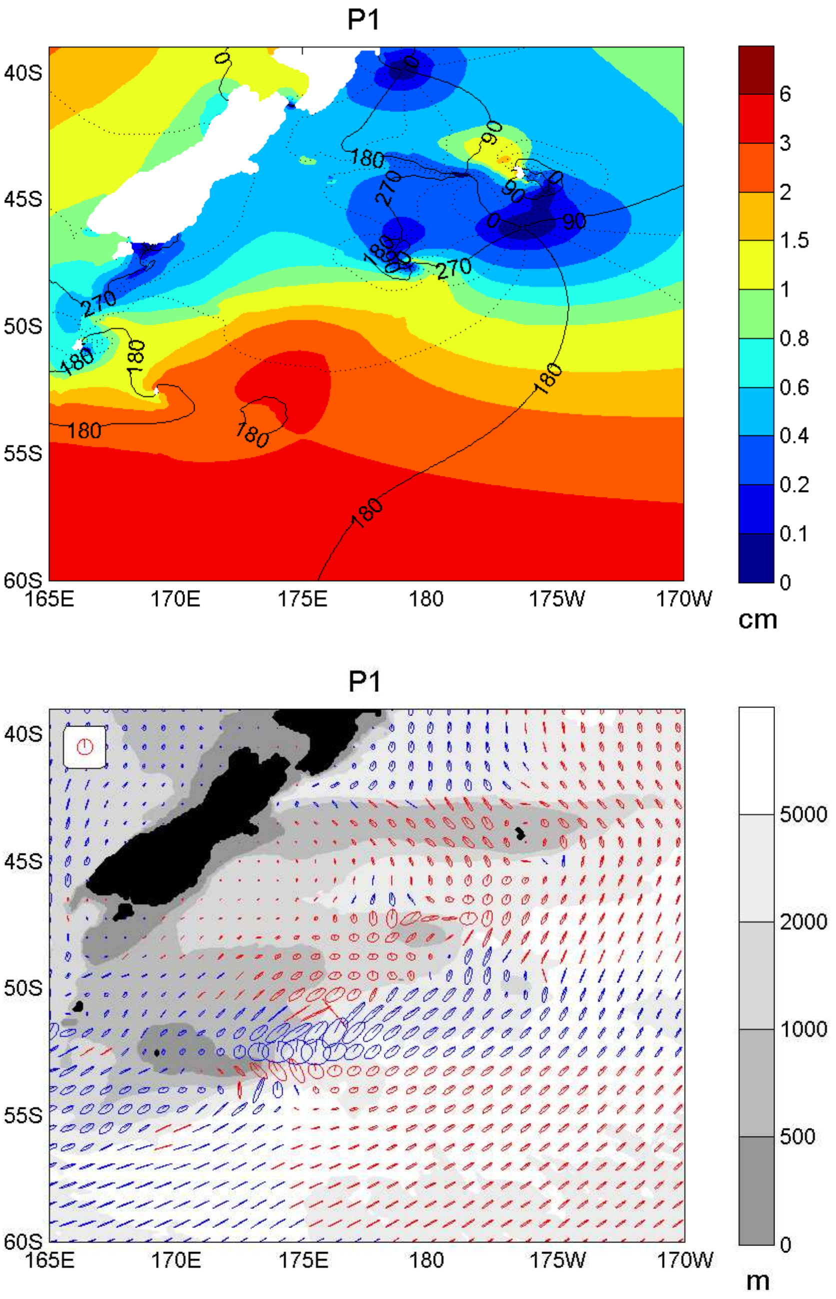

Figure 4.6: Amplitudes and phases (in degrees) of the $P_1$ southeast of New Zealand (top) and transport ellipses (bottom). Water depths are shown in grey shading. A ”legend” tidal ellipse has been added to the figure in the upper left corner. It represents a current characterised by $U = V = 10\frac{m^2}{s}$ and $\phi_U = 90^\circ$ and $\phi_V = 0^\circ$. Cyclonic tidal ellipses are drawn in red (i.e. clockwise in the southern and ant-clockwise in the northern hemisphere).

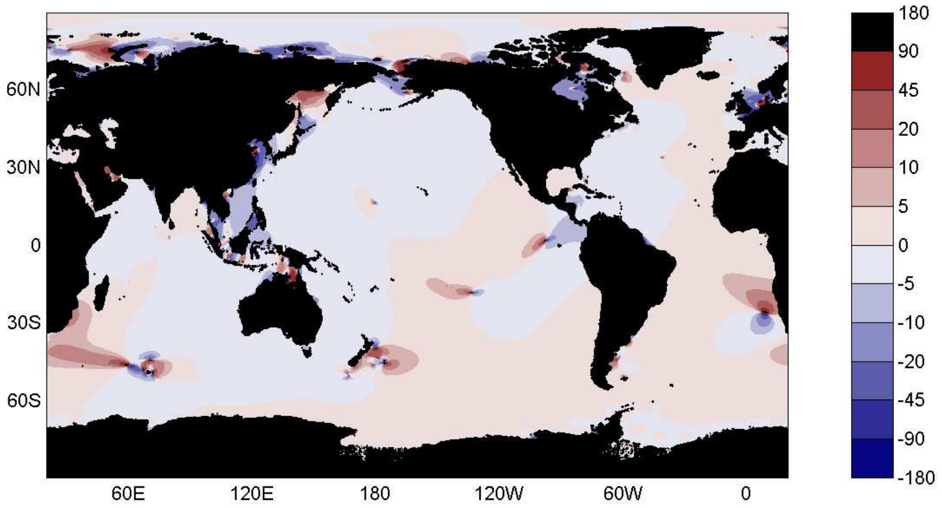

Figure 4.7: Differences in phases (in degrees) between $P_1$-only forcing (Fig. 4.5, top) and $P_1$ extracted from complete forcing simulation (Fig. 4.5, middle).

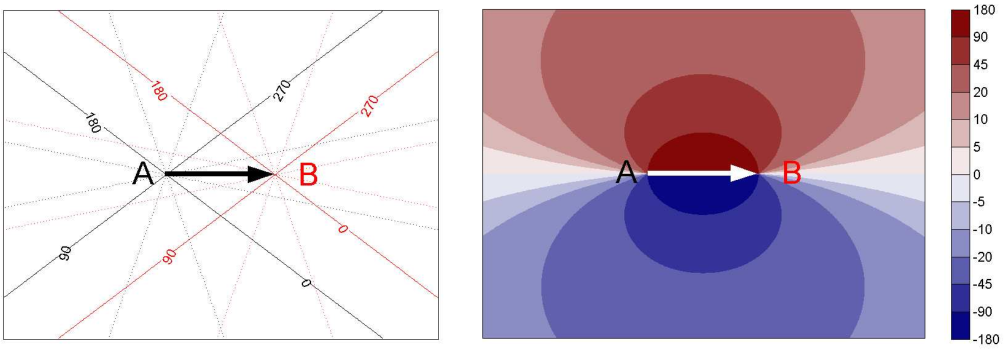

Figure 4.8: Conceptual explanation of a shift in the position of an amphidromic point as represented by phase differences (in degrees). The amphidrome A (black) is shifted to the right (or eastward) to B (red). The difference $d\phi = \phi_A - \phi_B$ produces a distinct colour pattern. The line with 0° differences (shown in white) indicates the line of shift. The distance of shift is indicated by the size of the blue and red ”plumes”. The direction depends on the sense of the respective amphidrome. The example shows a clockwise propagation shifted to the right (or eastward), producing positive values in the upper (northern) part. An anti-clockwise amphidrome moved to the left (or westward) would produce the same pattern. Examples can be found in Fig.4.7 off the Namibian coast (roughly at 10°E, 20°S) and near Galapagos (roughly at the equator and 90°W).

affects the eigen-oscillation of 31.73 hours in the circum-antarctic Kelvin wave. This eigen-oscillation is the most significant constituent of most tides of the diurnal band including the $P_1$ (Zahel and Müller, 2005).

The differences in amplitudes $dA_{pt} = A_{pt}^{pt} - A_{pt}^{eph}$ (Fig. 4.5, bottom) and phases $d\phi_{pt} = \phi_{pt}^{pt} - \phi_{pt}^{eph}$ (Fig. 4.7) of the $P_1$-tide show positive values (red) where the results from the partial tide forcing have higher values. In the open ocean, the two simulations generally agree with each other. The most significant differences in amplitudes and phases are found in extended shelf areas. The difference in amplitudes (Fig. 4.5, bottom) lies between 0.0 and 1.0 cm throughout almost the entire ocean basins with a few areas of negative values up to -1.0 cm. In case of the $P_1$-tide this is most pronounced in the adjacent seas of the western Pacific from northern Australia to Kamchatka and Alaska with differences in amplitudes of up to ± 20 cm. Smaller differences in amplitudes are found in the adjacent seas of the North Atlantic, namely the Labrador Sea and the North Sea, where also considerable changes in the phases can be observed (Fig. 4.7). Phase values generally differ between $\pm 5°$. Some distinct point-centred colour patterns can be seen which are related to a shift in the locations of amphidromes (Fig. 4.8), e.g. west of the Namibian coast (roughly at 10°E, 20°S).

In order to demonstrate the significant differences in oscillations in shelf areas, three different shelf regions and three partial tides will be shown:

1. the $O_1$-tide in the North Sea, English Channel and parts of the North Atlantic (Figure 4.9);
2. the $N_2$-tide on the Patagonian Shelf and parts of the South Atlantic (Figure 4.10); and
3. the $M_2$-tide in the Bohai and Yellow Sea and parts of the Western Pacific (Figure 4.11).

All three areas include extended shelf regions which are located in the immediate vicinity of an ocean and where high tidal amplitudes are observed. Note that the depth of the southern North Sea (Fig. 4.9), the eastern Yellow Sea and Bo-hai (Fig. 4.11) is only a few metres for large parts. The $O_1$ is the strongest diurnal and the $M_2$ the strongest semi-diurnal tide. The Patagonian Shelf (Fig. 4.10) is known to experience pronounced resonance for semi-diurnal tides and with the $N_2$-tide a comparably weaker partial tide has been chosen. The three shown combinations of partial tide and shelf region may serve as illustrative examples where the changes are pronounced but not extreme, which means that a large number of other combinations would have been possible. All results shown are excerpted from global 5' simulations. All partial tide charts extracted from real-time series stem from one single simulation with complete forcing.

### 4.2.1 The $O_1$-Tide in the North Sea Area

The principal lunar diurnal $O_1$ is the strongest tide of the diurnal tidal band. Figure 4.12 shows the propagation of the $O_1$ in the North Sea. The wave travels from the North Atlantic across the Scotland-Faeroe-Ridge into the North Sea, and then anti-clockwise along the British and Dutch coasts into the German Bight. The highest amplitudes with more than 40 cm are found along Britain's east coast. The $O_1$ also travels from the North Atlantic northward into the Irish Sea and eastward into the English Channel.

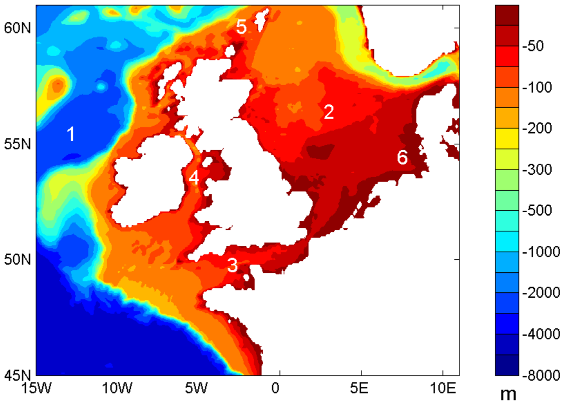

Figure 4.9: Bathymetry showing 1) North Atlantic, 2) North Sea, 3) English Channel, 4) Irish Sea, 5) Scotland-Faeroe-Ridge, and 6) German Bight.

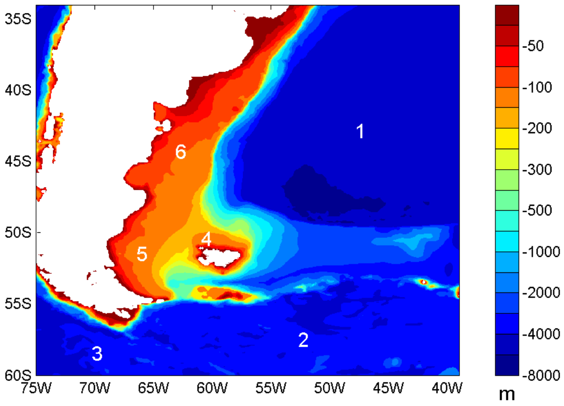

Figure 4.10: Bathymetry showing 1) South Atlantic, 2) Southern Ocean, 3) Drake Passage, 4) Falkland Islands, 5) Southern Patagonian Shelf, and 6) Northern Patagonian Shelf.

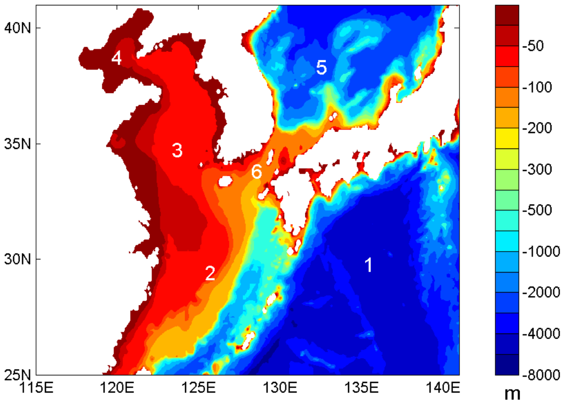

Figure 4.11: Bathymetry showing 1) Pacific Ocean, 2) East China Sea, 3) Yellow Sea, 4) Bo-Hai, 5) Sea of Japan, and 6) Korean Strait.

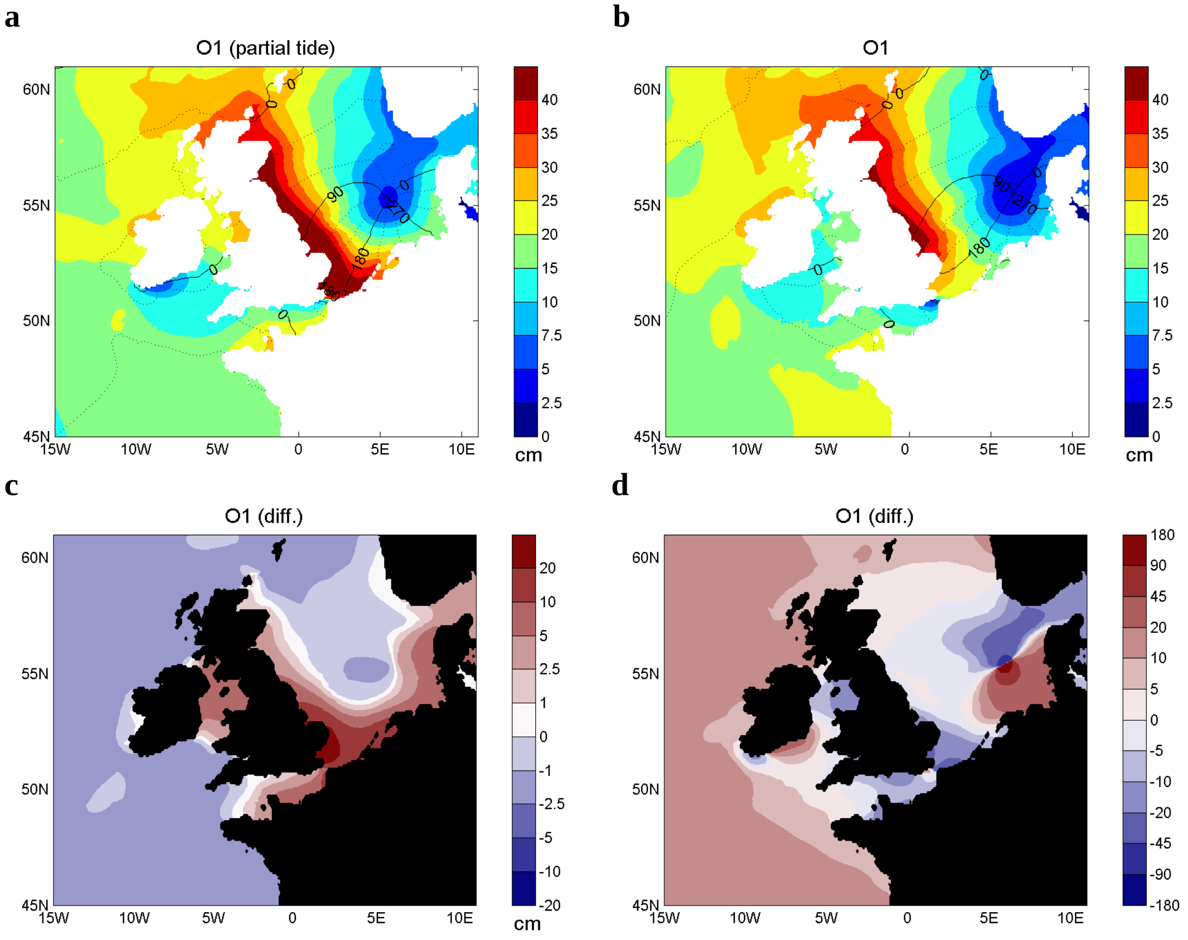

Figure 4.12: Amplitudes and phases of the $O_1$ in the North Sea area with partial tide forcing (a) and complete forcing (b) and differences in amplitudes (c) and phases (d).

The amplitudes of this tide in the Atlantic are generally higher in the simulations with complete forcing by a few centimetres (Fig. 4.12c). On the shelf areas, however, the full forcing results in considerably lower values. The strongest reduction in elevations can be found in the southwesternmost corner of the North Sea. Reduced from 40 cm (partial) to 20 cm (full), the amplitude is halved by interactions within the complete tidal dynamics. Further reductions are observed in the Irish Sea, the English Channel and the German Bight.

The difference in phases (Fig. 4.12d) shows that the $O_1$ partial tide leads the extracted $O_1$ by some 10 degrees in the North Atlantic. In the shelf regions, there are relatively small differences in the phases except for a shift of the location of the amphidromic point in the southern North Sea. Following the conceptual explanation provided in Figure 4.8, the anti-clockwise amphidrome as extracted from the complete forcing simulation has been moved northeastward towards the Danish coast compared to the results of the partial tide forcing simulation.

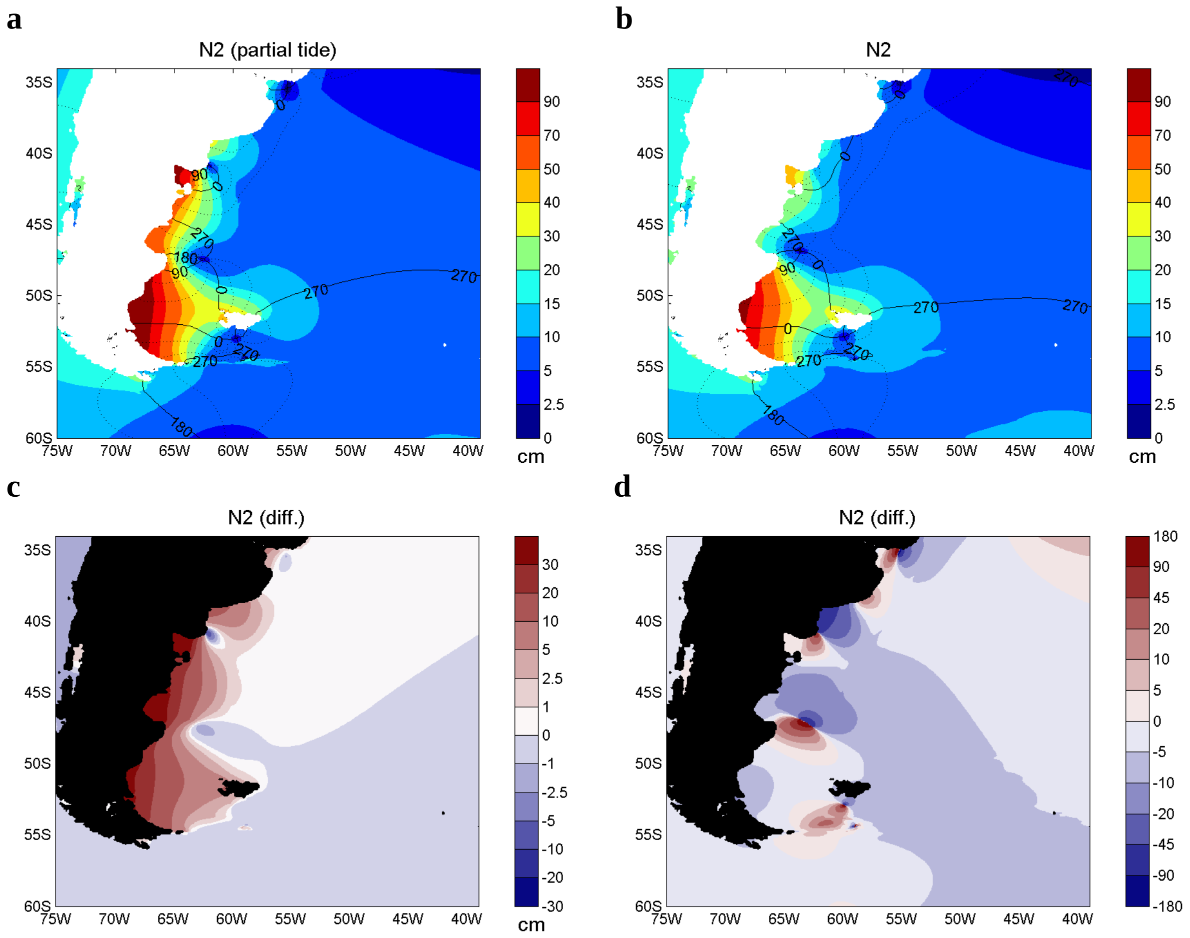

Figure 4.13: Amplitudes and phases of the $N_2$ on the Patagonian Shelf with partial tide forcing (a) and complete forcing (b) and differences in amplitudes (c) and phases (d).

### 4.2.2 The $N_2$-Tide in the Patagonian Shelf Area

The $N_2$-tide is the larger lunar elliptic semi-diurnal constituent of first degree and flows onto the Patagonian Shelf partly from the Southern Ocean and partly from the Pacific Ocean through the Drake Passage (Fig. 4.13). The $N_2$ experiences, like most semi-diurnal tides, pronounced resonance on the Patagonian Shelf due to favourable dimensions of the ocean basins. Amplitudes here can exceed 1 m, which is quite substantial for this otherwise comparably weak partial tide. The wave propagates further northwards along the South American east coast with an amphidrome at around 47°S, 64°W where parts of the $N_2$ from the South Atlantic joins with the northward propagation.

The differences in amplitudes between the results of the two forcings are minimal in the deep ocean part (Fig. 4.13c) with ±1 cm. The differences on the shelf, however, can reach up to 30 cm near the coast. For the region south of 47°S this means a reduction by about 1/3, north of

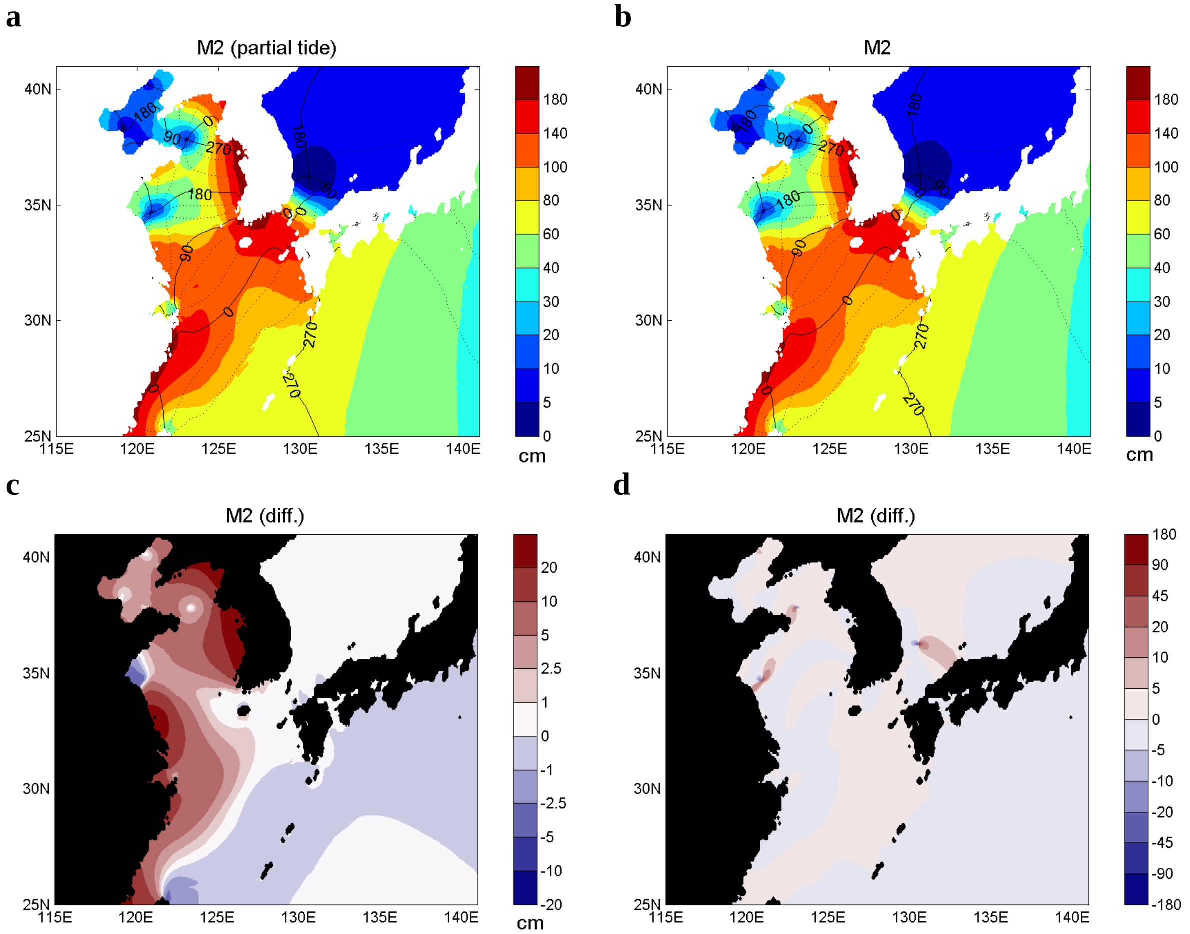

Figure 4.14: Amplitudes and phases of the $M_2$ in the Yellow Sea with partial tide forcing (a) and complete forcing (b) and differences in amplitudes (c) and phases (d).

47°S by 1/2. The differences in phases (Fig. 4.13d) reveal a slight tendency towards a lead of the extracted partial tide in the open ocean. The amphidrome on the Northern Patagonian Shelf has moved eastward towards the Argentinian coast, while the one south of the Falkland Islands shifted slightly to the west.

### 4.2.3 The $M_2$-Tide in the Yellow Sea Area

The principal lunar tide $M_2$ is the most dominant partial tide. The $M_2$-tide propagates from the Pacific Ocean along the Japanese coast into the Yellow Sea and travels further as a continuous wave front northwestward into the Bohai Sea (Fig. 4.14). The highest amplitudes are up to 2 m at the Korean coast.

Major differences in amplitudes are found along the Korean coast and the Chinese coast between 25°N and 35°N (Fig. 4.14c). The amplitude differences can locally exceed 20 cm and reveal a reduction of 10 to 20%. Note that the area of the Korean Strait and northernmost East China Sea is high in absolute amplitudes (Fig. 4.14a and b) with almost no differences observed between partial and full forcing (Fig. 4.14c). Differences in phases are generally less then ± 5 degrees.

### 4.2.4 Interpretation

As an overall impression, the accordance of partial tide and complete forcing in describing the respective oscillation systems is striking. This demonstrates that the partial tides investigated are well captured by the new approach and that the applied harmonic analysis works properly. Clearly, the main differences are found in regions of shallow waters where the respective partial tides reach high amplitudes.

The three regional examples demonstrate the significance of non-linearities within the tidal oscillation system. The $O_1$-tide in the North Sea is an example of a strong diurnal tide in an area which is not necessarily prone to resonance. The second example shows the $N_2$-tide on the Patagonian Shelf, i.e. a relatively weaker semi-diurnal partial tide in an environment strongly influenced by resonance. Both show reductions in amplitudes of up to 50% when using complete forcing instead of partial tide forcing. The third example, the $M_2$-tide in the Yellow Sea, shows a strong semi-diurnal tide in an area which is characterised by strong resonance. The reduction in amplitudes is less compared to the other two examples, yet still significant with differences of up to 20%.

A great deal of these changes can be attributed to the formation of shallow-water tides due to non-linear interactions between partial tides.

## 4.3 Shallow-Water Tides

In contrast to astronomical tides, shallow-water tides do not describe a certain aspect of the relative motion of a tide-generating celestial body. Consequently, they can not be directly derived from the astronomical tidal potential as formulated in Equation 2.10. This also means that they can not be included in schemes that apply partial tide forcing. The non-linear differential equations in the oceanic module of TiME allow for the formation of shallow-water tides in areas of low water depth by interactions between partial tides. With the new approach of the complete forcing, all partial tides of the the second degree tidal potential are included. With the implementation of the high resolution of 5 minutes globally, the shelf areas where shallow-water tides generate are resolved.

Any combination of astronomical tides is possible, and the resulting ”compound tides” can be described by adding (or subtracting) the respective astronomical arguments. This phenomenon also precisely defines the frequencies of the shallow-water tides, and, consequently, they can be included in the harmonic analysis (Section 2.4). In this study, the most important shallow-water tides have been considered (Table A.2).

In the following, one selected compound tide resulting from the interaction of the partial tides described in Section 4.2 and the principal lunar tide $M_2$ will be shown as illustrative examples.

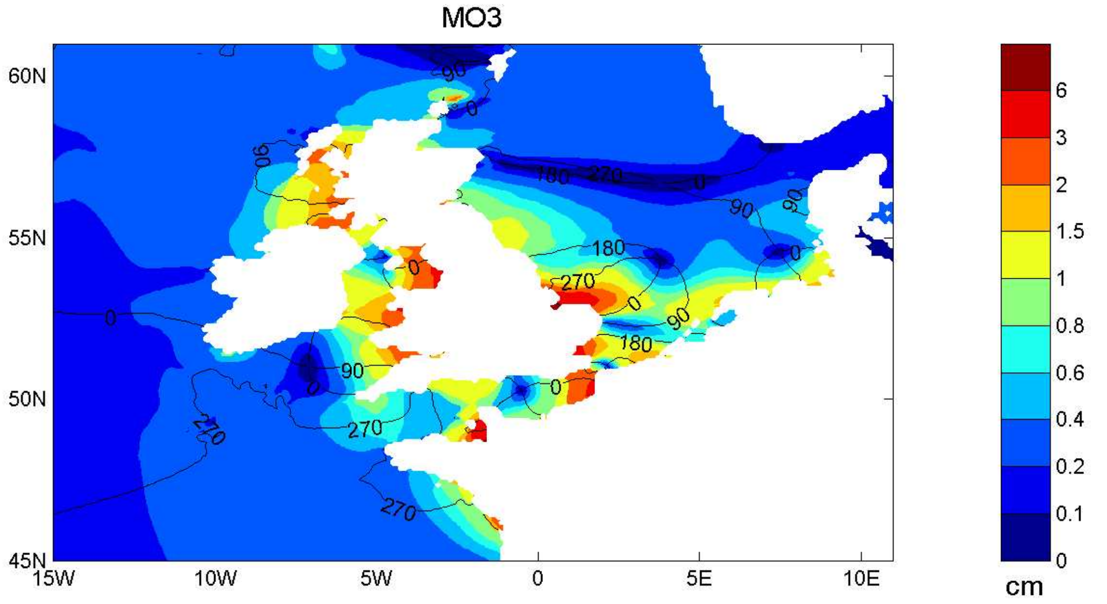

Figure 4.15: Amplitudes and phases of $MO_3$ in the North Sea area.

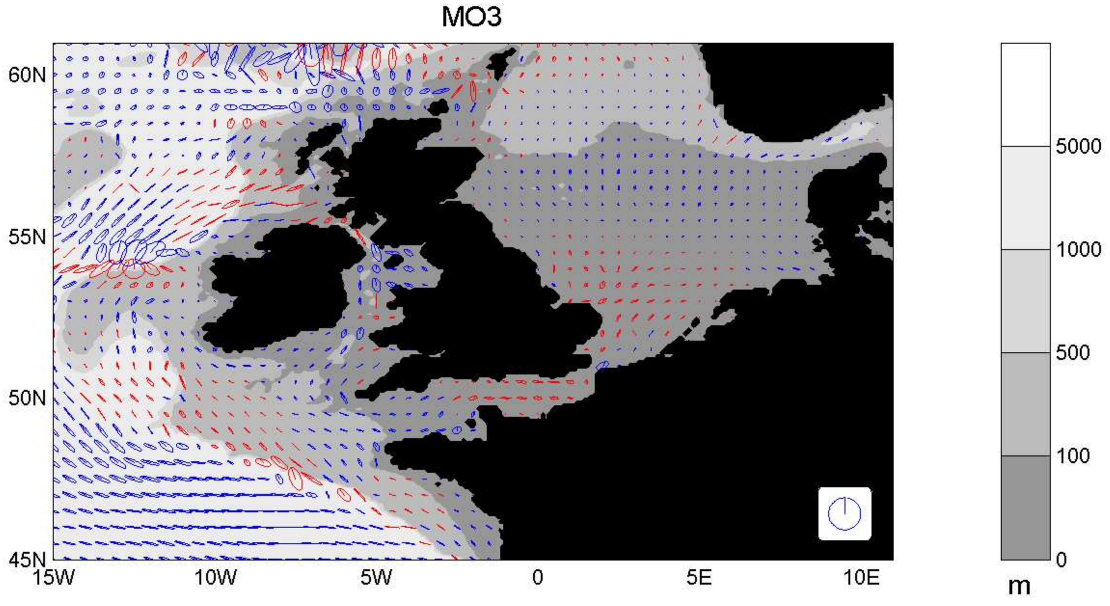

Figure 4.16: Transport ellipses of $MO_3$ in the North Sea area. Water depths are shown in grey shading. A ”legend” tidal ellipse has been added to the figure in the lower right corner. It represents a current characterised by $U = V = 1\frac{m^2}{s}$ and $\phi_U = 90°$ and $\phi_V = 0°$. Cyclonic tidal ellipses are drawn in red (i.e. clockwise in the southern and ant-clockwise in the northern hemisphere).

### 4.3.1 The $MO_3$-Tide in the North Sea Area

The interaction of $O_1 + M_2$ results in the third-diurnal tide $MO_3$. The frequency is determined by

$$\sigma_{M_2} + \sigma_{O_1} = \sigma_{MO_3} \tag{4.1}$$

with $\sigma_{M_2} = 29.984104\ °/h$ and $\sigma_{O_1} = 13.943036\ °/h$ this results in $\sigma_{MO_3} = 42.927140\ °/h$ and gives a period of about 8 hours and 23 minutes.

The highest amplitudes of the $MO_3$ in the North Sea (Fig. 4.15) are found essentially in the same areas as the ones where the biggest amplitude differences between partial and complete forcing are observed (Fig. 4.12). The $MO_3$ reaches its highest values of up to 6 cm along the coasts of the British Isles. A similar anti-clockwise path is observed for the $MO_3$ in the southern North Sea, as for the $O_1$ (Fig. 4.12) albeit with a different speed. Also, the amphidrome at 4°E, 57°N indicates that the $MO_3$ does not flow across the Scotland-Faeroe-Ridge into the northern North Sea (as it was the case with the $O_1$) but rather in the opposite direction, i.e. from the Scottish east coast northward out into the North Atlantic. Other amphidromes form in the Southern North Sea (4°E,55°N), German Bight (7°E,55°N), English Channel (1°W,50°N) and south of Ireland (7°W,51°N).

In the deeper areas of the North Atlantic, the $MO_3$ contributes almost nothing to the sea surface elevations. The cotidal lines, however, suggest a quite distinctive propagation of a wave with the analysed frequency. Flow transports describe the volumes of water that are being moved due to currents and are shown for the $MO_3$ in the North Sea in Figure 4.16.

The transport of partial tides with fixed periods can be represented by amplitude and phase values. Ocean transport pattern can therefore be described by a tidal ellipse with the solid line indicating the transport current at 0° and the elliptic line indicating the change in direction and amount of the tidal transport over 360° (i.e. a full period).

Most of the transport of the $MO_3$ can be found in the North Atlantic part of the excerpt (Figure 4.16). This is confirmation that while shallow-water tides predominantly form in shelf areas the $MO_3$ indeed propagates through the open ocean, albeit as comparably weak currents with transports only locally exceeding 1 $m^2/s$. In contrast, the partial tide $M_2$ can transport up to 500 $m^2/s$ over large regions of the Atlantic. The highest values of the $MO_3$ transport can be seen along the shelf breaks and near the Iceland-Faeroe-Ridge (at the top-edge of Figure 4.16). Relatively strong currents are also observed in the Irish Sea. The values in the North Sea itself are low as water depth is less then 50 metres over large parts.

### 4.3.2 The $MN_4$-Tide in the Patagonian Shelf Area

The amplitudes and phases of the fourth diurnal tide $MN_4$ ($M_2 + N_2$) are shown for the Patagonian Shelf (Fig. 4.17). Again, the highest amplitudes (up to 10 cm) are clearly associated with the regions that display the strongest reduction due to the implementation of the complete forcing (Fig. 4.13). The $MN_4$ has an amphidromic point on the Patagonian Shelf itself (at roughly 52°S, 67°W) where the wave propagates clockwise. After moving northward along the coast, it leaves the shallow waters and spreads out into the South Atlantic. Though the amplitude values

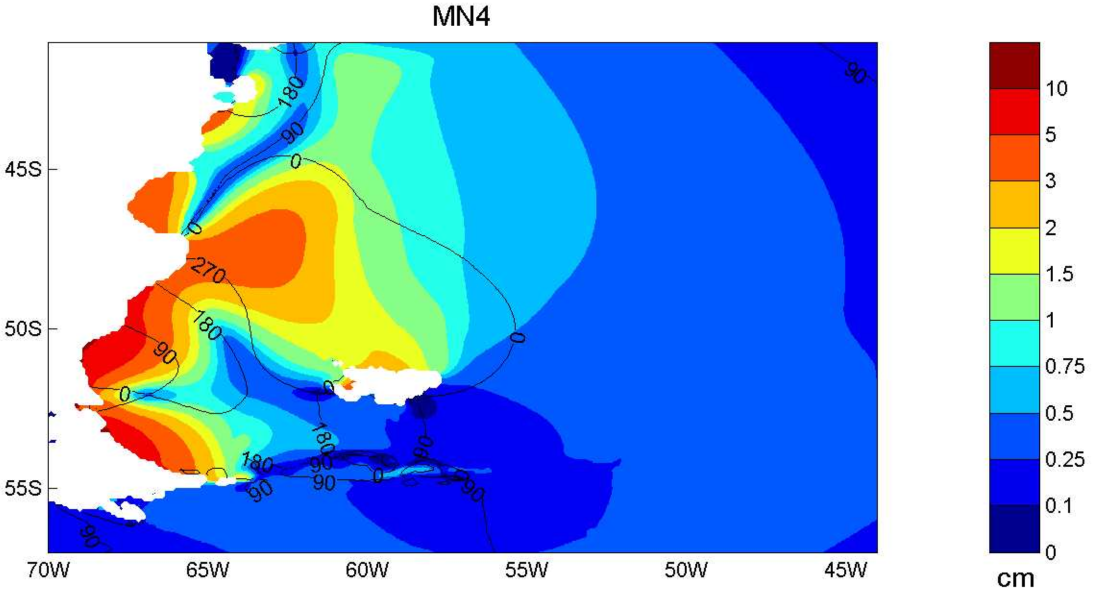

Figure 4.17: Amplitudes and phases of $MN_4$ on the Patagonian Shelf.

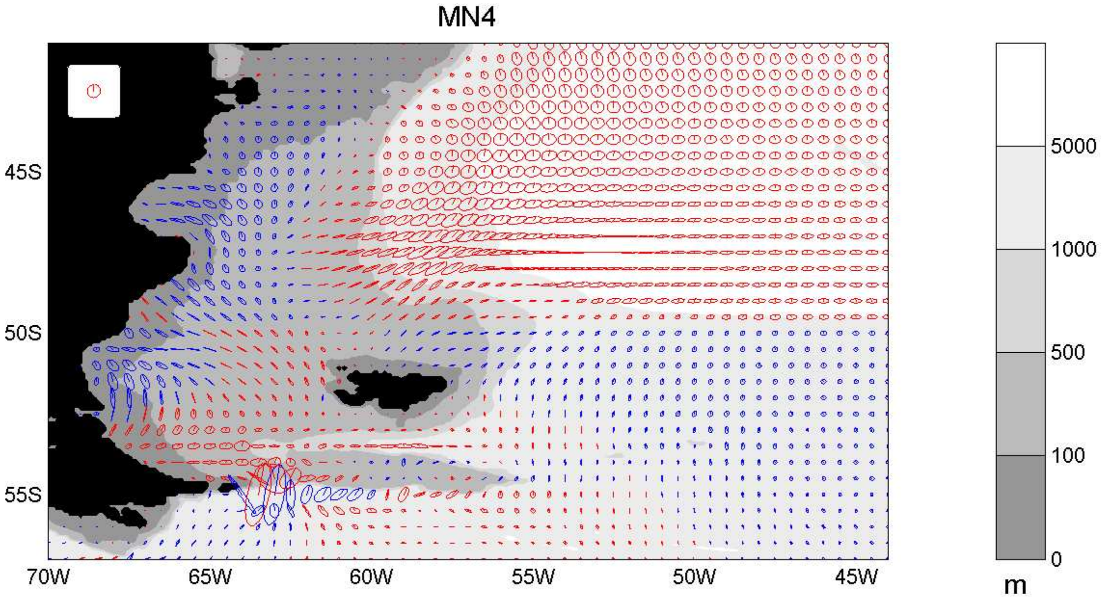

Figure 4.18: Transport ellipses of $MN_4$ on the Patagonian Shelf, as in Fig. 4.16 except that as this is in the southern hemisphere the ”legend” tidal ellipse (upper left corner) now is cyclonic (red).

seem to level off at further distances, the very uniform phase propagation suggests that the wave is still detectable far out in the open ocean.

This finding can be verified by the description of the water transport (Fig. 4.18) where the propagation of the $MN_4$ into the South Atlantic is demonstrated by large ellipses. In contrast to the $MO_3$ in the North Sea (Fig. 4.16) transport values on the shelf itself are quite pronounced. As flow transport is the product of depth and velocity and the Patagonian Shelf is characterised by shallow waters, this indicates that the described compound tide reaches substantial velocities on the Patagonian Shelf. The largest values of flow transport can again be found at the shelf break (e.g. 64°W, 55°S).

### 4.3.3 The $M_4$- and $2SM_2$-Tide in the Yellow Sea Area

The third example is of the interaction of the $M_2$ with itself, the $M_4$ compound tide, an example of an ”overtide” (Fig. 4.19). The $M_4$-overtide in the Yellow Sea basically redraws the picture of the $M_2$ with a doubled speed: the main propagation is northward in the Yellow Sea with amplitudes of up to 10 cm at the Korean coast into the Bohai Sea. The $M_4$, however, exhibits its highest values in the inner Yellow Sea while the $M_2$ has a pronounced maximum at the southern end of the Yellow Sea and the East China Sea (Fig. 4.14). The transports shown in Figure 4.20 show northwestward propagation into the Bohai Sea, northward propagation into the Sea of Japan and throughflow between the Pacific Ocean and the East China Sea. Overtides are the only shallow-water tides that can also be captured by a numerical model that is forced by a single partial tide and applies non-linear shallow water equations. Consequently, it is not related to the differences seen in Figure 4.14.

Compound tides can be formed by adding the fundamental arguments of the astronomical partial tides, and can also be formed by subtraction or combinations of both. One remarkable feature of this phenomenon is that some combinations will have similar or identical arguments as an astronomical partial tide. For example, the compound tide $2MS_2 = M_2 + M_2 - S_2$ has an identical frequency as the variational lunar tide $\mu_2$ (Bartels, 1957). In a slightly different combination, though, $S_2 + S_2 - M_2$ results in the semi-diurnal shallow-water tide $2SM_2$ which has no corresponding astronomical counterpart.

Similar to the $M_2$ and $M_4$, the $2SM_2$ also travels through the Yellow Sea along the Korean coast, where the highest amplitudes of more than 4 cm are found, into the Bohai (Fig. 4.21). The areas of highest amplitudes of the $2SM_2$ are the same as the areas with highest differences in Figure 4.14, i.e. at the Korean westcoast and western part of the Yellow Sea.

A conspicuous phenomenon can be seen in the westernmost part of the East China Sea (at about 122°E, 29°N): the $2SM_2$ has a pronounced maximum of about 2 cm and the phase lines seem to spread out in a concentric way from this location. This may indicate that parts of the $2SM_2$ are generated directly at the coastline by interactions of $M_2$ with $S_2$ and that the $2SM_2$ moves off the coast into the East China Seas afterwards.

The compound tide also travels across the Korean Strait into the Sea of Japan where it forms an amphidrome. The cotidal line of 270° in the Pacific Ocean south of Japan shows that the $2SM_2$ propagates eastward into the East China Sea. This suggests that this part of the tide has not

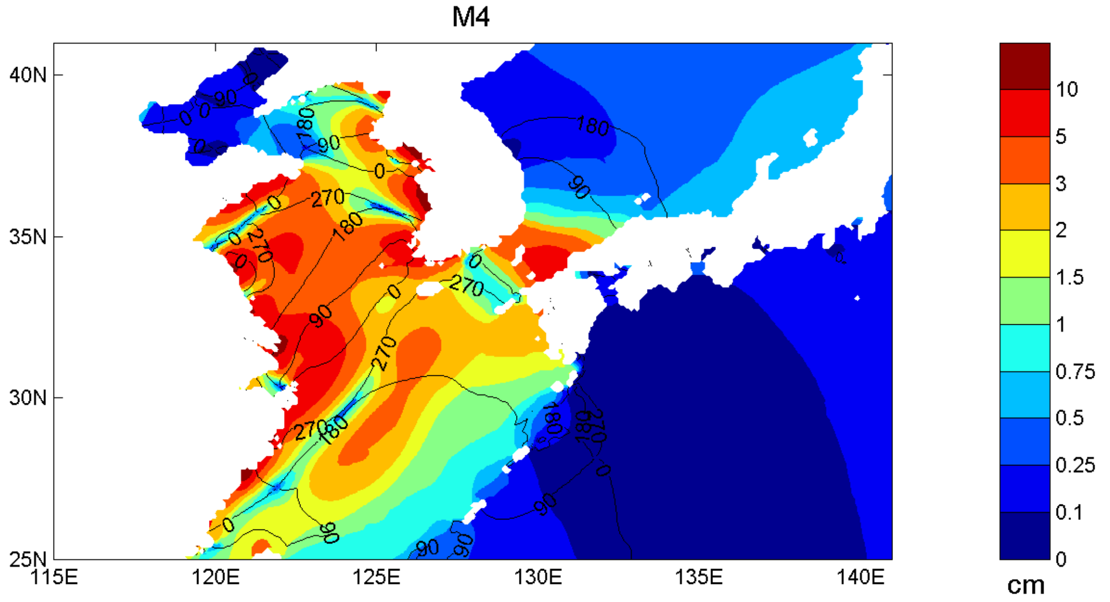

Figure 4.19: Amplitudes and phases of $M_4$ in the Yellow Sea.

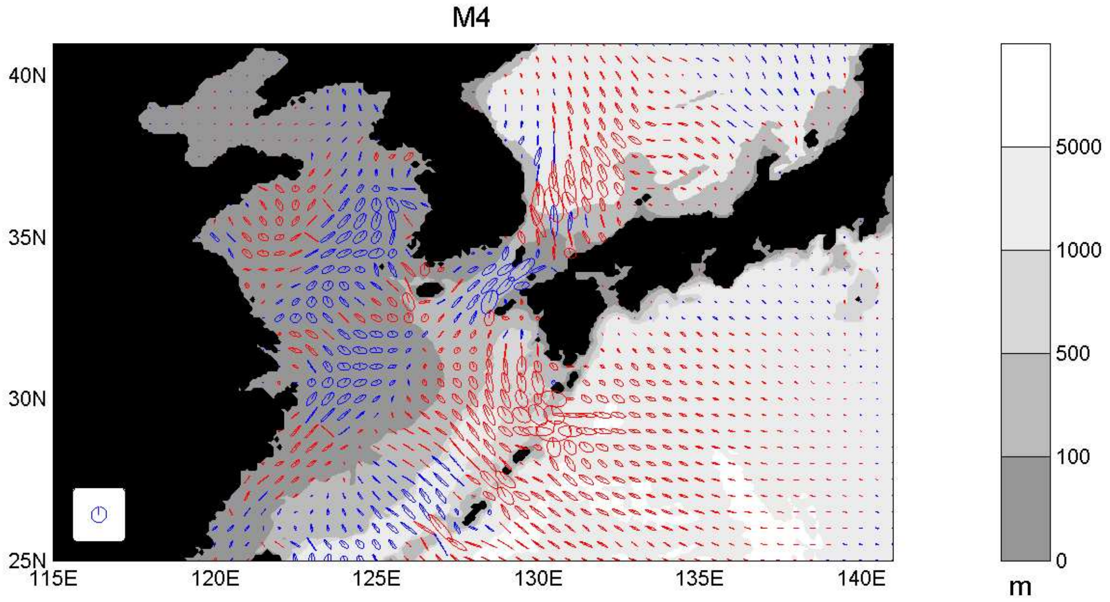

Figure 4.20: Transport ellipses of $M_4$ in the Yellow Sea area as in Fig. 4.16.

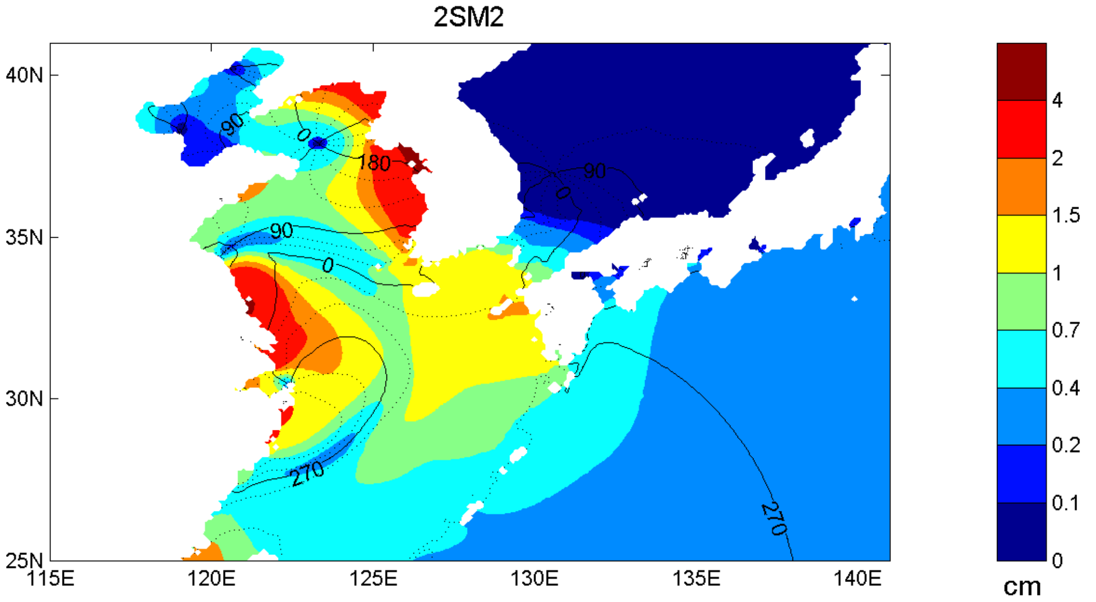

Figure 4.21: Amplitudes and phases of $2SM_2$ in the Yellow Sea.

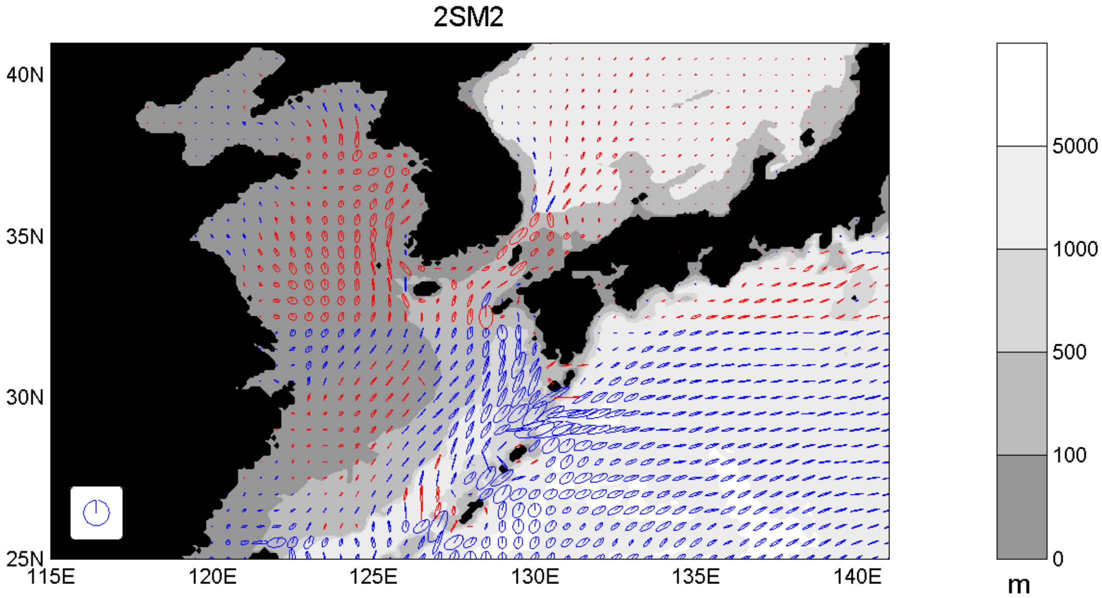

Figure 4.22: Transport ellipses of $2SM_2$ in the Yellow Sea area as in Fig. 4.16.

been formed in the Yellow Sea but rather is an already existing component of the tidal currents moving southward along the coastlines of the Western Pacific.

The transport ellipses (Fig. 4.22) confirm the eastward flow in the Pacific Ocean south of Japan, the northward propagation across the Yellow Sea into the Bohai. The strongest transport can be found in the Korean Strait and in the narrow straits between the archipelago of the Ryukyu Islands dividing the East China Sea from the Pacific Ocean, where transport can reach values of up to 1 $\frac{m^2}{s}$.

### 4.3.4 Sixth- and Eighth-Diurnal Tides

Given the harmonic analysis performed for this study, a few sixth-diurnal and eighth-diurnal tides (periods of about 3 and 4 hours) were also included in this analysis. Their formation is analogue to the ones described in the examples above. Representations of the $2MS_6$ on the Patagonian Shelf and the $3MS_8$ in the North Sea can be found in Appendix A.3. The significance of the shallow-water tides decreases with increasing frequency. The two shown compound tides barely exceed amplitudes of 2 cm. The results do, however, document that these tides are captured by the model and that they can also be traced far out in the open ocean.

# Chapter 5

# Angular Momentum and the Earth's Rotation

The influence of the tidal oscillation system (Chapter 4) on the rotational behaviour of the earth will be analysed. The new real-time approach offers two different ways for the investigations. First, the complete effect of the tidal oscillation system from the lunisolar tidal potential of second degree can be described. Second, every extracted partial tide can be described separately in the frequency-domain. Section 2.4 gives a description of the selection criteria and the procedure for this harmonic analysis. Some additional partial tides were also investigated by a harmonic analysis of the the time-series of the angular momentum calculated from the simulations with complete forcing (Table A.2).

The advantage of the representation in the frequency-domain are fixed periods. The results for any partial tide are time-invariant and can be presented in a more comprehensive form. Furthermore, they can be compared to results from measurements and other models related to partial tides.

The description of the oceanic tidal angular momentum (Section 5.1) is followed by the analysis of the instantaneous angular momentum budgets (Section 5.2). Energy dissipation due to eddy-viscosity and bottom friction and their long-term effects on the earth's rotation will be discussed (Section 5.3) and the influence of the ocean tides on the earth rotation parameters, i.e. length of day and polar motion, is investigated (Section 5.4).

## 5.1 Oceanic Tidal Angular Momentum

The oceanic tidal angular momentum (AM) is influenced by tidal elevations and currents and is divided into rotational and relative angular momenta (Section 2.3.1). Rotational, relative and total AM for 21 days in June 2002 for the x-, y- and z-components is shown in Figure 5.1. The time-series reveals a pronounced fortnightly cycle in the amount of AM in both rotational and relative angular momentum as well as in all three components. The highest values in the excerpt of Figure 5.1 are found in the y-component around June 14 2002 with a range of $-6$ - $4 \cdot 10^{25}\,\frac{kg \cdot m^2}{s}$ for relative and $\pm 4 \cdot 10^{25}\,\frac{kg \cdot m^2}{s}$ for rotational angular momentum. The total angular momentum reaches maxima of $-6$ - $8 \cdot 10^{25}\,\frac{kg \cdot m^2}{s}$.

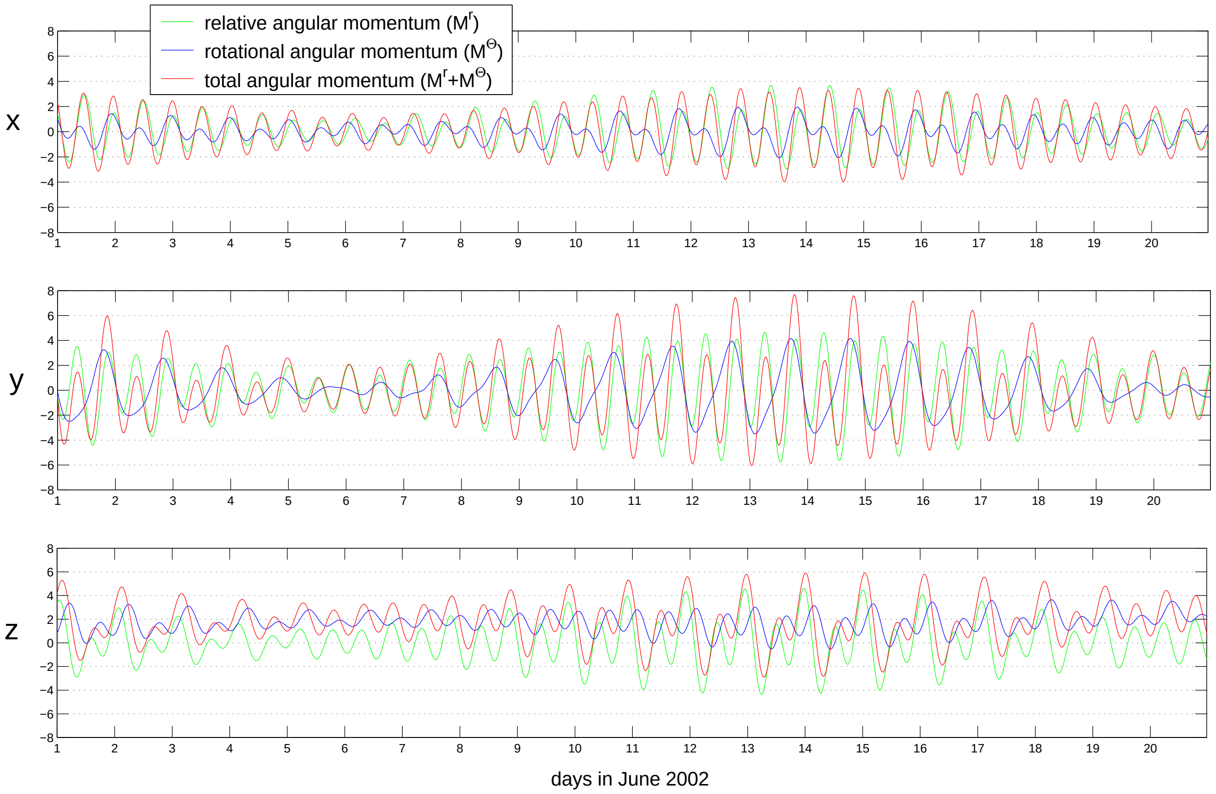

Figure 5.1: Relative and rotational angular momentum in $10^{25}\frac{kg\cdot m^2}{s}$ calculated by TiME with 5' resolution for the equatorial components x and y and the axial component z (time-domain).

The y-component of the relative AM, $M_y^r$ (Equation 2.17), is dominated by semi-diurnal variations. Every second semi-diurnal peak is reduced due to diurnal variations. This effect is stronger for negative values of $M_y^r$ where the difference of two neighbouring semi-diurnal peaks can be up to $2 \cdot 10^{25}\,\frac{kg\cdot m^2}{s}$.

The y-component of the rotational AM, $M_y^\Theta$, is dominated by diurnal variations. Throughout large parts of the time-series, these diurnal oscillations are asymmetric: the time-span from peaks of positive value to negative ones is considerably shorter than the time-span from negative to the subsequent peak of positive value. Note that the ratio of the time-span of decreasing values against the time-spans where values of $M_y^\Theta$ increase is nearly $1 : 3$. This means that the curve can also be interpreted as a semi-diurnal variation where every third and fourth semi-diurnal peak simply does not develop.

The total of relative and rotational AM is dominated by semi-diurnal variations which also vary from one neighbouring peak to the next. The highest values are observed when relative and rotational AM have their respective positive maxima in phase with each other. As the ”absent” semi-diurnal peaks in $M_y^\Theta$ occur simultaneously with the absolute maximum peaks in $M_y^r$, relative and rotational AM are out of phase and consequently result in reduced values in total AM. This constellation results in the phenomenon that even though relative AM has stronger negative than positive peaks, the total AM reveals stronger positive than negative peaks. In general, $M_y^r$ is more significant than $M_y^\Theta$ especially during periods of low amplitudes (e.g. June 4-8) where $M_y^{tot} \cong M_y^r$.

Values of AM of the x- ($\pm 4 \cdot 10^{25} \frac{kg \cdot m^2}{s}$) and z-component ($-4$ - $6 \cdot 10^{25} \frac{kg \cdot m^2}{s}$) are generally lower than for the y-component. $M_x^r$ is (as for $M_y^r$) dominated by semi-diurnal variations with diurnal variations producing an inequality of neighbouring peaks. Again, the rotational AM $M_x^\Theta$ is influenced by diurnal tides more strongly than is $M_x^r$. The influence of the semi-diurnal tides is more pronounced for $M_x^\Theta$ than for $M_y^\Theta$. $M_z^r$ reveals a similar pattern as $M_x^r$ and $M_y^r$ in the combination of diurnal and semi-diurnal variations. For $M_z^\Theta$, an off-set of about $1 \cdot 10^{25} \frac{kg \cdot m^2}{s}$ towards positive values is visible. This can be attributed to the effect of long-period tides, most likely the influence of the semi-annual tide $Ssa$ and the annual tide $Sa$.

The fornightly patterns displayed by all three components (x, y and z) result from the fortnightly partial tides, e.g. $Mf$ and $MSf$, and the superimposition of semi-diurnal and diurnal partial tides, e.g. the combination of $M_2$ and $S_2$ leads to a fortnightly cycle with highest values when the two tides are in phase.

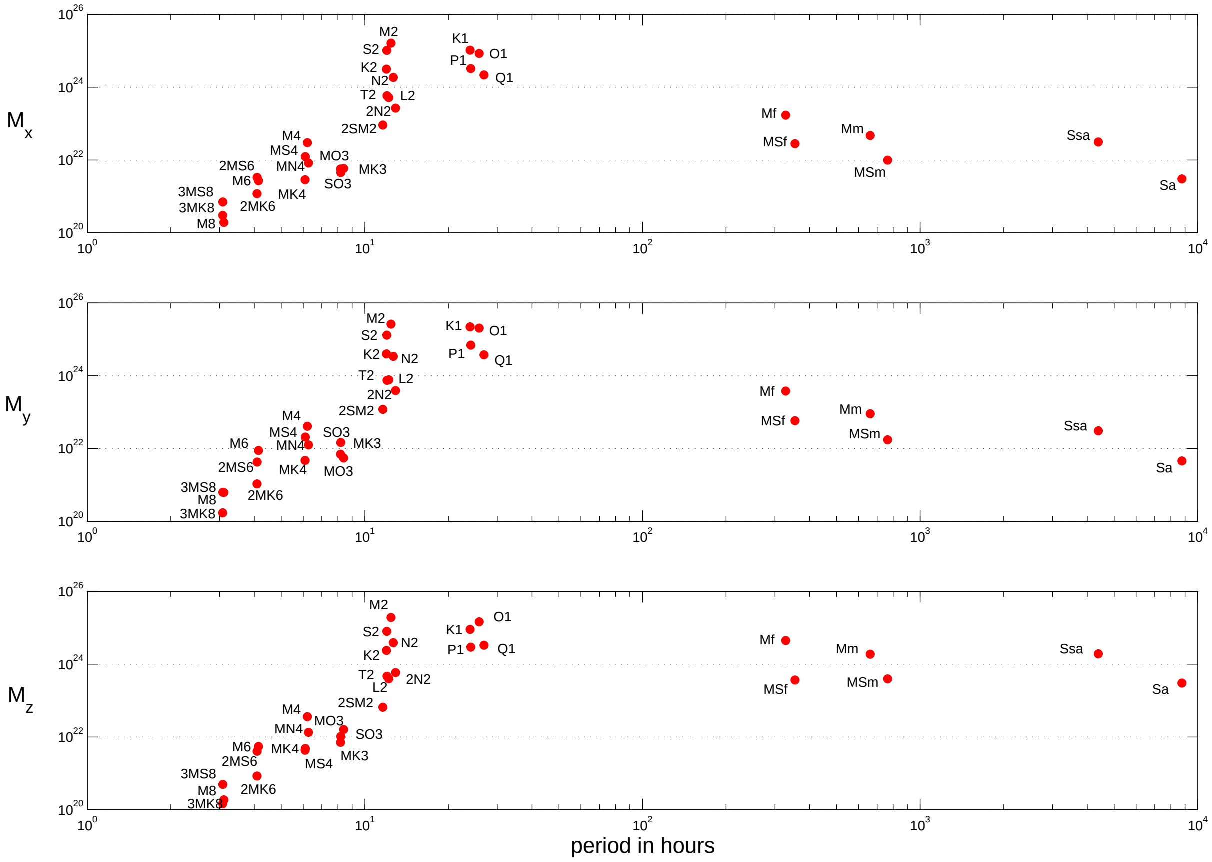

Figure 5.2: Amplitudes of total angular momentum in $10^{25} \frac{kg \cdot m^2}{s}$ calculated by TiME with 5' resolution (frequency-domain). Note that both axes use a logarithmic scale.

Table 5.1: Relative ($M^r$) and Rotational ($M^\Theta$) Angular Momentum of Long-Period Tides

| tide | model | $M_x^r$ | | $M_y^r$ | | $M_z^r$ | | $M_x^\Theta$ | | $M_y^\Theta$ | | $M_z^\Theta$ | |
|---|---|---|---|---|---|---|---|---|---|---|---|---|---|
| $Sa$ | T | 0.001 | 264° | 0.001 | 220° | 0.001 | 314° | 0.003 | 346° | 0.004 | 155° | 0.302 | 331° |
| $Ssa$ | T | 0.012 | 290° | 0.008 | 262° | 0.016 | 31° | 0.027 | 10° | 0.024 | 220° | 1.912 | 0° |
| | S | 0.011 | 278° | 0.007 | 280° | 0.009 | 89° | 0.026 | 6° | 0.012 | 259° | 1.851 | 2° |
| $MSm$ | T | 0.011 | 306° | 0.007 | 313° | 0.012 | 69° | 0.004 | 60° | 0.011 | 304° | 0.390 | 11° |
| $Mm$ | T | 0.057 | 309° | 0.038 | 317° | 0.073 | 73° | 0.020 | 78° | 0.053 | 301° | 1.854 | 12° |
| | S | 0.062 | 315° | 0.037 | 326° | 0.074 | 91° | 0.043 | 58° | 0.059 | 340° | 1.945 | 11° |
| $MSf$ | T | 0.021 | 296° | 0.020 | 317° | 0.027 | 105° | 0.011 | 235° | 0.043 | 269° | 0.374 | 1° |
| $Mf$ | T | 0.225 | 355° | 0.158 | 12° | 0.339 | 104° | 0.111 | 128° | 0.220 | 11° | 4.330 | 37° |
| | S | 0.127 | 333° | 0.092 | 0° | 0.286 | 98° | 0.093 | 118° | 0.112 | 25° | 3.324 | 16° |

Values shown are amplitudes ($A_i$) in $10^{24}\,\frac{kgm^2}{s}$ and phases ($\phi_i$) in degrees.
Results from TiME with 5’ resolution and complete forcing (T).
Comparisons with the results of Seiler (1991) (S).

As the representation of AM in the time-domain (Figure 5.1) is not convenient for comparisons with measurements or results of other models, it is preferential to investigate AM for individual partial tides in the frequency-domain. Figure 5.2 shows results of the partial tides which were extracted via harmonic analysis of the entire global fields of sea surface elevations and currents (see Section 2.3). Amplitudes range from $10^{20}$ - $10^{26}\frac{kg \cdot m^2}{s}$ and periods from 3 hours to one year are represented.

The most dominant tides are the semi-diurnal and diurnal partial tides. The four most significant of each of the tidal bands ($M_2$, $S_2$, $K_2$, and $N_2$ and $K_1$, $O_1$, $P_1$ and $Q_1$, respectively) exceed $10^{24}\frac{kg \cdot m^2}{s}$ in total AM in all three components. The less important partial tides ($T_2$, $L_2$ and $2N_2$) are lower by roughly one order of magnitude. Partial tides of the long-period tidal band are most dominant in the axial component $M_z$ where they can also exceed $10^{24}\frac{kg \cdot m^2}{s}$ in amplitude ($Mf$,$Mm$ and $Ssa$). Their values in $M_x$ and $M_y$ are lower by at least one order of magnitude.

The high-frequency shallow-water tides on the left-hand sides of Figure 5.2 are even less significant, rarely exceeding $10^{22}\frac{kg \cdot m^2}{s}$ (namely $2SM_2$, $M_4$, $MS_4$, $MN_4$, $MO_3$, and $SO_3$). With increasing period, the shallow-water tides become more important. The most dominant shallow-water tide is the semi-diurnal tide $2SM_2$, followed by the fourth-diurnal and the third-diurnal tides. The eighth-diurnals reach $10^{21}\frac{kg \cdot m^2}{s}$ and have values five orders of magnitude lower than, for example, the predominant semi-diurnal tides.

In the following, the results of this study will be described in more detail and compared 1) with the model results from Seiler (1991), which is a 1° partial tide model and the precursor of TiME, and 2) with results from the data assimilation model of Zahel et al. (2000) which also utilises 1° resolution. These two models were selected because they are similar to the presented model TiME in the basic principles and equations. Differences in the results of angular momentum will reflect on the differences of the general approaches, i.e. a high-resolving real-time model compared with a coarser-resolving partial tide model and a data assimilation model.

Table 5.2: Relative ($M^r$) and Rotational ($M^\Theta$) Angular Momentum of Diurnal Tides

| tide | model | $M_x^r$ | | $M_y^r$ | | $M_z^r$ | | $M_x^\Theta$ | | $M_y^\Theta$ | | $M_z^\Theta$ | |
|---|---|---|---|---|---|---|---|---|---|---|---|---|---|
| $Q_1$ | T | 0.077 | 281° | 0.047 | 246° | 0.194 | 77° | 0.176 | 349° | 0.344 | 194° | 0.144 | 98° |
| | Z | 0.049 | 306° | 0.068 | 214° | 0.147 | 117° | 0.109 | 339° | 0.256 | 218° | 0.073 | 128° |
| $O_1$ | T | 0.424 | 292° | 0.416 | 163° | 0.945 | 101° | 0.453 | 326° | 1.728 | 211° | 0.592 | 138° |
| | S | 0.204 | 262° | 0.185 | 112° | 0.851 | 114° | 0.489 | 14° | 1.533 | 217° | 0.516 | 107° |
| | Z | 0.225 | 299° | 0.409 | 210° | 0.644 | 124° | 0.474 | 328° | 1.153 | 219° | 0.190 | 144° |
| $P_1$ | T | 0.143 | 295° | 0.248 | 190° | 0.275 | 128° | 0.189 | 320° | 0.488 | 231° | 0.065 | 206° |
| | S | 0.037 | 275° | 0.169 | 213° | 0.240 | 145° | 0.251 | 351° | 0.371 | 228° | 0.047 | 183° |
| | Z | 0.175 | 280° | 0.258 | 191° | 0.245 | 132° | 0.161 | 309° | 0.458 | 223° | 0.044 | 47° |
| $K_1$ | T | 0.466 | 300° | 0.808 | 196° | 0.883 | 136° | 0.599 | 327° | 1.539 | 239° | 0.173 | 224° |
| | S | 0.182 | 234° | 0.380 | 202° | 0.653 | 143° | 0.637 | 358° | 1.134 | 221° | 0.076 | 125° |
| | Z | 0.514 | 286° | 0.785 | 198° | 0.735 | 135° | 0.477 | 308° | 1.387 | 222° | 0.162 | 44° |

Values shown are amplitudes ($A_i$) in $10^{25}\ \frac{kgm^2}{s}$ and phases ($\phi_i$) in degrees.
Results from TiME with 5' resolution and complete forcing (T).
Comparisons with the results of Seiler (1991) (S) and Zahel et al. (2000) (Z).

### 5.1.1 Long-Period Tidal Band

Amplitude ($A$) and phase values ($\phi$) of selected partial tides of the long-period band are presented in Table 5.1 (results from real-time simulations of TiME are marked with ”T”). The rotational AM $M_z^\Theta$ has the highest values for all tides ($0.3$ - $4.3 \cdot 10^{24}\ \frac{kgm^2}{s}$). This is due to the fact that with decreasing frequencies, the oscillation system of the long-period tides get closer to the equilibrium tide (Seiler, 1989). In the $Ssa$-tide, for example, this is shown by the very low amplitude values in $M^r$ and a phase value of $M_z^\Theta$ of $0°$. The results of the $Ssa$ are in very good agreement with the results of Seiler (1991) (S). Only values of $M_y^\Theta$ differ considerably in the two models. The same holds for comparisons of the $Mm$-tide where the main differences are found in $M_x^\Theta$. Long-period tides are very large scale features within the oceanic oscillation system and they can be captured by a relatively coarse model. The agreement of the data of the partial tide model with the results of the real-time model shows that the long-period tides are well-captured by simulations with TiME and that they can indeed be correctly extracted by the harmonic analysis (even with a time-series of only 400 days).

The results of the fortnightly tide $Mf$ are less consistent with the coarser resolving partial tide model. They agree well in the order of magnitude of amplitudes and phases of the respective components, but the results of TiME are generally higher in amplitude by a factor of 1.5 to 2 and, with the exception of $M_y^\Theta$, lead the Seiler-model by some 10° to 20°.

### 5.1.2 Diurnal Tidal Band

Results of the angular momenta of four selected partial tides of the diurnal band - $Q_1$, $O_1$, $P_1$ and $K_1$ (Table 5.2) - show a clear dominance of $M_y^\Theta$. This is in accordance with the interpretations of results in the time-domain (Fig. 5.1) where the rotational AM in the y-component was characterised by diurnal variations. The amplitudes of $M_y^\Theta$ are usually higher by at least a factor of 2 compared to the other five components of the AM. Note that the phase values of $M_y^\Theta$ all lie comparably close to each other (around 220°).

The results of the angular momentum of the diurnal tide $Q_1$ are generally higher in amplitude than the results of the data assimilating model of Zahel et al. (2000) (Z), with the exception of $M_y^r$ (Table 5.2). Phases differ by $\pm 40°$.

Results of TiME for the $O_1$-tide have been compared to the model results of both Seiler (1991) and Zahel et al. (2000). In general, the $O_1$-amplitudes calculated with the partial tide model S agree better with the data assimilation model Z and the high-resolving real-time model T calculates higher values. An exception is $M_y^r$ where T and Z produce an almost identical amplitude. For the amplitudes of the three most significant components ($A_z^r$, $A_y^\Theta$ and $A_z^\Theta$) of the $O_1$, the two free models (T and S) are close to each other and differ considerably from the constrained model Z. Regarding the phase values, however, T and Z give a better fit ($\phi_x^r$, $\phi_y^r$, $\phi_x^\Theta$ and $\phi_z^\Theta$).

Amplitudes of the $P_1$-tide's AM calculated in this study are in very good agreement with the results of the data assimilation model Z. Only in the z-component, S and Z are relatively closer to each other and T shows higher values. Phases are generally in very good agreement for all three models, except for $\phi_z^\Theta$ where the results differ by up to 150°. As $A_z^\Theta$ has lower values than the other components by almost an order of magnitude, this difference is of minor significance.

Similar observations can be made for the $K_1$-tide. The high-resolving real-time model T is in considerably better agreement with the data assimilation model Z than the coarser-resolving partial tide model S. Exception is again $\phi_z^\Theta$ of the similarly weak $M_z^\Theta$-term. Note that the partial tide model S is substantially lower than both T and Z in its amplitude values ($A_x^r$, $A_y^r$, $A_y^\Theta$ and $A_z^\Theta$).

### 5.1.3 Semi-Diurnal Tidal Band

In the semi-diurnal tidal band, $M^r$ clearly dominates over $M^\Theta$ (Table 5.3). The y-component $M_y^r$ has the highest amplitudes and confirms the interpretations made in the time-domain (Fig.5.1), excepting for the $N_2$-tide, where $M_z^r$ is strongest.

All three models agree quite well with each other in the description of the $N_2$. The real-time model T is generally closer to the data assimilation model Z than S ($M_x^r$, $M_z^r$, $M_y^\Theta$ and $M_x^\Theta$).

Results for the principal lunar tide $M_2$ reflect the overestimation of free tidal models discussed earlier (Sections 3.5 and 3.6). This effect is even more pronounced in T than in S ($A_x^r$, $A_y^\Theta$ and $A_z^\Theta$). The data assimilation model Z calculates maximum angular momenta for both $A_y^r$ and $A_z^r$ with about $1.7 \cdot 10^{25}\,\frac{kgm^2}{s}$, while S calculates a distinct maximum in $A_z^r$ and T in $A_y^r$ with about $3 \cdot 10^{25}\,\frac{kgm^2}{s}$ (the respective other component reaching $2.1 \cdot 10^{25}\,\frac{kgm^2}{s}$). All three models agree well in their phase values with Z slightly leading T leading S.

Results of the $S_2$-tide also reveal a tendency towards overestimation of the free models (T and S) as compared to the data assimilation model (Z). T and S agree well in the amplitudes of the equatorial components of relative and rotational AM ($A_x^r$, $A_y^r$, $A_x^\Theta$ and $A_y^\Theta$) and have higher values than Z sometimes by a factor of more than 2. In the axial components $A_z^r$ and $A_z^\Theta$, however, the new model T agrees better with the data assimilation model Z. There is very good

Table 5.3: Relative ($M^r$) and Rotational ($M^\Theta$) Angular Momentum of Semi-Diurnal Tides

| tide | model | $M_x^r$ | $M_y^r$ | $M_z^r$ | $M_x^\Theta$ | $M_y^\Theta$ | $M_z^\Theta$ |
|---|---|---|---|---|---|---|---|
| $2N_2$ | T | 0.013 232° | 0.035 163° | 0.062 324° | 0.023 320° | 0.007 112° | 0.010 210° |
| $\mu_2$ | T | 0.020 220° | 0.052 156° | 0.062 308° | 0.022 324° | 0.006 22° | 0.004 247° |
| $N_2$ | T | 0.194 216° | 0.356 143° | 0.388 315° | 0.165 335° | 0.039 262° | 0.089 51° |
| | S | 0.098 167° | 0.274 158° | 0.543 320° | 0.189 307° | 0.045 95° | 0.019 68° |
| | Z | 0.164 248° | 0.259 164° | 0.343 319° | 0.130 349° | 0.034 228° | 0.072 262° |
| $M_2$ | T | 1.877 239° | 3.052 158° | 2.112 314° | 0.874 0° | 0.455 323° | 0.907 68° |
| | S | 1.241 201° | 2.139 150° | 3.056 312° | 0.824 328° | 0.264 301° | 0.824 97° |
| | Z | 1.039 261° | 1.737 165° | 1.735 323° | 0.517 15° | 0.339 295° | 0.662 81° |
| $L_2$ | T | 0.063 275° | 0.094 187° | 0.053 318° | 0.018 49° | 0.018 344° | 0.028 91° |
| $T_2$ | T | 0.064 298° | 0.096 205° | 0.067 341° | 0.014 58° | 0.023 9° | 0.030 126° |
| $S_2$ | T | 1.128 300° | 1.694 206° | 1.168 342° | 0.243 62° | 0.412 11° | 0.514 128° |
| | S | 1.085 275° | 1.545 189° | 1.866 338° | 0.282 27° | 0.402 329° | 0.792 130° |
| | Z | 0.439 306° | 0.890 202° | 0.737 350° | 0.128 46° | 0.284 6° | 0.302 120° |
| $K_2$ | T | 0.349 320° | 0.527 225° | 0.351 1° | 0.072 86° | 0.134 31° | 0.155 147° |
| | Z | 0.124 310° | 0.252 205° | 0.202 352° | 0.030 45° | 0.083 10° | 0.081 123° |
| $\eta_2$ | T | 0.022 356° | 0.036 257° | 0.021 27° | 0.003 162° | 0.011 74° | 0.008 188° |
| $2SM_2$ | T | 0.011 308° | 0.014 211° | 0.010 345° | 0.002 143° | 0.003 359° | 0.004 141° |

Same as Table 5.2.

agreement between T and Z in all phase values which are considerably closer to each other than the ones calculated by S. The very good agreement between T and Z demonstrates the importance of the model's resolution as compared with the coarser, poorer agreeing S.

Comparisons of the results for the $K_2$-tide with Z result in a similar picture. While the values agree well in the phases, the amplitudes are generally higher in T by approximately a factor of 2.

The less significant semi-diurnal astronomic partial tides, $2N_2$, $\mu_2$, $L_2$, $T_2$ and $\eta_2$, are lower in amplitude by one or two orders of magnitude than e.g. the $M_2$. Their dominant components are also $M_y^r$ and $M_z^r$. The semi-diurnal shallow-water tide $2SM_2$ is even a bit lower in amplitude, yet still reaches values of $1 \cdot 10^{23} \frac{kgm^2}{s}$ in all three components of relative AM. This is quite remarkable considering that compound tides are not directly forced by the lunisolar tidal potential but form purely due to non-linearities in shallow-waters.

### 5.1.4 High-Frequency Shallow-Water Tides

The angular momenta of selected high-frequency shallow-water tides are listed in Table 5.4. Note that the amplitudes are given in $10^{22} \frac{kgm^2}{s}$ as compared to $10^{25}$ in the tables for the short-period astronomical tides (Tables 5.2 and 5.3). In general, third- and fourth-diurnal tides differ by three orders of magnitude from $M_2$ and $S_2$, sixth-diurnal by four, and eighth-diurnals by five orders of magnitude.

Table 5.4: Relative ($M^r$) and Rotational ($M^\Theta$) Angular Momentum of Shallow-Water Tides

| tide | model | $M_x^r$ | | $M_y^r$ | | $M_z^r$ | | $M_x^\Theta$ | | $M_y^\Theta$ | | $M_z^\Theta$ |
|---|---|---|---|---|---|---|---|---|---|---|---|---|
| $MO_3$ | 1.017 | 87° | 1.312 | 356° | 1.618 | 281° | 0.432 | 266° | 0.842 | 192° | 0.075 | 26° |
| $SO_3$ | 0.858 | 193° | 2.000 | 138° | 0.994 | 347° | 0.406 | 12° | 0.604 | 296° | 0.042 | 349° |
| $MK_3$ | 0.718 | 201° | 0.114 | 113° | 0.361 | 326° | 0.497 | 329° | 0.565 | 264° | 0.353 | 328° |
| $MN_4$ | 0.764 | 320° | 1.137 | 231° | 1.225 | 66° | 0.249 | 44° | 0.167 | 182° | 0.388 | 148° |
| $M_4$ | 2.942 | 356° | 3.788 | 265° | 3.603 | 122° | 0.930 | 92° | 0.310 | 259° | 0.609 | 215° |
| $MS_4$ | 0.840 | 61° | 1.842 | 356° | 0.446 | 197° | 0.719 | 136° | 0.250 | 326° | 0.449 | 83° |
| $MK_4$ | 0.320 | 42° | 0.449 | 3° | 0.292 | 138° | 0.249 | 162° | 0.022 | 16° | 0.144 | 124° |
| $M_6$ | 0.289 | 135° | 0.899 | 315° | 0.505 | 240° | 0.102 | 246° | 0.506 | 206° | 0.049 | 264° |
| $2MS_6$ | 0.263 | 269° | 0.470 | 280° | 0.459 | 229° | 0.129 | 337° | 0.059 | 137° | 0.063 | 20° |
| $2MK_6$ | 0.102 | 283° | 0.128 | 314° | 0.108 | 257° | 0.029 | 343° | 0.025 | 104° | 0.025 | 61° |
| $M_8$ | 0.024 | 49° | 0.057 | 32° | 0.023 | 341° | 0.008 | 178° | 0.005 | 48° | 0.009 | 108° |
| $3MS_8$ | 0.077 | 99° | 0.065 | 87° | 0.036 | 131° | 0.007 | 264° | 0.002 | 260° | 0.014 | 149° |
| $3MK_8$ | 0.025 | 137° | 0.005 | 29° | 0.012 | 38° | 0.005 | 123° | 0.012 | 341° | 0.006 | 318° |

Same as Table 5.2, except that amplitudes ($A_i$) are in $10^{22}\,\frac{kgm^2}{s}$.

$M^r$ clearly dominates over $M^\Theta$ as variations of the sea surface elevation due to shallow-water tides are limited to restricted areas in shelf regions whereas their currents can be traced even in the open ocean with considerable values in flow transport (Section 4.3). The highest amplitudes are calculated for $M_y^r$ for most of the shallow-water tides listed, with the exception of the $MO_3$ which has its maximum in $M_z^r$ and the $MK_3$, $3MS_8$ and $MK_3$ with maxima in $M_x^r$. The most significant high-frequency shallow-water tide is the $M_4$-overtide with $A_y^r = 3.8 \cdot 10^{22}\,\frac{kgm^2}{s}$ and $A_z^r = 3.6 \cdot 10^{22}\,\frac{kgm^2}{s}$.

## 5.2 Instantaneous Angular Momentum Budgets

The balance of instantaneous angular momentum budgets (Section 2.3.2) is shown in Figure 5.3 for a period of ten days in June 2002. The torque due to relative motion and the Coriolis force, here summarised as the left-hand side's total $L_s$ (Equation 2.19), is mostly balanced by the pressure torque $L_{pr}$. For the axial component z this relationship is most pronounced with $L_s \cong -L_{pr}$ and the frictional torque $L_{fr}$ and the tidal torque $L_{tid}$ being negligibly small. In the equatorial components x and y, $L_{fr}$ remains very small and can thus be neglected whereas $L_{tid}$ is getting more significant, albeit still relatively small compared to $L_s$ and $L_{pr}$. The results are similar to the findings of Seiler (1991) where results for the $M_2$, $K_1$ and $Mf$ are shown in Figures 8-10 therein.

The highest values within the selected time-series of Figure 5.3 are found in the y-component. $L_s$ ranges between $-6$ - $4 \cdot 10^{21}\frac{kg{\cdot}m^2}{s}$ and is mostly balanced by $L_{pr}$ with $-4$ - $6 \cdot 10^{21}\frac{kg{\cdot}m^2}{s}$. $L_{tid}$ only reaches roughly $1 \cdot 10^{21}\frac{kg{\cdot}m^2}{s}$. The values for the x-component are lower by almost an order of magnitude, however, $L_{tid}$ has a stronger relative influence in x than in y or z.

The same combination of semi-diurnal and diurnal variations are seen as in Figure 5.1, resulting in the inequality of neighbouring peaks. Note that the positive-valued peaks of $L_{pr}$ are greater

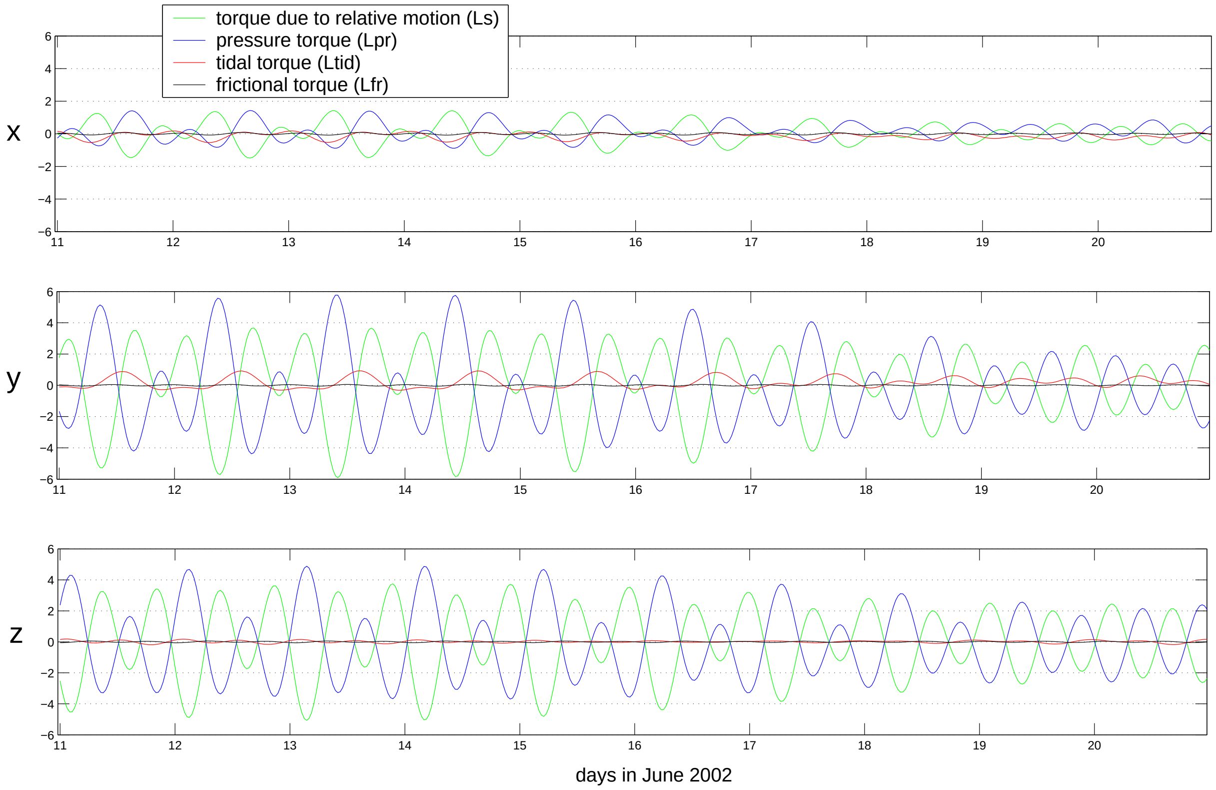

Figure 5.3: Instantaneous Angular Momentum Budgets in $10^{21}\frac{kg \cdot m^2}{s}$ calculated by TiME with 5' resolution (time-domain). The figure shows the torques $L_s$, $L_{pr}$, $L_{tid}$ and $L_{fr}$ for a time-span of ten days.

than the negative-valued ones and that the inequality of neighbouring peaks is more pronounced for the positive peaks. This is most conspicuous in the y-component. The same holds for $L_{tid}$ which has positive peaks roughly every 24 hours. $L_{tid}$ also reveals an off-set towards positive values, an effect of the long-period tides.

The greater significance of $L_{pr}$ compared with $L_{tid}$ reflects the character of the eigenoscillations. Seiler (1991) has shown that the resonantly oscillating system of the semi-diurnal and diurnal tides is characterised by $L_s \cong -L_{pr}$ whereas the long-period tides are characterised by $L_{tid} \cong L_{pr}$ reflecting a state near the equilibrium tide. The complete system described by Figure 5.3 is dominated by the oscillation behaviour of the partial tides involved and only a small amount can be directly attributed to the tide-generating forces.

## 5.3 Energy Dissipation and Tidal Friction

The frictional torque $L_{fr}$ is not significant in the instantaneous angular momentum budgets (Section 5.2). Frictional terms rather gain importance in the energy budgets, as they are the main cause for energy dissipation and drivers for tidal friction.

Tidal friction is directly related to a secular deceleration of the earth's rotation due to momentum transfer from the earth-moon-system to the lunar orbit (Kagan and Sündermann, 1996, and references therein). The dissipated tidal energy (-$\dot{E}$) is related to the tidal acceleration of the lunar mean longitude (-$\dot{n}_M$) by

$$-\dot{n}_M = \frac{3\cdot(M_M+M_E)}{M_M\cdot M_E\cdot c_M^2\cdot(\Omega-n_M)}\cdot(-\dot{E}) \tag{5.1}$$

where $M_M$ and $M_E$ are the masses of moon and earth, respectively, $c_M$ the mean distance between moon and earth, $\Omega$ the mean angular velocity of the earth and $n_M$ the mean angular velocity of the moon. According to Kepler's third law (Equation 5.2) an acceleration in the motion of the lunar orbit $\dot{n}_M$ will result in an increase of the the earth-moon distance $\dot{c}_M$.

$$-\dot{n}_M = \frac{3\cdot n_M}{2\cdot c_M}\cdot\dot{c}_M \tag{5.2}$$

A detailed discussion of the relationship between tidal friction and lunar acceleration can be found in Kagan and Sündermann (1996). The distance between the earth and the moon can be derived in different ways, ranging from interpretations of ancient reports on solar eclipses (e.g. Stephenson, 1978) to modern measurements by lunar laser ranging (e.g. Newhall et al., 1990). Kagan and Sündermann (1996) list results for -$\dot{n}_M$ and -$\dot{E}$ in Table I therein, and more recently Chapront et al. (2002) added new measurement results for $\dot{n}_M$ in Table 6 therein. These values range between 21 - 52 arcseconds per century$^2$ ($as/cy^2$) for -$\dot{n}_M$, or 2.6 and 5.2 Terawatts (TW) for -$\dot{E}$. Yet the most recent measurement values seem to agree on a significantly smaller range of about 24 - 26 $as/cy^2$ for $\dot{n}_M$ or a total dissipation rate of about 3 TW.

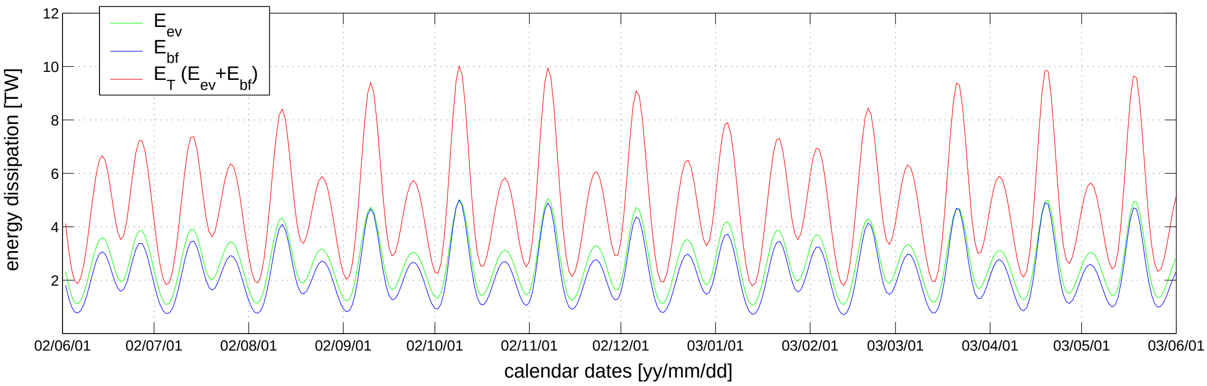

Figure 5.4: Energy dissipated due to eddy-viscosity and bottom friction in $10^{12} kgm^2/s^3$ (1 TW) calculated by TiME with 5' resolution (time-domain). Daily means are plotted for one calendar year (June 2002 - June 2003).

The energy dissipated by eddy-viscosity, ($\dot{E}_{ev}$), and by bottom friction, ($\dot{E}_{bf}$), within the modelling approach of TiME is shown in Figure 5.4 for a time-span of one year (June 2002 - June 2003) as daily averaged values. Note that by averaging over a day, there is always part of the most dominant partial tide $M_2$ missing, so the values should be treated with care. Averaging over cycles of $M_2$ would lead to a similar imbalance as all the other tidal constituents' periods would not be closed.

Instantaneous real-time values, however, give a measure of the total amount of dissipated energy and its variation within a year's time. Fortnightly, monthly and semi-annual variations are clearly visible, which can be attributed to both long-period tides and to the superimposition of daily and subdaily partial tides. Eddy-viscosity is only slightly stronger than bottom friction, with the two having about the same values (1 - 5 TW). Calculations of the yearly averages give $\dot{E}_{ev}$ = 2.6 TW, $\dot{E}_{bf}$ = 2.2 TW or a total of $\dot{E}_T$ = 4.8 TW.

Not all of the energy dissipated due to the lunisolar tides has an effect on the moon's angular velocity, though. As tidal friction is a phenomenon of the earth-moon-system only, only the dissipation of the lunar part can be considered in the relation of Equation 5.1. Simulations with $M_2$ partial tide forcing with TiME (5' resolution) produce $\dot{E}_{ev}= 2.0\ TW$ and $\dot{E}_{bf}= 1.6\ TW$ leading to a value of $\dot{E}_T= 3.6\ TW$. Assuming that the principal lunar tide $M_2$ contributes to about 88% of the total dissipation rate (Sündermann and Brosche, 1978), this leads to an estimate of total tidal friction of about $\dot{E}= 4.1\ TW$. This value lies within the range of measurements. Compared to the recent agreement on about 3 TW, however, it is higher by 30%.

Egbert and Ray (2000) estimate the dissipation of the $M_2$ with their data assimilation model to amount up to 2.4-2.5 TW. Taking the factor $0.88$ into account, this would lead to a value of 2.7-2.8 TW for total tidal frictional and is reasonably close to the measurements.

In order to better investigate the total energy dissipated by ocean tides contributing to tidal friction in the time-domain, a simulation over a full lunar node (about 18.6 years) forced by the lunar tidal potential only would be preferable, as all partial tides would be closed. The only restriction would be that the interactions between lunar and solar tides would not be taken into account.

## 5.4 Earth Rotation Parameters

The effects of the ocean tides on variations in the earth's rotation were calculated in both the time- and frequency-domains. The instantaneous values of relative and rotational angular momentum (see Fig. 5.1) were taken for the calculation of the $\chi$-functions (Equation 2.47). For the representation in the frequency-domain, the results of relative and rotational angular momentum given in Tables 5.1-5.4 were used for calculation of the earth rotation parameters. The time-series of $M_i^r$ and $M_i^\Theta$ (Fig. 5.1) were harmonically analysed directly in order to extract additional partial tides. In total, all partial tides derived from the second degree lunisolar tidal potential listed in Bartels (1957) have been analysed (Tables A.1 and A.2).

Results in the frequency-domain will be compared to measurements of the earth rotation parameters. Variations of semi-diurnal and diurnal tides are described by Sovers et al. (1993), Herring and Dong (1994) and Gipson (1996) from VLBI measurements and Rothacher et al. (1998) from GPS measurements. Results of the ocean tide models used for comparison in Section 5.1 will not be shown here (excepting the variations in UT1 due to the long-period tides).

The results of the variations in the length of day and in UT1 of Zahel et al. (2000) are listed in Table 3 therein. The OTAM calculated by Seiler (1991) were analysed by Gross (1993) and are listed in Tables 2 and 3 therein.

Results in the frequency-domain can be represented as amplitude- and phase-values or as cosine- and sine-values. In the following, the amplitude-phase notation will be used. In order to compare the model results with available measurements, some cosine-sine notated values had to be transformed. In oceanography, the tidal argument of any partial tide is normally given by the Doodson variables while geodetic studies usually refer to Woolard arguments. Depending on the notation, phase values may have to be corrected by values of 180° or ±90° before comparing model results with measurements. The specific names of individual partial tides may differ or in some cases are not given at all. See Appendix A.4 for conversions and transformations performed for this study.

The effects of ocean tides on the earth's rotation can be separated into variations of the rotational speed, quantified as either changes in the length of day or as variations in Universal Time (UT1) (Section 5.4.1), and variations in the orientation of the earth's rotational axis (polar motion) (Section 5.4.2).

## 5.4.1 Variations in the Length of Day and Universal Time

Variations in the length of day ($\Delta$LOD) are calculated to be up to one millisecond (1000 $\mu$sec) within the time-span shown in Figure 5.5. As $\Delta$LOD only depends on $\psi_3$ (Equation 2.43) which is defined by $M_z^r$ and $M_z^\Theta$, Figure 5.5 essentially redraws the time-series of $M_z$ in Figure 5.1 (bottom), except that the effect of $M_z^\Theta$ is considered to be about 3/4 weaker than $M_z^r$ (Equation 2.42). The time-series shows the same combination of semi-diurnal, diurnal and fortnightly variations as well as the off-set towards positive values due to the semi-annual and annual tides as seen in Figure 5.1.

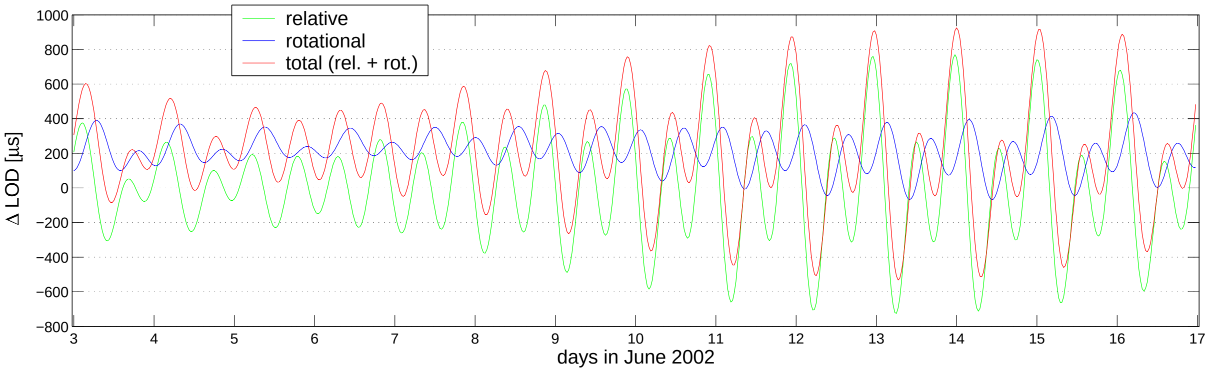

Figure 5.5: Variations in the length of day in $\mu$sec calculated by TiME with 5' resolution (time-domain) for one fortnight in June 2002.

The variations in UT1 in the frequency-domain for long-period tides, diurnal, semi-diurnal and some shallow-water tides are shown in Tables 5.5 - 5.8.

Table 5.5: Variations in UT1 caused by Long-Period Tides

| | $Sa$ | | $Ssa$ | | $Sta$ | | $MSm$ | | $Mm$ | | $MSf$ | |
|---|---|---|---|---|---|---|---|---|---|---|---|---|
| rel | 1.32 | 224° | 7.61 | 300° | 0.45 | 315° | 1.05 | 338° | 5.30 | 343° | 1.06 | 15° |
| Θ | 220.69 | 241° | 698.71 | 269° | 29.59 | 282° | 24.85 | 280° | 102.22 | 282° | 11.07 | 271° |
| tot | 221.96 | 241° | 705.20 | 269° | 29.96 | 282° | 25.42 | 282° | 104.82 | 284° | 10.9 | 276° |
| K | | | | | | | | | 115.00 | 280° | | |
| S/G | | | 676.58 | 272° | | | | | 108.01 | 284° | | |
| | $Mf$ | | $mf$ | | $MStm$ | | $Mtm$ | | $mtm$ | | $MSqm$ | |
| rel | 12.30 | 14° | 2.64 | 21° | 0.68 | 36° | 2.35 | 16° | 0.73 | 15° | 0.34 | 42° |
| Θ | 118.37 | 307° | 29.89 | 322° | 3.59 | 314° | 12.06 | 295° | 3.83 | 297° | 1.60 | 315° |
| tot | 123.60 | 312° | 31.30 | 326° | 3.73 | 324° | 12.63 | 306° | 4.04 | 307° | 1.65 | 326° |
| K | 114.90 | 295° | | | | | | | | | | |
| S/G | 92.85 | 292° | 38.44 | 292° | | | | | | | | |

Values shown are $A_u$ [$\mu$sec] and $\phi_u$ [°].
Variations calculated by TiME due to relative (rel), rotational (Θ) and total angular momentum (tot = rel + Θ).
Comparisons with Kantha et al. (1998) (K) and Seiler (1991) as calculated by Gross (1993) (S/G).

### *Long-Period Tides*

The effects of long-period tides are clearly dominated by the effect of $M^\Theta$ (marked as Θ). The influence of $M^r$ (rel) is about two orders of magnitude lower for partial tides with very low frequencies ($Sa$, $Ssa$ and $Sta$) and one order of magnitude lower for those with shorter periods ($Mf$ and $mf$). This reflects the interpretation that the longer the period, the closer the oscillation system of the partial tide is to the equilibrium tide (see Section 5.1 and Seiler (1991)).

The semi-annual and annual solar tides $Ssa$ and $Sa$ have the strongest effect on UT1 of the long-period tides with 705 and 222 microseconds ($\mu$sec) followed by the monthly and fortnightly lunar tides $Mm$ and $Mf$ with about 100 $\mu$sec.

Comparisons with results from Gross (1993) (S/G) show that the results of TiME for the long-period tides are in very good agreement with the partial tide model of Seiler (1991), excepting the fortnightly tide $Mf$. Comparisons with the data assimilation model of Kantha et al. (1998) (K) show a very good agreement of all three ocean tide models for the monthly tide $Mm$. The results of K for the $Mf$ perfectly agree with S/G in the phase value but produce higher amplitudes which agree better with the results of this study.

### *Diurnal Tides*

Results of $\Delta$UT1 of partial tides of the diurnal tidal band are compared with measurements by Sovers et al. (1993) (S), Herring and Dong (1994) (H), Gipson (1996) (G) and Rothacher et al. (1998) (R) in Table 5.6. All four measurement studies investigated at least the most significant diurnal partial tides ($Q_1$, $O_1$, $P_1$ and $K_1$).

The strongest diurnal variations in UT1 are caused by the $O_1$-tide with an amplitude of about 38 $\mu$sec. Measurements show relatively lower values of 21 - 24 $\mu$sec. Phase values of the model

Table 5.6: Variations in UT1 caused by Diurnal Tides

| | $2Q_1$ | $\sigma_1$ | $q_1$ | $Q_1$ | $\varrho_1$ | $o_1$ | $O_1$ | $\tau_1$ |
|---|---|---|---|---|---|---|---|---|
| rel | 0.62 338° | 0.77 338° | 0.76 326° | 5.76 347° | 1.07 353° | 4.08 18° | 26.90 11° | 0.23 16° |
| Θ | 0.37 343° | 0.48 336° | 0.50 345° | 3.23 8° | 0.58 18° | 2.02 53° | 12.75 48° | 0.24 37° |
| tot | 0.99 340° | 1.25 337° | 1.24 333° | 8.85 354° | 1.61 2° | 5.85 29° | 37.90 23° | 0.46 27° |
| S | | | | 6.64 37° | | | 21.40 39° | |
| H | | | | 5.30 36° | | | 23.63 47° | |
| G | 0.89 27° | | 0.98 24° | 5.90 26° | 1.25 29° | 4.28 37° | 22.54 37° | |
| R | 2.38 15° | 1.25 29° | 1.08 22° | 6.05 22° | 0.78 50° | 4.26 39° | 22.77 39° | |

| | $o_1'$ | $M_1$ | $\chi_1$ | $\pi_1$ | $P_1$ | $S_1$ | $K_1$ | $km_1$ |
|---|---|---|---|---|---|---|---|---|
| rel | 1.99 4° | 0.44 157° | 0.42 25° | 0.41 28° | 7.29 38° | 0.17 64° | 23.32 46° | 3.12 32° |
| Θ | 0.65 61° | 0.17 216° | 0.13 82° | 0.07 95° | 1.31 116° | 0.06 153° | 3.46 134° | 0.62 117° |
| tot | 2.40 17° | 0.55 172° | 0.50 37° | 0.45 36° | 7.67 47° | 0.18 83° | 23.66 54° | 3.23 43° |
| S | | | | | 7.16 27° | | 15.50 13° | |
| H | | 2.92 38° | | | 7.07 33° | 2.22 54° | 18.95 20° | |
| G | 0.71 82° | 1.00 53° | | 0.22 27° | 5.99 28° | 2.37 28° | 18.54 30° | 2.56 31° |
| R | 1.63 11° | 1.61 353° | | 2.72 126° | 6.80 26° | 2.94 305° | 20.35 26° | 2.77 26° |

| | $\psi_1$ | $\varphi_1$ | $\vartheta_1$ | $J_1$ | $SO_1$ | $OO_1$ | $oo_1$ | $\nu_1$ |
|---|---|---|---|---|---|---|---|---|
| rel | 0.19 35° | 0.33 37° | 0.24 52° | 1.22 53° | 0.22 33° | 0.99 75° | 0.23 136° | 0.14 93° |
| Θ | 0.02 116° | 0.06 108° | 0.02 270° | 0.12 276° | 0.06 69° | 0.34 6° | 0.11 70° | 0.06 73° |
| tot | 0.19 42° | 0.36 46° | 0.23 48° | 1.14 49° | 0.26 40° | 1.16 59° | 0.30 116° | 0.20 86° |
| S | | | | | | | | |
| H | 1.53 79° | 2.60 106° | | 2.20 3° | | 1.22 99° | | 1.58 252° |
| G | | | | 1.20 335° | | 1.04 73° | 0.63 72° | 0.41 14° |
| R | 2.42 330° | 0.28 225° | | 0.89 63° | | 1.43 78° | 0.92 77° | 1.08 304° |

Same as Table 5.5.
Comparisons with Sovers et al. (1993) (S), Herring and Dong (1994) (H), Gipson (1996)) (G), and Rothacher et al. (1998) (R).

results and measurements are in good agreement. The difference between the model results of TiME (T) and G is 14° and the measurements themselves differ by up to 10°.

The results of the $K_1$- and the $P_1$-tide are in even better agreement with measurements. For both partial tides, the rotational angular momentum is out of phase with relative angular momentum and much lower in amplitude. Thus the total AM stays almost at the values of the relative AM. For the $Q_1$-tide, relative and rotational AM are in phase so that the total adds up to an amplitude in ΔUT1 of 8.9 $\mu$sec which is again higher than the 5.3 - 6.6 $\mu$sec indicated by the measurements.

Two variational tides of the major diurnals $O_1$ and $K_1$, the $\underline{o_1}$ and $\underline{km_1}$, are found to have a significant effect on ΔUT1 of about 6 $\mu$sec and 3 $\mu$sec , respectively. The measurements reported in G and R give slighlty lower amplitudes. Phase values are in very good agreement.

In comparison to G, good agreement can also be found for $\varrho_1$, $\pi_1$ and $OO_1$ and general agreement in amplitudes but increasing differences in phases can be seen for $2Q_1$, $q_1$, $oo_1$ and $J_1$. Comparisons with R show similar agreement for these partial tides except for $\pi_1$ and $2Q_1$. T and R calculate an identical amplitude for $\sigma_1$ and differ by more than 50° in phase values. General agreement of T and R is found for $o_1'$ while G differs both in amplitude and phase.

Table 5.7: Variations in UT1 caused by Semi-Diurnal Tides

| | $3N_2$ | | $\varepsilon_2$ | | $2N_2$ | | $\mu_2$ | | $N_2$ | | $\nu_2$ | | $\gamma_2$ | | $\alpha_2$ | |
|---|---|---|---|---|---|---|---|---|---|---|---|---|---|---|---|---|
| rel | 0.16 | 219° | 0.32 | 223° | 0.88 | 234° | 0.88 | 218° | 5.42 | 225° | 0.98 | 225° | 0.05 | 211° | 0.08 | 227° |
| Θ | 0.06 | 67° | 0.11 | 78° | 0.11 | 120° | 0.04 | 157° | 0.94 | 321° | 0.20 | 322° | 0.02 | 307° | 0.02 | 342° |
| tot | 0.11 | 206° | 0.23 | 207° | 0.85 | 227° | 0.90 | 216° | 5.41 | 235° | 0.98 | 236° | 0.06 | 233° | 0.08 | 243° |
| S | | | | | | | | | 3.05 | 221° | | | | | | |
| H | | | | | | | | | 3.22 | 240° | | | | | | |
| G | | | | | 0.85 | 249° | 0.81 | 210° | 3.86 | 239° | | | | | | |
| R | | | | | 0.98 | 246° | 0.67 | 243° | 4.39 | 246° | 0.73 | 254° | | | | |

| | $m_2$ | | $M_2$ | | $\beta_2$ | | $\delta_2$ | | $\lambda_2$ | | $L_2$ | | $km_2$ | | $2T_2$ | |
|---|---|---|---|---|---|---|---|---|---|---|---|---|---|---|---|---|
| rel | 1.34 | 231° | 28.94 | 224° | 0.09 | 223° | 0.03 | 186° | 0.24 | 214° | 0.71 | 228° | 0.35 | 273° | 0.04 | 255° |
| Θ | 0.44 | 347° | 9.39 | 338° | 0.03 | 342° | 0.01 | 305° | 0.09 | 348° | 0.29 | 1° | 0.12 | 50° | 0.01 | 39° |
| tot | 1.21 | 250° | 26.48 | 243° | 0.08 | 244° | 0.02 | 215° | 0.19 | 234° | 0.56 | 250° | 0.27 | 291° | 0.03 | 270° |
| S | | | 18.17 | 235° | | | | | | | | | | | | |
| H | | | 17.92 | 233° | | | | | | | | | | | | |
| G | 0.58 | 59° | 18.28 | 237° | | | | | | | 0.14 | 135° | | | | |
| R | 0.67 | 63° | 17.29 | 247° | | | | | | | 0.45 | 27° | | | | |

| | $T_2$ | | $S_2$ | | $R_2$ | | $K_2$ | | $km'_2$ | | $\zeta_2$ | | $\eta_2$ | | $km''_2$ | |
|---|---|---|---|---|---|---|---|---|---|---|---|---|---|---|---|---|
| rel | 0.89 | 251° | 15.45 | 252° | 0.17 | 69° | 4.64 | 271° | 1.45 | 256° | 0.06 | 274° | 0.27 | 297° | 0.08 | 347° |
| Θ | 0.30 | 36° | 5.15 | 38° | 0.06 | 215° | 1.54 | 57° | 0.49 | 42° | 0.02 | 93° | 0.08 | 98° | 0.01 | 145° |
| tot | 0.67 | 266° | 11.60 | 267° | 0.13 | 84° | 3.46 | 285° | 1.09 | 271° | 0.04 | 274° | 0.20 | 305° | 0.06 | 352° |
| S | | | 5.22 | 266° | | | 2.75 | 251° | | | | | | | | |
| H | | | 8.60 | 269° | 1.00 | 217° | 3.79 | 282° | | | | | 0.32 | 252° | 0.36 | 56° |
| G | | | 7.84 | 264° | | | 2.55 | 281° | 0.71 | 278° | | | | | | |
| R | 0.63 | 252° | 7.72 | 266° | 0.94 | 148° | 3.11 | 236° | 0.94 | 238° | | | | | | |

Same as Table 5.6.

Big differences in amplitudes and phases are found for $o'_1$, $\psi_1$, $\varphi_1$, $M_1$ and $\nu_1$. The two latter ones were included in three measurement studies - H, G, and R - which diverge from each other by comparable amounts as the model T does. Obviously, the results become more tentative the less significant the extracted partial tides are.

Four additional diurnal partial tides were analysed which are not documented in the literature. The influences of $\tau_1$, $\chi_1$, $\vartheta_1$ and $SO_1$ on $\Delta$UT1 are relatively small, with amplitude values between 0.2 - 1.2 $\mu$sec.

The $S_1$ is both an astronomical tide (the elliptic tide of first order of $K_{1s}$) and a ”meteorological” tide (which is excited by tidal variations in the atmosphere). As no atmospheric data are considered within the model approach, no meteorological tides are captured by the model which most probably explains the discrepancy between model results and measurements.

### *Semi-Diurnal Tides*

TiME calculates relative angular momentum to be the dominant term for variations in UT1 of the semi-diurnal tidal band for all partial tides listed in Table 5.7. As the influences of relative and rotational angular momentum are out of phase for all partial tides, the total influence results in lower amplitude values than for relative AM alone.

Table 5.8: Variations in UT1 caused by Shallow-Water Tides

| | $2SM_2$ | $MQ_3$ | $MO_3$ | $SO_3$ | $MK_3$ | $SP_3$ | $SK_3$ | $K_3$ |
|---|---|---|---|---|---|---|---|---|
| rel | 132.2 255° | 7.5 144° | 15.0 191° | 9.0 257° | 3.3 236° | 0.5 145° | 5.2 268° | 1.4 247° |
| Θ | 42.1 51° | 0.3 60° | 0.5 296° | 0.3 258° | 2.4 240° | 0.1 34° | 1.1 339° | 1.2 6° |
| tot | 95.3 266° | 7.6 142° | 14.8 193° | 9.3 257° | 5.7 237° | 0.5 134° | 5.6 279° | 1.3 301° |
| | $3MS_4$ | $MN_4$ | $M_4$ | $SN_4$ | $3MN_4$ | $MS_4$ | $MK_4$ | $S_4$ |
| rel | 1.4 354° | 8.5 336° | 24.7 32° | 0.6 136° | 1.7 309° | 3.0 107° | 2.0 48° | 0.6 132° |
| Θ | 0.5 354° | 2.0 58° | 3.2 125° | 0.3 322° | 0.3 0° | 2.3 353° | 0.7 34° | 0.6 91° |
| tot | 1.9 354° | 9.0 349° | 24.7 39° | 0.2 127° | 1.8 316° | 2.9 62° | 2.7 44° | 1.2 112° |
| | $2MN_6$ | $M_6$ | $MSN_6$ | $MNK_6$ | $2MS_6$ | $2MK_6$ | $2SM_6$ | $MSK_6$ |
| rel | 0.81 113° | 2.31 150° | 0.56 90° | 0.64 86° | 2.07 139° | 0.49 166° | 0.54 187° | 0.38 222° |
| Θ | 0.06 53° | 0.20 174° | 0.06 217° | 0.03 215° | 0.21 290° | 0.08 331° | 0.02 302° | 0.04 85° |
| tot | 0.84 109° | 2.46 151° | 0.53 95° | 0.62 89° | 1.89 142° | 0.41 170° | 0.54 189° | 0.35 217° |
| | $3MN_8$ | $M_8$ | $2MSN_8$ | $2MNK_8$ | $3MS_8$ | $3MK_8$ | $2(MS)_8$ | $2MSK_8$ |
| rel | 0.11 173° | 0.08 251° | 0.05 331° | 0.06 95° | 0.12 40° | 0.04 308° | 0.11 118° | 0.09 143° |
| Θ | 0.03 306° | 0.02 18° | 0.03 24° | 0.06 137° | 0.04 58° | 0.02 228° | 0.04 149° | 0.10 257° |
| tot | 0.09 187° | 0.07 266° | 0.07 350° | 0.06 99° | 0.16 45° | 0.05 288° | 0.14 126° | 0.08 139° |

Same as Table 5.5, except that $A_u$ are shown in nsec.

The influence of the four major semi-diurnal partial tides ($N_2$, $M_2$, $S_2$ and $K_2$) on the variations in UT1 is in very good agreement with the four measurement studies. The amplitudes calculated by the model of $N_2$, $M_2$ and $S_2$ are generally higher than the ones derived from measurements. The strongest influence on semi-diurnal variations in UT1 is caused by the $M_2$ where measurements calculate an amplitude of about 17-18 $\mu$sec whereas the model calculates 26 $\mu$sec. In contrast, the amplitude of $K_2$ lies within the range of the measurements and is in excellent agreement with the values from Herring and Dong (1994). Phase values of all four major semi-diurnal tides show exceptionally good agreement.

Besides these dominant partial tides, few semi-diurnal constituents effect ΔUT1 with amplitudes greater than 1 $\mu$s. $2N_2$, $\mu_2$, $\nu_2$, $T_2$ and $km_2'$ are in very good to excellent agreement with the results of G and R. $m_2$, $L_2$ and $\eta_2$ are in the same order of magnitude as the measurements. Only $R_2$ and $km_2''$ strongly diverge between results of the model and H and R.

### *Shallow-Water Tides*

The influence of shallow-water tides on UT1 is several orders of magnitude less than the major astronomical tides described above and is given in nanoseconds (nsec) in Table 5.8. The strongest effect is caused by the semi-diurnal compound tide $2SM_2$ with about 95 nsec. Of the third-diurnal tides, the $MO_3$ has the strongest influence with 15 nsec and, out of the fourth-diurnals, the $M_4$-overtide with 25 nsec. They are followed by the $SO_3$ and $MN_4$ both resulting in variations in UT1 by about 9 nsec. For comparison, the weakest influence of the astronomic partial tides listed in Tables 5.5-5.7 is caused by the $\delta_2$ with 20 nsec (0.02 $\mu$sec). The most influential shallow-water tide for ΔUT1 out of the sixth-diurnals is $M_6$ with 2.5 nsec and out of the eighth-diurnals $3MS_8$ with about 0.2 nsec.

### 5.4.2 Polar Motion

The effect of the ocean tides on the orientation of the earth's axis depends on the equatorial components x and y of the rotational and relative angular momentum (see Figure 5.1) and is characterised by the excitation functions $\psi_1$ and $\psi_2$ (Equations 2.40 and 2.41).

In the time-domain, the effect of ocean tides on polar motion (PM) is preferentially described by the effective angular momentum functions $\chi$ (Equation 2.47). Figure 5.6 presents a time-span of six weeks in 2002 with three pronounced fortnightly cycles indicated by the change from red to blue. These fortnightly cycles are similar to the ones shown for the angular momentum (Figure 5.1).

The inequality of the neighbouring semi-diurnal peaks in the angular momenta results in two alternating main oscillations in polar motion, one reaching values of up to 6 $\mu$as in $\chi_y$ and the other one of up to 3 $\mu$as. On the negative axis, both oscillations result in about -4 $\mu$as. Figure 5.7 shows the same time-series in two dimensions as an outline of the excitation so that the two main oscillations are clearly distinguishable in a quasi elliptic form.

The ellipses vary in their dimensions, an effect of the fortnightly cycles described earlier. These ellipses are the result of the superimposition of a number of elliptic periodic motions, each one excited by a partial tide. The effect of any partial tide on polar motion can therefore be described by an ellipse which can be further divided into a prograde ($p$) and a retrograde ($r$) circular movement. Referring to the given frequency of a partial tide, these are then represented by amplitudes ($A_p$ and $A_r$) and phases ($\phi_p$ and $\phi_r$). The semi-major axis of the ellipse is defined by $A_p + A_r$, the semi-minor axis by $A_p - A_r$.

In the following, the modelled effects of the ocean tides on polar motion will be described in more detail in the frequency-domain and compared to measurements. The effect was calculated following Gross (1993) where the Chandler wobble and the free core nutation were taken into account. Amplitudes are given in fractions of an arcsecond (1° = 3600 as) with a variation in polar motion of one milliarcsecond (1 mas) corresponding to roughly 3 cm on the earth's surface.

*Long-Period Tides*

Angular momenta of the long-period tides are strongly dominated by the axial rotational AM $M_z^{\Theta}$ (Table 5.1) which produce the main variations in UT1 (Table 5.5), yet variations in the equatorial components are also significant enough to have a considerable effect on polar motion (Table 5.9). The most influential tides are the annual $Sa$ and the semi-annual $Ssa$. The former results in a maximum variation of up to 140 $\mu$as (prograde) and the latter 120 $\mu$as (retrograde). Both are dominated by the influence of rotational AM ($M^{\Theta}$).

$Ssa$ and $Sa$ are followed by the fortnightly tide $Mf$ with 100 $\mu$as in the amplitude of prograde polar motion and the monthly $Mm$ with 46 $\mu$as (also prograde). In contrast to $Sa$ and $Ssa$, they are dominated by relative AM ($M^r$).

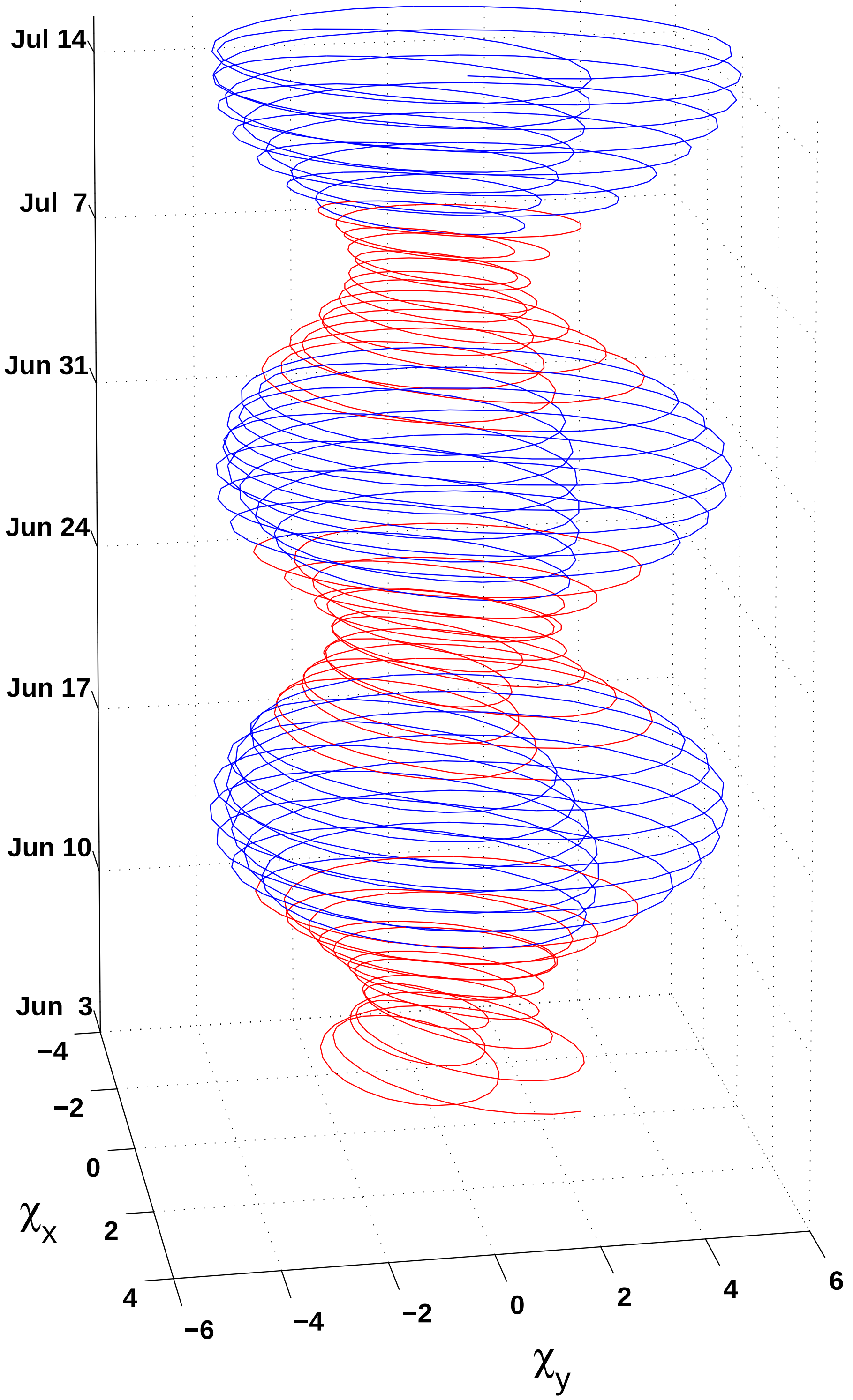

Figure 5.6: The effect of ocean tides on polar motion calculated from the $\chi$-functions in microarcseconds ($\mu$as) produced by TiME. The figure shows a time-span of six weeks in 2002 (indicated by the blue and red colours).

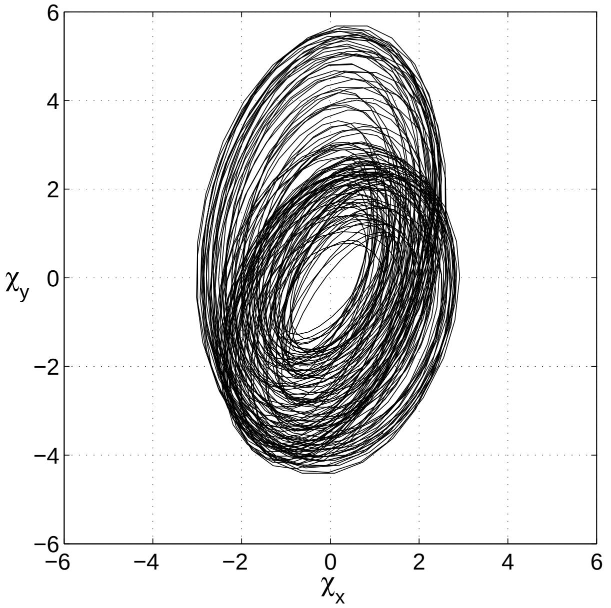

Figure 5.7: The effect of ocean tides on polar motion as in Figure 5.6, with the time-dimension collapsed into this 2-D representation.

Table 5.9: Effect of Long-Period Tides on Polar Motion

| | $Sa$ | | | | $Ssa$ | | | | $Sta$ | | | | $MSm$ | | | |
|---|---|---|---|---|---|---|---|---|---|---|---|---|---|---|---|---|
| rel | 35.09 | 306° | 5.55 | 279° | 68.27 | 292° | 44.48 | 314° | 2.97 | 310° | 3.37 | 316° | 9.20 | 264° | 7.09 | 340° |
| Θ | 174.98 | 145° | 12.59 | 280° | 108.72 | 115° | 77.23 | 342° | 5.48 | 67° | 5.69 | 349° | 3.51 | 339° | 5.68 | 40° |
| tot | 142.28 | 149° | 18.14 | 280° | 40.82 | 121° | 118.49 | 332° | 4.92 | 34° | 8.71 | 337° | 10.66 | 283° | 11.04 | 6° |
| | $Mm$ | | | | $MSf$ | | | | $Mf$ | | | | $mf$ | | | |
| rel | 42.54 | 262° | 32.89 | 345° | 10.38 | 278° | 6.65 | 350° | 87.48 | 214° | 61.61 | 35° | 23.52 | 196° | 13.94 | 42° |
| Θ | 17.02 | 350° | 24.34 | 43° | 10.41 | 351° | 7.31 | 344° | 25.36 | 281° | 58.01 | 110° | 6.86 | 240° | 15.83 | 119° |
| tot | 46.29 | 283° | 50.17 | 9° | 16.76 | 315° | 13.94 | 347° | 100.07 | 228° | 95.03 | 71° | 28.85 | 206° | 23.39 | 83° |
| | $MStm$ | | | | $Mtm$ | | | | $mtm$ | | | | $MSqm$ | | | |
| rel | 4.12 | 198° | 2.47 | 45° | 13.74 | 209° | 7.36 | 35° | 3.68 | 185° | 1.01 | 342° | 1.61 | 180° | 1.13 | 33° |
| Θ | 1.38 | 268° | 1.88 | 132° | 5.11 | 235° | 10.85 | 143° | 2.59 | 121° | 4.34 | 211° | 0.46 | 183° | 0.40 | 279° |
| tot | 4.77 | 213° | 3.16 | 81° | 18.47 | 216° | 11.07 | 103° | 5.34 | 159° | 3.76 | 223° | 2.07 | 180° | 1.03 | 12° |

Results calculated by TiME of effects due to relative (rel), rotational (Θ) and total angular momentum (tot = rel + Θ). Values shown are $A_p$ [$\mu$as], $\phi_p$ [°], $A_r$ [$\mu$as] and $\phi_r$ [°] for the respective partial tide.

Gross (1993) (Table 2 therein) has investigated the tidal effect on polar motion based on the angular momenta given in Seiler (1991). The new predictions from this study for $mf$, $Mm$ and $Ssa$ are in very good agreement with this earlier work. Results for the amplitudes of the $Mf$-tide, however, are doubled in the new approach while still agreeing in the phase values.

There is a large difference in the calculated effect on polar motion by measurements and different models, especially for the fortnightly tides (Gross et al., 1997). The higher amplitudes of $Mf$ calculated by TiME for prograde polar motion agree well with the results from Desai (1996, cited in Gross et al. (1997)) who used an ocean model utilising estimates from altimetric sea surface height measurements. The higher amplitudes of retrograde polar motion agree well with the results from measurements (Gross et al., 1997). Note that Gross et al. (1997) have recalculated the results for the $\chi$-functions and that the aforementioned comparisons are only tentative. This good agreement with these measurements and the Desai-Model suggest that TiME represents the $Mf$ better than Seiler (1991).

*Diurnal Tides*

The effect of the partial tides of the diurnal tidal band on polar motion are shown in Table 5.10 as results derived from relative and rotational angular momenta (Section 5.1) calculated by the model. For comparison, results of measurements are added (Sovers et al. (1993, S), Herring and Dong (1994, H), Gipson (1996, G) and Rothacher et al. (1998, R)).

The free core nutation has a nearly diurnal retrograde frequency and is in resonance with the diurnal partial tides. In the calculations, the denominator $\sigma_{fcn} - \sigma_{pt}$ of Equation 2.45 moves towards zero and leads to increasing values in the amplitudes of retrograde polar motion $A_r$. This resonance phenomenon creates difficulties in the determination of quasi-diurnal retrograde polar motion from measurements so this term is normally omitted in measurement studies.

The results of three of the main diurnal partial tides ($Q_1$, $O_1$ and $P_1$) are in extraordinary good agreement with the measurements from H for $A_p$ and $\phi_p$. The $K_1$-tide, which has the strongest effect on the prograde quasi-diurnal polar motion with an amplitude of about 180 $\mu$as is in good agreement with G.

The variational tides $o_1$ and $km_1$ again prove to be relatively influential on the earth rotation parameters (see Section 5.4.1) with prograde amplitudes of 29 and 26 $\mu$as. The values are in excellent agreement with G and R.

Among the smaller partial tides, good agreements are found for $\sigma_1$, $\varrho_1$, $M_1$, $J_1$ and $OO_1$ and general agreement is achieved for $q_1$ and $oo_1$. T is in excellent agreement with R for $2Q_1$ while G differs substantially. Weak agreement is observed for $\psi_1$, $\varphi_1$ and $\nu_1$ with H, G and R. Similar to the results of UT1, the measurement studies also differ substantially in their respective estimates of the effect of these weaker partial tides.

The model calculates an amplitude for prograde polar motion of about 1.5 $\mu$as for the $S_1$. This refers to the contribution of the astronomical $S_1$. The measured values of 23-54 $\mu$as likely represent the meteorological $S_1$ which is not included in the model.

The values in amplitudes of retrograde polar motion are highest for partial tides with frequencies near the free core nutation (e.g. $P_1$, $K_1$, $km_1$). An amplitude of 11.5 mas (milliarcseconds) calculated for the $K_1$ would result in polar motion of roughly 35 cm on the earth's surface.

# Table 5.10: Effect of Diurnal Tides on Polar Motion

| | $2Q_1$ | | | | $\sigma_1$ | | | | $q_1$ | | | | $Q_1$ | | | |
|---|---|---|---|---|---|---|---|---|---|---|---|---|---|---|---|---|
| rel | 3.19 | 6° | 5.12 | 316° | 3.79 | 3° | 5.90 | 316° | 2.68 | 311° | 2.33 | 298° | 14.21 | 298° | 24.44 | 301° |
| Θ | 5.88 | 135° | 5.09 | 309° | 6.98 | 135° | 5.62 | 308° | 7.21 | 131° | 1.98 | 288° | 50.53 | 107° | 16.26 | 305° |
| tot | 4.57 | 103° | 10.19 | 312° | 5.31 | 102° | 11.49 | 312° | 4.53 | 131° | 4.29 | 293° | 36.66 | 103° | 40.68 | 303° |
| S | | | | | | | | | | | | | 49.00 | 54° | | |
| H | | | | | | | | | | | | | 34.79 | 72° | | |
| G | 14.87 | 42° | | | 7.28 | 16° | | | 6.08 | 81° | | | 30.81 | 77° | | |
| R | 4.12 | 104° | | | 6.08 | 81° | | | 6.32 | 72° | | | 34.79 | 72° | | |
| | $\varrho_1$ | | | | $o_1$ | | | | $O_1$ | | | | $\tau_1$ | | | |
| rel | 2.47 | 278° | 4.52 | 298° | 10.16 | 178° | 24.76 | 276° | 60.14 | 179° | 167.86 | 273° | 0.48 | 111° | 3.09 | 263° |
| Θ | 9.11 | 98° | 2.46 | 308° | 32.31 | 61° | 8.06 | 133° | 205.25 | 68° | 54.48 | 126° | 2.31 | 67° | 1.10 | 122° |
| tot | 6.65 | 98° | 6.96 | 302° | 29.09 | 79° | 18.91 | 261° | 192.12 | 85° | 125.59 | 259° | 2.67 | 74° | 2.34 | 245° |
| S | | | | | | | | | 132.00 | 54° | | | | | | |
| H | | | | | | | | | 199.01 | 63° | | | | | | |
| G | 7.21 | 56° | | | 27.51 | 71° | | | 145.15 | 72° | | | | | | |
| R | | | | | 25.96 | 74° | | | 137.09 | 74° | | | | | | |
| | $o'_1$ | | | | $M_1$ | | | | $\chi_1$ | | | | $\pi_1$ | | | |
| rel | 6.20 | 142° | 17.96 | 259° | 1.48 | 339° | 4.19 | 46° | 1.31 | 119° | 3.83 | 279° | 1.34 | 107° | 4.21 | 277° |
| Θ | 12.61 | 70° | 34.22 | 111° | 2.94 | 278° | 73.70 | 259° | 2.62 | 51° | 9.44 | 131° | 2.45 | 49° | 42.26 | 131° |
| tot | 15.69 | 92° | 21.29 | 137° | 3.88 | 297° | 70.20 | 261° | 3.33 | 72° | 6.50 | 149° | 3.34 | 69° | 38.84 | 134° |
| S | | | | | | | | | | | | | | | | |
| H | | | | | 5.00 | 127° | | | | | | | | | | |
| G | | | | | 2.83 | 315° | | | | | | | | | | |
| R | 10.44 | 17° | | | 11.31 | 315° | | | | | | | 14.87 | 110° | | |
| | $P_1$ | | | | $S_1$ | | | | $K_1$ | | | | $km_1$ | | | |
| rel | 23.12 | 99° | 71.86 | 285° | 0.55 | 64° | 1.62 | 312° | 74.11 | 91° | 191.18 | 291° | 10.60 | 98° | 24.88 | 277° |
| Θ | 43.01 | 38° | 1034.38 | 141° | 1.08 | 7° | 42.11 | 169° | 134.53 | 30° | 11649.29 | 148° | 18.59 | 46° | 1710.77 | 133° |
| tot | 57.95 | 58° | 976.87 | 144° | 1.46 | 26° | 40.83 | 171° | 182.58 | 51° | 11496.21 | 149° | 26.42 | 64° | 1690.57 | 133° |
| S | 69.00 | 92° | | | | | | | 134.00 | 51° | | | | | | |
| H | 60.22 | 54° | | | 23.41 | 110° | | | 152.20 | 61° | | | | | | |
| G | 47.54 | 68° | | | 28.86 | 104° | | | 173.54 | 63° | | | 23.71 | 62° | | |
| R | 77.62 | 68° | | | 53.76 | 137° | | | 168.43 | 58° | | | 22.47 | 58° | | |
| | $\psi_1$ | | | | $\varphi_1$ | | | | $\vartheta_1$ | | | | $J_1$ | | | |
| rel | 0.59 | 105° | 4.53 | 281° | 1.18 | 103° | 4.82 | 283° | 0.84 | 94° | 3.38 | 286° | 3.94 | 95° | 17.30 | 289° |
| Θ | 1.06 | 43° | 523.89 | 318° | 1.95 | 32° | 132.19 | 319° | 1.48 | 26° | 12.81 | 327° | 7.71 | 23° | 56.33 | 330° |
| tot | 1.43 | 64° | 527.62 | 317° | 2.59 | 58° | 136.11 | 318° | 1.95 | 49° | 15.51 | 319° | 9.65 | 46° | 70.30 | 320° |
| S | | | | | | | | | | | | | | | | |
| H | 10.63 | 229° | | | 16.76 | 107° | | | | | | | 21.93 | 246° | | |
| G | 3.61 | 34° | | | 10.05 | 174° | | | | | | | 7.21 | 34° | | |
| R | 45.88 | 344° | | | 6.08 | 81° | | | | | | | 7.07 | 352° | | |
| | $SO_1$ | | | | $OO_1$ | | | | $oo_1$ | | | | $\nu_1$ | | | |
| rel | 1.19 | 117° | 4.10 | 292° | 5.98 | 86° | 21.14 | 307° | 1.45 | 30° | 4.69 | 7° | 1.33 | 44° | 3.57 | 340° |
| Θ | 1.99 | 356° | 6.72 | 321° | 7.81 | 346° | 29.93 | 342° | 1.88 | 281° | 6.32 | 45° | 0.99 | 294° | 3.45 | 3° |
| tot | 1.71 | 33° | 10.52 | 310° | 8.94 | 27° | 48.70 | 328° | 1.97 | 325° | 10.42 | 29° | 1.36 | 1° | 6.88 | 351° |
| S | | | | | | | | | | | | | | | | |
| H | | | | | 22.02 | 39° | | | | | | | 18.44 | 347° | | |
| G | | | | | 10.82 | 34° | | | 4.47 | 153° | | | 3.61 | 56° | | |
| R | | | | | 14.14 | 45° | | | 8.49 | 45° | | | 7.07 | 315° | | |

Same as Table 5.9.
Comparisons with Sovers et al. (1993) (S), Herring and Dong (1994) (H), Gipson (1996)) (G), and Rothacher et al. (1998) (R).

The excellent agreement of TiME's results with the measurement data clearly shows how useful this modelling approach is, as it can provide this data for many more partial tides than the measurement campaigns can capture.

### *Semi-Diurnal Tides*

As the frequencies of the partial tides of the semi-diurnal tidal band do not resonate with the free core nutation, measurements are available for both prograde and retrograde polar motion (Table 5.11).

In general, TiME produces higher amplitudes for the main semi-diurnal tides than the ones given by the measurements. The strongest effect on diurnal PM is caused by the $M_2$ with about 117 $\mu$as (prograde) and 443 $\mu$as (retrograde) while measurements result in 22-67 $\mu$as and 256-265 $\mu$as. Phase values are in better agreement, though they also differ by 20° in retrograde polar motion.

The $S_2$-tide differs in amplitudes by a factor of 1.3 to 3 compared to measurements and shows excellent agreement in phase values. The $N_2$ is in excellent agreement with measurements.

The amplitude of retrograde polar motion due to the $K_2$-tide is in good agreement with S; H and G, however, give substantially lower values. $K_2$ phases of retrograde PM are in very good agreement. The modelled prograde PM of the $K_2$ is calculated to be 13 $\mu$as while measurements range higher with 23 - 39 $\mu$as. Model results are out of phase with measurements.

Out of the less significant semi-diurnals, only $\mu_2$ and $\nu_2$ are in relatively good agreement with G and R. Note, however, that several semi-diurnal partial tides in H, G and R give cosine- or sine-values of 0 for prograde and retrograde polar motion, and were therefore not taken into account in Table 5.11. Comparisons with results of H, G and R of the $R_2$-tide show that measurements can differ considerably from each other.

### *Shallow-Water Tides*

The effect of the non-linear shallow-water tides on polar motion is again weaker by orders of magnitude than the major astronomical tides (Table 5.12 lists amplitudes in nanoarcseconds). The most influential compound tide $2SM_2$, however, is in the same range as the less significant semi-diurnal partial tides (Table 5.11) with amplitudes of about 0.3 $\mu$as (prograde) and 2.1 $\mu$as (retrograde). In general, the influence due to relative angular momentum is stronger than the one due to rotational angular momentum. In most cases, the two effects are out of phase.

All third- and fourth-diurnal tides listed have considerably higher values for retrograde amplitudes than prograde ones. The strongest are $SO_3$, $MO_3$, $MK_3$ and $SK_3$ with $A_r$ of 70-136 nas and $M_4$, $MS_4$, $MN_4$ and $MK_4$ with $A_r$ of 37-356 nas. The influence on polar motion is even less significant for the sixth-and eighth-diurnals. In most cases, $A_r$ is again higher than $A_p$, yet not as pronounced as in the third- and fourth-diurnals. The most significant ones are $M_6$, $2SM_6$, $2MN_6$ and $2SM_6$ with $A_r$ of 10-29 nas and $3MS_8$, $2(MS)_8$, $3MN_8$ and $M_8$ with $A_r$ of 2-3 nas.

# Table 5.11: Effect of Semi-Diurnal Tides on Polar Motion

| | $3N_2$ | | | | $\epsilon_2$ | | | | $2N_2$ | | | | $\mu_2$ | | | |
|---|---|---|---|---|---|---|---|---|---|---|---|---|---|---|---|---|
| rel | 0.36 | 106° | 0.76 | 257° | 1.06 | 108° | 1.76 | 245° | 2.43 | 94° | 5.05 | 247° | 3.75 | 100° | 7.49 | 239° |
| Θ | 0.28 | 228° | 0.18 | 306° | 0.69 | 229° | 0.56 | 329° | 2.06 | 207° | 1.81 | 303° | 2.09 | 222° | 1.53 | 334° |
| tot | 0.32 | 154° | 0.88 | 266° | 0.92 | 148° | 1.91 | 262° | 2.49 | 144° | 6.24 | 261° | 3.16 | 133° | 7.51 | 251° |
| S | | | | | | | | | | | | | | | | |
| H | | | | | | | | | | | | | | | | |
| G | | | | | | | | | | | | | 5.00 | 127° | | |
| R | | | | | | | | | 3.61 | 236° | 3.16 | 198° | | | | |

| | $N_2$ | | | | $\nu_2$ | | | | $\gamma_2$ | | | | $\alpha_2$ | | | |
|---|---|---|---|---|---|---|---|---|---|---|---|---|---|---|---|---|
| rel | 18.89 | 109° | 57.06 | 227° | 3.61 | 113° | 11.37 | 226° | 0.59 | 143° | 2.28 | 207° | 0.39 | 136° | 1.63 | 213° |
| Θ | 9.84 | 211° | 17.58 | 338° | 1.73 | 210° | 3.46 | 341° | 0.14 | 268° | 0.64 | 358° | 0.09 | 247° | 0.47 | 349° |
| tot | 19.43 | 138° | 53.40 | 245° | 3.81 | 140° | 10.36 | 243° | 0.52 | 156° | 1.75 | 218° | 0.37 | 148° | 1.33 | 227° |
| S | 23.00 | 125° | 37.00 | 267° | | | | | | | | | | | | |
| H | 16.97 | 135° | 48.05 | 282° | | | | | | | | | | | | |
| G | 13.89 | 120° | 42.01 | 269° | 6.32 | 198° | 17.49 | 301° | | | | | | | | |
| R | 15.65 | 153° | 44.10 | 266° | 4.47 | 117° | 3.16 | 198° | | | | | | | | |

| | $m_2$ | | | | $M_2$ | | | | $\beta_2$ | | | | $\delta_2$ | | | |
|---|---|---|---|---|---|---|---|---|---|---|---|---|---|---|---|---|
| rel | 5.13 | 76° | 18.60 | 266° | 127.55 | 98° | 505.95 | 244° | 0.37 | 90° | 1.45 | 249° | 0.29 | 351° | 0.65 | 5° |
| Θ | 2.42 | 192° | 2.93 | 40° | 53.04 | 212° | 101.76 | 17° | 0.19 | 203° | 0.23 | 12° | 0.25 | 170° | 0.31 | 214° |
| tot | 4.61 | 104° | 16.69 | 273° | 116.75 | 122° | 443.10 | 254° | 0.35 | 119° | 1.34 | 257° | 0.05 | 358° | 0.41 | 343° |
| S | | | | | 22.00 | 57° | 265.00 | 273° | | | | | | | | |
| H | | | | | 58.01 | 91° | 265.19 | 272° | | | | | | | | |
| G | 2.24 | 297° | | | 67.12 | 115° | 261.23 | 272° | | | | | | | | |
| R | 2.83 | 315° | | | 65.12 | 133° | 256.00 | 270° | | | | | | | | |

| | $\lambda_2$ | | | | $L_2$ | | | | $km_2$ | | | | $2T_2$ | | | |
|---|---|---|---|---|---|---|---|---|---|---|---|---|---|---|---|---|
| rel | 1.22 | 99° | 5.89 | 257° | 3.15 | 80° | 15.78 | 276° | 1.21 | 41° | 5.78 | 317° | 0.15 | 73° | 0.74 | 301° |
| Θ | 0.24 | 253° | 1.14 | 49° | 0.56 | 211° | 2.89 | 61° | 0.40 | 170° | 0.97 | 93° | 0.05 | 226° | 0.13 | 85° |
| tot | 1.01 | 105° | 4.91 | 263° | 2.81 | 89° | 13.51 | 283° | 1.00 | 59° | 5.12 | 325° | 0.10 | 87° | 0.64 | 308° |
| S | | | | | | | | | | | | | | | | |
| H | | | | | | | | | | | 6.40 | 39° | | | | |
| G | | | | | | | | | | | | | | | | |
| R | | | | | 5.00 | 307° | 3.61 | 124° | | | | | | | | |

| | $T_2$ | | | | $S_2$ | | | | $R_2$ | | | | $K_2$ | | | |
|---|---|---|---|---|---|---|---|---|---|---|---|---|---|---|---|---|
| rel | 3.24 | 72° | 15.94 | 296° | 57.17 | 72° | 280.53 | 298° | 0.64 | 256° | 3.11 | 115° | 18.08 | 54° | 86.81 | 317° |
| Θ | 1.10 | 223° | 2.84 | 83° | 19.72 | 225° | 50.36 | 87° | 0.22 | 50° | 0.57 | 265° | 6.29 | 210° | 16.00 | 109° |
| tot | 2.34 | 85° | 13.63 | 303° | 40.61 | 84° | 238.81 | 304° | 0.45 | 269° | 2.64 | 121° | 12.62 | 66° | 73.10 | 323° |
| S | | | | | 21.00 | 73° | 174.00 | 303° | | | | | 32.00 | 160° | 62.00 | 286° |
| H | | | | | 12.17 | 99° | 119.54 | 304° | 13.89 | 330° | 10.30 | 299° | 39.32 | 173° | 30.53 | 328° |
| G | 7.07 | 135° | | | | | 129.54 | 303° | | | 3.61 | 56° | | | 20.62 | 337° |
| R | 18.38 | 45° | 12.37 | 194° | 31.06 | 86° | 130.51 | 301° | 16.12 | 120° | 13.00 | 67° | 23.35 | 133° | 43.01 | 269° |

| | $km'_2$ | | | | $\zeta_2$ | | | | $\eta_2$ | | | | $km''_2$ | | | |
|---|---|---|---|---|---|---|---|---|---|---|---|---|---|---|---|---|
| rel | 5.84 | 69° | 28.11 | 302° | 0.31 | 55° | 1.47 | 295° | 1.39 | 27° | 5.58 | 350° | 0.46 | 318° | 1.84 | 56° |
| Θ | 1.97 | 225° | 5.17 | 95° | 0.07 | 233° | 0.22 | 110° | 0.51 | 196° | 1.11 | 163° | 0.21 | 155° | 0.34 | 253° |
| tot | 4.11 | 80° | 23.65 | 308° | 0.24 | 55° | 1.25 | 296° | 0.90 | 33° | 4.48 | 352° | 0.26 | 305° | 1.52 | 52° |
| S | | | | | | | | | | | | | | | | |
| H | | | | | | | | | 7.81 | 230° | 2.24 | 117° | | | 8.06 | 330° |
| G | | | 6.71 | 333° | | | | | | | | | | | | |
| R | 7.07 | 135° | | | | | | | | | | | | | | |

Same as Table 5.10.

Table 5.12: Effect of Shallow-Water Tides on Polar Motion

| | $2SM_2$ | | | | $MQ_3$ | | | | $MO_3$ | | | | $SO_3$ | | | |
|---|---|---|---|---|---|---|---|---|---|---|---|---|---|---|---|---|
| rel | 331.6 | 85° | 2397.6 | 304° | 14.9 | 21° | 57.9 | 16° | 20.6 | 277° | 162.0 | 87° | 94.3 | 111° | 18.7 | 218° |
| Θ | 150.0 | 319° | 314.4 | 112° | 9.8 | 142° | 26.5 | 235° | 22.8 | 62° | 69.1 | 276° | 11.5 | 309° | 53.6 | 20° |
| tot | 273.3 | 58° | 2091.6 | 306° | 13.0 | 62° | 41.0 | 351° | 13.2 | 359° | 94.6 | 80° | 83.4 | 109° | 136.4 | 224° |
| | $MK_3$ | | | | $SP_3$ | | | | $SK_3$ | | | | $K_3$ | | | |
| rel | 28.5 | 155° | 125.7 | 202° | 15.7 | 229° | 36.3 | 94° | 52.2 | 39° | 97.1 | 276° | 16.5 | 25° | 50.1 | 297° |
| Θ | 11.8 | 305° | 55.3 | 342° | 4.7 | 40° | 9.3 | 264° | 11.3 | 207° | 31.0 | 72° | 6.8 | 195° | 12.4 | 77° |
| tot | 19.2 | 172° | 90.2 | 225° | 11.2 | 233° | 27.2 | 98° | 41.2 | 42° | 70.2 | 287° | 9.8 | 33° | 41.3 | 308° |
| | $3MS_4$ | | | | $MN_4$ | | | | $M_4$ | | | | $SN_4$ | | | |
| rel | 24.3 | 318° | 34.9 | 302° | 19.4 | 36° | 98.8 | 321° | 43.8 | 11° | 346.6 | 355° | 15.3 | 262° | 19.1 | 43° |
| Θ | 5.1 | 122° | 3.2 | 48° | 14.7 | 117° | 7.5 | 2° | 39.8 | 71° | 36.3 | 73° | 4.8 | 62° | 7.2 | 74° |
| tot | 19.5 | 323° | 34.2 | 307° | 26.2 | 70° | 104.5 | 323° | 72.4 | 39° | 356.1 | 1° | 10.9 | 271° | 25.6 | 52° |
| | $3MN_4$ | | | | $MS_4$ | | | | $MK_4$ | | | | $S_4$ | | | |
| rel | 10.4 | 258° | 10.7 | 259° | 57.9 | 255° | 132.8 | 78° | 17.8 | 222° | 35.2 | 72° | 12.3 | 148° | 8.8 | 220° |
| Θ | 3.4 | 69° | 1.6 | 73° | 26.9 | 24° | 31.4 | 118° | 8.9 | 13° | 10.2 | 158° | 4.4 | 271° | 6.1 | 188° |
| tot | 7.0 | 263° | 9.1 | 260° | 46.2 | 282° | 158.2 | 86° | 10.9 | 246° | 37.2 | 88° | 10.5 | 168° | 14.4 | 207° |
| | $2MN_6$ | | | | $M_6$ | | | | $MSN_6$ | | | | $MNK_6$ | | | |
| rel | 14.2 | 9° | 17.7 | 7° | 32.4 | 333° | 32.4 | 63° | 5.5 | 355° | 3.8 | 308° | 5.1 | 13° | 5.4 | 334° |
| Θ | 0.9 | 44° | 1.2 | 199° | 2.0 | 323° | 3.7 | 262° | 1.1 | 220° | 1.2 | 286° | 0.4 | 174° | 0.4 | 230° |
| tot | 15.0 | 11° | 16.5 | 6° | 34.4 | 332° | 29.0 | 60° | 4.8 | 345° | 4.9 | 303° | 4.7 | 14° | 5.3 | 330° |
| | $2MS_6$ | | | | $2MK_6$ | | | | $2SM_6$ | | | | $MSK_6$ | | | |
| rel | 19.7 | 324° | 16.8 | 338° | 6.8 | 290° | 3.9 | 354° | 6.2 | 299° | 8.5 | 28° | 4.4 | 275° | 4.8 | 49° |
| Θ | 4.0 | 182° | 3.2 | 310° | 1.3 | 182° | 0.4 | 280° | 1.6 | 134° | 1.6 | 339° | 1.1 | 105° | 1.0 | 352° |
| tot | 16.7 | 315° | 19.6 | 334° | 6.5 | 279° | 4.0 | 349° | 4.6 | 294° | 9.6 | 21° | 3.3 | 272° | 5.4 | 40° |
| | $3MN_8$ | | | | $M_8$ | | | | $2MSN_8$ | | | | $2MNK_8$ | | | |
| rel | 0.7 | 234° | 1.3 | 72° | 1.4 | 213° | 1.7 | 103° | 1.0 | 149° | 1.3 | 104° | 0.1 | 53° | 0.6 | 74° |
| Θ | 0.1 | 347° | 0.2 | 102° | 0.1 | 325° | 0.3 | 163° | 0.1 | 358° | 0.1 | 197° | 0.0 | 119° | 0.2 | 47° |
| tot | 0.7 | 239° | 1.5 | 76° | 1.4 | 217° | 1.9 | 110° | 0.9 | 146° | 1.3 | 110° | 0.2 | 60° | 0.8 | 67° |
| | $3MS_8$ | | | | $3MK_8$ | | | | $2(MS)_8$ | | | | $2MSK_8$ | | | |
| rel | 2.3 | 126° | 2.8 | 133° | 0.5 | 39° | 0.8 | 133° | 1.8 | 40° | 1.8 | 200° | 0.9 | 22° | 1.1 | 212° |
| Θ | 0.1 | 293° | 0.2 | 280° | 0.2 | 313° | 0.3 | 86° | 0.1 | 260° | 0.2 | 149° | 0.1 | 179° | 0.2 | 152° |
| tot | 2.2 | 127° | 2.7 | 135° | 0.6 | 17° | 1.0 | 120° | 1.7 | 38° | 2.0 | 196° | 0.8 | 25° | 1.2 | 205° |

Same as Table 5.10, except that amplitudes are given in nas.

Shallow-water tides are a unique feature of the new model TiME. So far, they have not been included in any measurement study of the earth rotation parameters. They will be above the detection limit of VLBI and GPS measurements in the near future. Recently, geodetic measurements have found variations with periods of 3 to 8 hours in both GPS and VLBI measurements in the order of magnitude of microseconds (Nastula et al., 2004). It has been debated whether these variations have a real physical origin or whether they are artefacts of the methodology. Results of this study can rule out that the high-frequency non-linearities within the ocean tide system could be responsible for these variations.

### 5.4.3 Correlation with Measurements

In the following, the results of this study for the semi-diurnal and diurnal tides have been compared with the measurement studies that include a large number of partial tides (Tables 5.6, 5.7, 5.10 and 5.11). These are the results of VLBI-measurements from Herring and Dong (1994) and Gipson (1996) as well as the results of GPS-measurements from Rothacher et al. (1998). RMS-values and correlation coefficients ($r_{xy}$) have been calculated for the results of $\Delta$UT1 (Table 5.13) and polar motion (Table 5.14). The three measurement studies have also been compared with each other.

Following the description in Section 2.5, amplitude and phase values have been treated as complex-valued numbers and prograde and retrograde polar motion as two independent data. Some less significant partial tides are only described by one or two measurement studies. Yet these tides are also of particular interest for this study, which aims at a complete description of the oscillation system. For every cross-comparison, all partial tides described by the respective data sets have been considered, leading to varying numbers $n$.

The comparisons of the results of $\Delta$UT1 in Table 5.13 show an excellent agreement of all four studies with correlation coefficients of $\geq 0.90$. Comparisons of the measurement studies with each other give RMS-values of 1.5 - 2.5 $\mu$sec while the comparisons of the results of this study with measurements give 4.4 - 6.4 $\mu$sec. Comparisons of the results for polar motion (Table 5.14) reveal a similar picture with correlation coefficients of $\geq 0.92$. The effect of the ocean tides

Table 5.13: Correlation of Results for $\Delta$UT1

|  | $H$ |  |  | $G$ |  |  | $R$ |  |  | $T$ |  |  |
|---|---|---|---|---|---|---|---|---|---|---|---|---|
|  | $n$ | $r_{xy}$ | $rms$ | $n$ | $r_{xy}$ | $rms$ | $n$ | $r_{xy}$ | $rms$ | $n$ | $r_{xy}$ | $rms$ |
| $H$ |  |  |  | 13 | 0.98 | 1.88 | 16 | 0.97 | 2.46 | 17 | 0.90 | 6.43 |
| $G$ | 13 | 0.98 | 1.88 |  |  |  | 26 | 0.98 | 1.45 | 25 | 0.95 | 4.61 |
| $R$ | 16 | 0.97 | 2.46 | 26 | 0.98 | 1.45 |  |  |  | 31 | 0.93 | 4.39 |
| $T$ | 17 | 0.90 | 6.43 | 25 | 0.95 | 4.61 | 31 | 0.93 | 4.39 |  |  |  |

Comparisons of TiME (this study) (T), Herring and Dong (1994) (H), Gipson (1996) (G), and Rothacher et al. (1998) (R).
RMS-values are given in $\mu$sec.

Table 5.14: Correlation of Results for Polar Motion

| | $H$ | | | $G$ | | | $R$ | | | $T$ | | |
|---|---|---|---|---|---|---|---|---|---|---|---|---|
| | $n$ | $r_{xy}$ | $rms$ | $n$ | $r_{xy}$ | $rms$ | $n$ | $r_{xy}$ | $rms$ | $n$ | $r_{xy}$ | $rms$ |
| $H$ | | | | 18 | 0.98 | 20.47 | 21 | 0.95 | 28.58 | 24 | 0.92 | 57.30 |
| $G$ | 18 | 0.98 | 20.47 | | | | 28 | 0.97 | 17.02 | 30 | 0.96 | 47.99 |
| $R$ | 21 | 0.95 | 28.58 | 28 | 0.97 | 17.02 | | | | 38 | 0.95 | 43.88 |
| $T$ | 24 | 0.92 | 57.30 | 30 | 0.96 | 47.99 | 38 | 0.95 | 43.88 | | | |

Comparisons of TiME (this study) (T), Herring and Dong (1994) (H), Gipson (1996) (G), and Rothacher et al. (1998) (R).
RMS-values are given in $\mu$as.

on polar motion calculated by TiME differs from the measurement studies with RMS-values of 44 - 58 $\mu$as. The measurement studies compared with each other give values of 17 - 29 $\mu$as. TiME produces the smallest RMS-values in comparison with Rothacher et al. (1998) for both $\Delta$UT1 and polar motion and the highest correlation coefficients in comparison with Gipson (1996).

In general, the results show that the effect of the complete oscillation system of ocean tides on the earth's rotation has been well-captured by the novel modelling approach.

# Chapter 6

# Conclusions and Outlook

The objective of this study was to develop an unconstrained ocean model in order to investigate the complete effect of ocean tides on the earth's rotation. The key aspect was the transition from a traditional partial tide approach to a real-time approach. To this end, a new astronomical module calculating the exact position of the moon and earth has been implemented into a barotropic ocean tide model. This module operates independently, i.e. the module calculates the respective orbits from fundamental angles and determines the complete lunisolar tidal potential of second degree for every model time-step.

No satellite or other data of the sea surface elevations have been assimilated. In this way, the model utilises only the current physical understanding of the orbits of the moon and earth and the ocean's response on the gravitational forces. This leaves the ocean topography as the only dependent data input. The spatial resolution has been chosen to be as high as computationally feasible. Chapter 2 of this study describes the basic equations of the modules making up the Tidal Model forced by Ephemerides (TiME) and the analytical methods applied for the study.

## 6.1 Conclusions

The improvements implemented in the original 1° ocean model in order to ensure the feasibility for the simulations on the high resolution of 5' globally are described in Chapter 3. This required an alteration of the numerical semi-implicit scheme. A pronounced dependency of the energy within the modelled system on the time-step has been abolished. Along with the newly implemented algorithm, the iteration-scheme has been reworked in order to ensure fast convergence.

A two-step poleward zonal resolution change has been implemented because convergence used to be slowest towards the North Pole and because the smallest actual mesh size of the modelling grid constraints the largest possible modelling time-step. The solution was tested on an artificial aqua planet with uniform water depth. No structural disturbance of the oscillation pattern and no reflections at the latitudes of resolution change were observed.

The model has been tuned with the parameter $A_H$, which determines the prescription of turbulent effects within a model grid box, by comparison with a standard data set of pelagic measurements. The model has been evaluated for results of five partial tides calculated with the traditional partial tide forcing and with partial tides extracted from simulations with the novel, full-forcing approach. The simulations tend to overestimate the oscillation system, a common and expected feature of most unconstrained ocean tide models. The predicted oscillation system is in very good agreement with measurements, with correlation coefficients of $> 0.88$ for all partial tides investigated.

Chapter 4 describes examples of the oscillation system produced by TiME. One conspicuous result of the resolution change is the shift of the $M_2$ amphidromic point south of Australia (one of the improvements of data assimilation models) with high resolution and using the GEBCO bathymetry. This effect is not produced by TiME when utilising the ETOPO bathymetry and does not seem to be governed by the local topography, but rather by the general oscillation system. The experiments reveal the important role of bottom topography in the model simulations.

Results from partial tide forcings were compared with results of partial tides extracted via harmonic analysis. The most significant differences in both amplitudes and phases are found at the ocean margins, particularly in extended shelf areas where amplitudes are highest. Regional examples of selected partial tides show that utilising the complete lunisolar forcing reduces the amplitudes of certain partial tides by up to 50%.

These differences can be attributed to non-linear interactions between partial tides, leading to the formation of shallow-water tides. With the novel approach used in TiME global charts of numerically predicted shallow-water tides were produced for the first time. These tides can be captured because: 1) all partial tides are included simultaneously, 2) the model is formulated with non-linear shallow-water equations, and 3) shelf areas are well represented due to the high resolution.

Shallow-water tides (SWT) can reach amplitudes of up to 20 cm locally. The spatial distribution of maxima in the sea surface elevations of the SWT can be associated with the areas where the biggest differences (between the forcing approaches) in the astronomical partial tides are found. The spatial distribution of flow transport reveals that the SWT, after their formation in shallow waters, propagate into the open ocean and should therefore be regarded as a global phenomenon. Transports can reach values of around $1\ m^2/s$ in the open ocean.

Global results for rotational and relative angular momentum have been compared with a coarser resolving partial tide model and a data assimilation model in Chapter 5. In general, the high-resolving real-time model agrees better with the data assimilation model then the partial tide model does. This agreement is best for the phase values. Amplitude values, however, are still significantly overestimated (with a factor of up to 2) for several partial tides, including the dominant semi-diurnals $M_2$ and $S_2$.

Rotational angular momentum (AM) dominates over relative AM for long-period tides. With decreasing periods relative AM gains importance. This also holds for the angular momenta of the high-frequency shallow-water tides. This confirms the interpretation of the significance of their flow transport in the open ocean (described in Chapter 4).

Comparisons of the torques of different processes show that the system is clearly dominated by resonantly excited oscillations: the torques due to relative motion is essentially balanced by the pressure torque and only a small portion is directly attributed to the gravitational tidal forces. The frictional torque is negligible within instantaneous angular momentum budgets, yet frictional terms are significant in energy budgets. The energy dissipated due to eddy-viscosity and bottom friction is the main driver of tidal friction which results in a secular acceleration of the mean lunar angular velocity.

The total amount of energy dissipated by the entire oscillation system of ocean tides is calculated by TiME to be 4.8 TW. Estimates of the energy dissipated by the $M_2$-tide calculated by TiME with the old partial tide approach gives 3.6 TW. The contribution of the ocean tides on tidal friction is estimated to be $\dot{E}$ = 4.1 TW, which lies within the range of published measurement results. Most recent measurements, however, agree on a much lower value of about 3 TW, which is related to a secular lunar acceleration of about 25 $as/cy^2$.

As well as this long-term effect of tides on the earth's rotation, the ocean tide oscillation systems also causes rapid variations in the earth rotation parameters (ERP). They can be determined by the changes in rotational and relative angular momentum described earlier. Variations in Universal Time (UT1) and polar motion (PM) due to ocean tides have been investigated in relation to the celestial ephemeris pole (CEP) and compared to other studies including VLBI and GPS measurements and results from data assimilation models.

Results are generally in very good agreement for the dominating partial tides from long-term periods to semi-diurnals. Agreement decreases with the decreasing significance of the respective partial tide, which is also true for comparisons of measurement results with each other. The general tendency of the unconstrained model to overestimate the oscillation system is also reflected in the amplitudes of $\Delta$UT1 and in the effect on PM.

Comparisons with measurements of the ERP show significant improvements in TiME as compared to the coarse-resolving partial tide model. The real-time approach offers the opportunity for a large number of constituents to be studied without extra effort so that most partial tides described in the literature have been included in this study. Some less significant partial tides, which had not been included in any modelling study so far, are in excellent agreement with results from both VLBI and GPS measurements with correlation coefficients of 0.90 - 0.96.

A selection of non-linear shallow-water tides were included in the investigations of the earth rotation parameters. Variations in both UT1 and PM are about three orders of magnitude lower than the major astronomical partial tides. Their effects should be above the detection limit of modern measuring methods within the near future as their values are only a bit lower than the less significant semi-diurnal and diurnal partial tides which are already included in measurement campaigns.

## 6.2 Outlook

As the accuracy of geodetic measurements is being improved and more and more data are acquired through satellite altimetry, there is a growing interest in smaller scale ocean tides. For the earth rotation parameters, this means that a larger number of constituents can be detected and hopefully in the near future this will involve the non-linear shallow-water tides. The model study offers a foundation for these new measurements to be compared with.

Satellite altimetry is currently moving part of its focus towards coastal and shelf areas. Data are usually more sparse in the vicinity of land than for the open ocean because they are more often disturbed by clouds. Cross-comparisons of TiME's results with satellite and tide gauge data for the Patagonian Shelf and the North Sea had been initiated but could not be conducted within the time-frame of this study and are a future application of this work. Especially, the theoretical predictions of shallow-water tides are of particular interest (e.g. Andersen, 1999).

The results of angular momentum and the tidal effect on the earth's rotation were only investigated on a global scale in this study. As the spatial resolution of TiME is considerably higher than most other global tidal models, a more detailed analysis to study the respective influence of selected regions may reveal further insight into the dynamics. The contribution of certain shelf sea areas to tidal friction is one interesting example.

This study has used the lunisolar tidal potential of second degree as a forcing of the ocean tide model. Knowing the position of the moon and sun, it would be possible and straightforward to also include the tidal potential of third degree. This would include additional partial tides, e.g. the $M_3$ which is of similar importance as the weaker short-period tides of this study, and were already included in measurement campaigns (Haas and Wünsch, 2006).

One of the processes not described in the current set-up of TiME is the conversion of tides into internal tides which might add to vertical mixing (Egbert and Ray, 2000). There are approaches to parameterise that effect for barotropic models (Jayne and St. Laurent, 2001). For the present study, it seemed too early to test this new approach, which is reportedly quite sensitive to the model set-up. The parameterisation was also developed for a much coarser modelling grid and only takes 5' resolution into account for an estimate of the roughness of the bottom topography. However, it will be worth following the on-going research as e.g. Egbert et al. (2004) have recently produced promising results with this parameterisation. As internal tides form due to baroclinic processes, which are at the moment still not fully described, it would be preferential to formulate them within a baroclinic ocean model.

In the presented study, the earth rotation parameters, i.e. changes in the length of day and polar motion, were calculated as decoupled effects. Also, the main variations in polar motion, i.e. free core nutation and Chandler wobble, were taken into account in the calculation, albeit without allowing for feedbacks of these free oscillations with the forced oscillations due to the ocean tides. These assumptions are a valid approximation with sufficient accuracy for the purpose of this study. However, studying the effect of the complete tidal dynamics described by TiME in combination with a non-linear gyro-model for the earth's rotation like DyMEG (Seitz, 2004) may provide further insight into the dynamics.

One final application is using TiME's description of the oscillation system given in this study as boundary data for other ocean models. Global charts of 33 partial tides are available in four different resolutions (5’, 10’, 15’ and 20’) for sea surface elevations and tidal currents as amplitude and phase values. The instantaneous velocity and elevation fields are available for the time-span from June 2002 until June 2003 every 1/2 hour.

In conclusion, this novel approach to describe the ocean tides offers a range of opportunities for studies of the ocean tide dynamics and their complete effect on the earth’s rotation.

# Appendix A

## A.1 System of Equations (Finite Differences)

Applying the semi-implicit numerical scheme of Backhaus (1985) in TiME required restructuring of the system of equations from the original scheme used in Seiler (1989) who applied the semi-implicit scheme of Backhaus (1983). In the following, the general system (Section A.1.1), the solution for the resolution change (Section A.1.2) and the polar cap (Section A.1.3) will be described.

### A.1.1 General System

Equation 2.9 formulated in finite differences reads:

$$U_{ij}^{n+1} = H_{ij}^{x} \cdot F_{ij}^{x} \left[ \alpha \cdot u_{ij}^{n} + \beta \cdot \underline{v}_{ij}^{n} + \Delta t X_{ij}^{n} - P_{ij}^{x} \right] \tag{A.1}$$

$$V_{ij}^{n+1} = H_{ij}^{y} \cdot F_{ij}^{y} \left[ \alpha \cdot v_{ij}^{n} - \beta \cdot \underline{u}_{ij}^{n} + \Delta t Y_{ij}^{n} - P_{ij}^{y} \right] \tag{A.2}$$

where $i$ is the index for the longitudinal direction (from W to E) and $j$ for the latitudinal one (S to N); $\underline{v}_{ij}^{n}$ and $\underline{u}_{ij}^{n}$ are the averaged zonal velocity at the $u$-point and the meridional velocity at the $v$-point, respectively, and $F$ is the bottom friction function.

$$F = \frac{H}{H + r \cdot \Delta t \sqrt{u^2 + v^2}} \tag{A.3}$$

The pressure gradient $P$ is formulated as:

$$P_{ij}^{x} = \frac{g'}{fa} \left[ \frac{\beta \left( \zeta_{(i+1)j}^{(1/2)} - \zeta_{ij}^{(1/2)} \right)}{\Delta\lambda \cos_u \phi_j} + \frac{\gamma \left( \zeta_{i(j+1)}^{(1/2)} + \zeta_{(i+1)(j+1)}^{(1/2)} - \zeta_{i(j-1)}^{(1/2)} - \zeta_{(i+1)(j-1)}^{(1/2)} \right)}{4\Delta\phi} \right] \tag{A.4}$$

$$P_{ij}^{y} = \frac{g'}{fa} \left[ \frac{\beta \left( \zeta_{ij}^{(1/2)} - \zeta_{i(j-1)}^{(1/2)} \right)}{\Delta\phi} - \frac{\gamma \left( \zeta_{(i+1)j}^{(1/2)} + \zeta_{(i+1)(j-1)}^{(1/2)} - \zeta_{(i-1)j}^{(1/2)} - \zeta_{(i-1)(j-1)}^{(1/2)} \right)}{4\Delta\lambda \cos_v \phi_j} \right] \tag{A.5}$$

with $\zeta^{(1/2)} = 0.5(\zeta^{n} + \zeta^{n+1})$ representing the elevation at the intermediate time-step. The equation of continuity reads:

$$\zeta_{ij}^{n+1} = \zeta_{ij}^{n} - \frac{\Delta t}{a\cos_u \phi_j}\left[\frac{U_{ij}^{(1/2)} - U_{(i-1)j}^{(1/2)}}{\Delta\lambda} + \frac{V_{i(j+1)}^{(1/2)}\cos_v \phi_{(j+1)} - V_{ij}^{(1/2)}\cos_v \phi_j}{\Delta\phi}\right]. \tag{A.6}$$

Inserting Equations A.1 and A.2 into Equation A.6 leads to the iteration problem of $\Delta\zeta = \zeta^{n+1} - \zeta^{n}$:

$$\begin{aligned}\Delta\zeta_{ij} = \frac{1}{1+c_5}\cdot\big[&c_1\Delta\zeta_{(i-1)(j+1)} + c_2\Delta\zeta_{i(j+1)} + c_3\Delta\zeta_{(i+1)(j+1)} + c_4\Delta\zeta_{(i-1)j} +\\ &c_6\Delta\zeta_{(i+1)j} + c_7\Delta\zeta_{(i-1)(j-1)} + c_8\Delta\zeta_{i(j-1)} + c_9\Delta\zeta_{(i+1)(j-1)} + B + C\big]\end{aligned} \tag{A.7}$$

with the coefficients $c_i$

$$\begin{aligned}
c_1 &= -b^x_{(i-1)j} - b^y_{i(j+1)}\\
c_2 &= -b^x_{(i-1)j} + b^x_{ij} - a^x_{i(j+1)}\\
c_3 &= b^y_{i(j+1)} + b^x_{ij}\\
c_4 &= b^y_{ij} + a^x_{(i-1)j} - b^y_{i(j+1)}\\
c_5 &= a^x_{ij} + a^x_{(i-1)j} + a^y_{ij} + a^y_{i(j+1)}\\
c_6 &= a^x_{ij} + b^y_{i(j+1)} - b^y_{ij}\\
c_7 &= b^y_{ij} + b^x_{(i-1)j}\\
c_8 &= a^y_{ij} - b^x_{ij} + b^x_{(i-1)j}\\
c_9 &= -b^x_{ij} - b^y_{ij}
\end{aligned}$$

defined by

$$\begin{aligned}
h^x_{ij} &= \frac{g'\Delta t H^x_{ij} F^x_{ij}}{4fa\Delta\lambda\cos_u \phi_j}\\
a^x_{ij} &= h^x_{ij}\frac{\beta}{a\Delta\lambda\cos_u \phi_j}\\
b^x_{ij} &= h^x_{ij}\frac{\gamma}{4a\Delta\phi}\\
h^y_{ij} &= \frac{g'\Delta t H^y_{ij} F^y_{ij}}{4fa\Delta\phi}\\
a^y_{ij} &= h^y_{ij}\frac{\beta\cos_v \phi_j}{a\Delta\phi\cos_u \phi_j}\\
b^y_{ij} &= -h^y_{ij}\frac{\gamma}{4a\lambda\cos_u \phi_j}
\end{aligned}$$

and the terms $B$ and $C$ representing the explicit pressure gradient and the perturbation term:

$$B = 2\left[c_1\zeta^n_{(i-1)(j+1)} + c_2\zeta^n_{i(j+1)} + c_3\zeta^n_{(i+1)(j+1)} + c_4\zeta^n_{(i-1)j} + c_5\zeta^n_{ij} + c_6\zeta^n_{(i+1)j} + c_7\zeta^n_{(i-1)(j-1)} + c_8\zeta^n_{i(j-1)} + c_9\zeta^n_{(i+1)(j-1)}\right] \tag{A.8}$$

$$C = \frac{\Delta t}{2a\cos_u\phi_j}\left[\frac{\widehat{U}_{(i-1)j} - \widehat{U}_{ij}}{\Delta\lambda} + \frac{\widehat{V}_{ij}\cos_v\phi_j - \widehat{V}_{i(j+1)}\cos_v\phi_{(j+1)}}{\Delta\phi}\right] \tag{A.9}$$

with

$$\begin{aligned}
\widehat{U}_{ij} &= H^x_{ij}\left[u^n_{ij} + F^x_{ij}\left(\alpha u^n_{ij} + \beta\underline{v}^n_{ij} + \Delta t X^n_{ij}\right)\right]\\
\widehat{V}_{ij} &= H^y_{ij}\left[v^n_{ij} + F^y_{ij}\left(\alpha v^n_{ij} - \beta\underline{u}^n_{ij} + \Delta t Y^n_{ij}\right)\right].
\end{aligned}$$

For the regions with lower zonal resolution the system is essentially the same (only replacing $\Delta\lambda$ by $2\Delta\lambda$ or $4\Delta\lambda$).

### A.1.2 Zonal Resolution Change

The resolution changes at the latitudes $b$ and $B = b + 1$. For the longitudinal indices, only every second $\zeta$-point in $b$ has a direct meridional neighbour in $B$. In the following, the index $i$ is an uneven integer defined as $i = 2I - 1$. The pressure gradient terms within the equations of motion (A.1 and A.2) for the bordering latitudes read:

$$\begin{aligned}
P^x_{ib} &= \frac{g'}{fa}\left[\frac{\beta\left(\zeta^{(1/2)}_{(i+1)b} - \zeta^{(1/2)}_{ib}\right)}{\Delta\lambda\cos_u\phi_b} + \frac{\gamma\left(1.5\zeta^{(1/2)}_{IB} + 0.5\zeta^{(1/2)}_{(I+1)B} - \zeta^{(1/2)}_{i(b-1)} - \zeta^{(1/2)}_{(i+1)(b-1)}\right)}{4\Delta\phi}\right]\\
P^x_{(i+1)b} &= \frac{g'}{fa}\left[\frac{\beta\left(\zeta^{(1/2)}_{(i+2)b} - \zeta^{(1/2)}_{(i+1)b}\right)}{\Delta\lambda\cos_u\phi_b} + \frac{\gamma\left(0.5\zeta^{(1/2)}_{IB} + 1.5\zeta^{(1/2)}_{(I+1)B} - \zeta^{(1/2)}_{(i+1)(b-1)} - \zeta^{(1/2)}_{(i+2)(b-1)}\right)}{4\Delta\phi}\right]\\
P^x_{IB} &= \frac{g'}{fa}\left[\frac{\beta\left(\zeta^{(1/2)}_{(I+1)B} - \zeta^{(1/2)}_{IB}\right)}{2\Delta\lambda\cos_u\phi_b} + \frac{\gamma\left(\zeta^{(1/2)}_{IB+1} + \zeta^{(1/2)}_{(I+1)(B+1)} - 2\zeta^{(1/2)}_{(i+1)(b)}\right)}{4\Delta\phi}\right]\\
P^y_{IB} &= \frac{g'}{fa}\left[\frac{\beta\left(\zeta^{(1/2)}_{IB} - \zeta^{(1/2)}_{ib}\right)}{\Delta\phi} - \frac{\gamma\left(\zeta^{(1/2)}_{(I+1)B} + 2\zeta^{(1/2)}_{(i+1)b} - \zeta^{(1/2)}_{(I-1)B} - 2\zeta^{(1/2)}_{(i-1)b}\right)}{8\Delta\lambda\cos_v\phi_B}\right]
\end{aligned}$$

while $P^y_{ib}$ is formulated analogue to $P^y_{ij}$. The equations of continuity are:

$$\begin{aligned}
\zeta^{n+1}_{ib} &= \zeta^n_{ib} - \frac{\Delta t}{a\cos_u\phi_b}\left[\frac{U^{(1/2)}_{ib} - U^{(1/2)}_{(i-1)b}}{\Delta\lambda} + \frac{V^{(1/2)}_{IB}\cos_v\phi_B - V^{(1/2)}_{ib}\cos_v\phi_b}{\Delta\phi}\right]\\
\zeta^{n+1}_{(i+1)b} &= \zeta^n_{(i+1)b} - \frac{\Delta t}{a\cos_u\phi_b}\left[\frac{U^{(1/2)}_{(i+1)b} - U^{(1/2)}_{ib}}{\Delta\lambda} + \frac{0.5(V^{(1/2)}_{IB} + V^{(1/2)}_{(I+1)B})\cos_v\phi_B - V^{(1/2)}_{(i+1)b}\cos_v\phi_b}{\Delta\phi}\right]
\end{aligned}$$

while $\zeta_{IB}^{n+1}$ follows $\zeta_{IJ}^{n+1}$. This leads to a slightly altered formulation of the iteration problem. For uneven integers $i$ in latitude $b$ it is formulated as:

$$\begin{aligned}\Delta\zeta_{ib} = \frac{1}{1+c_5} \cdot \big[ & c_1 \Delta\zeta_{(I-1)B} + c_2 \Delta\zeta_{IB} + c_3 \Delta\zeta_{(I+1)B} + c_4 \Delta\zeta_{(i-1)b} + \\ & c_6 \Delta\zeta_{(i+1)b} + c_7 \Delta\zeta_{(i-1)(b-1)} + c_8 \Delta\zeta_{i(b-1)} + c_9 \Delta\zeta_{(i+1)(b-1)} + B + C \big]\end{aligned} \tag{A.10}$$

with

$$\begin{aligned}
c_1 &= -0.5 b^x_{(i-1)b} - b^y_{IB} \\
c_2 &= -1.5 b^x_{(i-1)b} + 1.5 b^x_{ib} - a^x_{IB} \\
c_3 &= b^y_{IB} + 0.5 b^x_{ib} \\
c_4 &= b^y_{ib} + a^x_{(i-1)b} - b^y_{IB} \\
c_5 &= a^x_{ib} + a^x_{(i-1)b} + a^y_{ib} + a^y_{IB} \\
c_6 &= a^x_{ib} + b^y_{IB} - b^y_{ib} \\
c_7 &= b^y_{ib} + b^x_{(i-1)b} \\
c_8 &= a^y_{ib} - b^x_{ib} + b^x_{(i-1)b} \\
c_9 &= -b^x_{ib} - b^y_{ib}
\end{aligned}$$

$$C = \frac{\Delta t}{2a \cos_u \phi_b} \left[ \frac{\widehat{U}_{(i-1)b} - \widehat{U}_{ib}}{\Delta\lambda} + \frac{\widehat{V}_{ib} \cos_v \phi_j - \widehat{V}_{IB} \cos_v \phi_{(j+1)}}{\Delta\phi} \right].$$

For even integers $i+1$ at latitude $b$, 12 coefficients are needed and the iteration problem is formulated as:

$$\begin{aligned}\Delta\zeta_{(i+1)b} = \frac{1}{1+c_5} \cdot \big[ & c_1 \Delta\zeta_{IB} + c_2 \Delta\zeta_{(I+1)B} + c_3 \Delta\zeta_{(I+2)B} + c_4 \Delta\zeta_{ib} + \\ & c_6 \Delta\zeta_{(i+2)b} + c_7 \Delta\zeta_{i(b-1)} + c_8 \Delta\zeta_{(i+1)(b-1)} + c_9 \Delta\zeta_{(i+2)(b-1)} + \\ & c_{10} \Delta\zeta_{(I-1)B} + c_{11} \Delta\zeta_{(i-1)b} + c_{12} \Delta\zeta_{(i+3)b)} + B + C \big]\end{aligned} \tag{A.11}$$

with

$$
\begin{aligned}
c_1 &= 0.5b^x_{(i+1)b} - 1.5b^x_{ib} + 0.5a^y_{IB} - 0.5b^y_{(I+1)B} \\
c_2 &= 1.5b^x_{(i+1)b} - 0.5b^x_{ib} + 0.5b^y_{IB} + 0.5a^y_{(I+1)B} \\
c_3 &= 0.5b^y_{(I+1)B} \\
c_4 &= b^y_{(i+1)b} + a^x_{ib} - 0.5a^y_{IB} \\
c_5 &= a^x_{(i+1)b} + a^x_{ib} + a^y_{(i+1)b} + 0.5b^y_{(I+1)B} - 0.5b^y_{IB} \\
c_6 &= a^x_{(i+1)b} - 0.5a^y_{(I+1)B} - b^y_{(i+1)b} \\
c_7 &= b^y_{(i+1)b} + b^x_{ib} \\
c_8 &= a^y_{(i+1)b} - b^x_{(i+1)b} + b^x_{ib} \\
c_9 &= -b^x_{(i+1)b} - b^y_{(i+1)b} \\
c_{10} &= -0.5b^y_{IB} \\
c_{11} &= -0.5b^y_{IB} \\
c_{12} &= 0.5b^y_{(I+1)B}
\end{aligned}
$$

$$
C = \frac{\Delta t}{2a\cos_u\phi_b}\left[\frac{\widehat{U}_{ib} - \widehat{U}_{(i+1)b}}{\Delta\lambda} + \frac{\widehat{V}_{(i+1)b}\cos_v\phi_j - 0.5(\widehat{V}_{IB} + \widehat{V}_{(I+1)B})\cos_v\phi_{(j+1)}}{\Delta\phi}\right].
$$

For the first latitude of the lower zonal resolution $B$, the iteration problem becomes:

$$
\begin{aligned}
\Delta\zeta_{IB} = \frac{1}{1+c_5}\cdot\big[&c_1\Delta\zeta_{(I-1)(B+1)} + c_2\Delta\zeta_{I(B+1)} + c_3\Delta\zeta_{(I+1)(B+1)} + c_4\Delta\zeta_{(I-1)B} + \\
&c_6\Delta\zeta_{(I+1)B} + c_7\Delta\zeta_{(i-1)b} + c_8\Delta\zeta_{ib} + c_9\Delta\zeta_{(i+1)b} + B + C\big]
\end{aligned} \tag{A.12}
$$

with

$$
\begin{aligned}
c_1 &= -b^x_{(I-1)B} - b^y_{I(B+1)} \\
c_2 &= -b^x_{(I-1)B} + b^x_{IB} + a^y_{I(B+1)} \\
c_3 &= b^y_{I(B+1)} + b^x_{IB} \\
c_4 &= b^y_{IB} + a^x_{(I-1)B} - b^y_{I(B+1)} \\
c_5 &= a^x_{IB} + a^x_{(I-1)B} + a^y_{IB} + a^y_{I(B+1)} \\
c_6 &= a^x_{IB} + b^y_{I(B+1)} - b^y_{IB} \\
c_7 &= b^y_{IB} + 2b^x_{(I-1)B} \\
c_8 &= a^y_{IB} \\
c_9 &= -2b^x_{IB} - b^y_{IB}
\end{aligned}
$$

$$
C = \frac{\Delta t}{2a\cos_u\phi_b}\left[\frac{\widehat{U}_{(I-1)B} - \widehat{U}_{IB}}{2\Delta\lambda} + \frac{\widehat{V}_{IB}\cos_v\phi_j - \widehat{V}_{I(B+1)}\cos_v\phi_{(j+1)}}{\Delta\phi}\right].
$$

### A.1.3 Polar Cap

The North Pole is represented by a polar cap with the elevation $\zeta_P$ and the radius $\Delta\phi_c$ reaching until a latitude with index $p$. This alters the pressure gradient terms $P^x_{i(p-1)}$ and $P^y_{ip}$ in the equations of motion.

$$
\begin{aligned}
P^x_{i(p-1)} &= \frac{g'}{fa}\left[\frac{\beta\left(\zeta^{(1/2)}_{(i+1)(p-1)} - \zeta^{(1/2)}_{i(p-1)}\right)}{\Delta\lambda\cos_u\phi_{(p-1)}} + \frac{\gamma\left(2\zeta^{(1/2)}_P - \zeta^{(1/2)}_{i(p-2)} - \zeta^{(1/2)}_{(i+1)(p-2)}\right)}{2(\Delta\phi + \Delta\phi_c)}\right] \\
P^y_{ip} &= \frac{g'}{fa}\left[\frac{\beta\left(\zeta^{(1/2)}_P - \zeta^{(1/2)}_{i(p-1)}\right)}{\Delta\phi_c} - \frac{\gamma\left(\zeta^{(1/2)}_{(i+1)(p-1)} - \zeta^{(1/2)}_{(i-1)(p-1)}\right)}{4\Delta\lambda\cos_v\phi_p}\right]
\end{aligned}
$$

The equations of continuity read:

$$
\zeta^{n+1}_{i(p-1)} = \zeta^n_{i(p-1)} - \frac{\Delta t}{a\cos_u\phi_{(p-1)}}\left[\frac{U^{(1/2)}_{i(p-1)} - U^{(1/2)}_{(i-1)(p-1)}}{\Delta\lambda} + \frac{V^{(1/2)}_{ip}\cos_v\phi_p - V^{(1/2)}_{i(p-1)}\cos_v\phi_{(p-1)}}{0.5(\Delta\phi + \Delta\phi_c)}\right]
$$

$$
\zeta^{n+1}_P = \zeta^n_P - \frac{\Delta t S}{A}\sum_i V^{(1/2)}_{ip}
$$

with $S = a\sin(\Delta\phi_c)\Delta\lambda$ and $A = 2\pi a^2(1 - \cos(\Delta\phi_c))$. The iteration problem for the northernmost latitude $p-1$ is solved through:

$$
\begin{aligned}
\Delta\zeta_{i(p-1)} = \frac{1}{1+c_5}\cdot\big[&c_2\Delta\zeta_P + c_4\Delta\zeta_{(i-1)(p-1)} + c_6\Delta\zeta_{(i+1)(p-1)} + \\
&c_7\Delta\zeta_{(i-1)(p-2)} + c_8\Delta\zeta_{i(p-2)} + c_9\Delta\zeta_{(i+1)(p-2)} + B + C\big]
\end{aligned}
\tag{A.13}
$$

with

$$
C = \frac{\Delta t}{a\cos_u\phi_{(p-1)}}\left[\frac{\widehat{U}_{(i-1)(p-1)} - \widehat{U}_{i(p-1)}}{2\Delta\lambda} + \frac{\widehat{V}_{i(p-1)}\cos_v\phi_{(p-1)} - \widehat{V}_{ip}\cos_v\phi_{(p)}}{\Delta\phi + \Delta\phi_c}\right]
$$

$$
\begin{aligned}
c_2 &= -2b^x_{(i-1)(p-1)} + 2b^x_{i(p-1)} + a^y_{ip} \\
c_4 &= b^y_{i(p-1)} + a^x_{(i-1)(p-1)} - b^y_{ip} \\
c_5 &= a^x_{i(p-1)} + a^x_{(i-1)(p-1)} + a^y_{i(p-1)} + a^y_{ip} \\
c_6 &= a^x_{i(p-1)} + b^y_{ip} - b^y_{i(p-1)} \\
c_7 &= b^y_{i(p-1)} + b^x_{(i-1)(p-1)} \\
c_8 &= a^y_{i(p-1)} - b^x_{i(p-1)} + b^x_{(i-1)(p-1)} \\
c_9 &= -b^x_{i(p-1)} - b^y_{i(p-1)}
\end{aligned}
$$

The polar cap is formulated as:

$$\Delta\zeta_P = \frac{1}{1+c_5}\sum_i \left[c_7\Delta\zeta_{(i-1)(p-1)} + c_8\Delta\zeta_{(p-1)} + c_9\Delta\zeta_{(i+1)(p-1)}\right] + B + C \tag{A.14}$$

with

$$C = \frac{\Delta t S}{2A}\sum_i \widehat{V}_{ip}$$

$$\begin{aligned} c_5 &= \sum_i a^y_{ip} \\ c_7 &= b^y_{ip} \\ c_8 &= a^y_{ip} \\ c_9 &= -b^y_{ip}. \end{aligned}$$

## A.2 Partial Tides

Table A.1: Partial Tides Extracted from Real-Time Simulations.

| Tide | Coefficient $k_{pt}$ | Doodson Number | Argument $t$ | $s$ | $h$ | $p$ | $p_s$ | $N$ | $\phi$ | Frequency $\sigma_{pt}$ [°/hour] | Origin1) |
|---|---|---|---|---|---|---|---|---|---|---|---|
| $Sa$ | 0.01176 | 056 554 | 0 | 0 | 1 | 0 | -1 | 0 | 0 | 0.041067 | S |
| $Ssa$ | 0.07287 | 057 555 | 0 | 0 | 2 | 0 | 0 | 0 | 0 | 0.082137 | S |
| $MSm$ | 0.01587 | 063 655 | 0 | 1 | -2 | 1 | 0 | 0 | 0 | 0.471521 | M |
| $Mm$ | 0.08254 | 065 455 | 0 | 1 | 0 | -1 | 0 | 0 | 0 | 0.544375 | M |
| $MSf$ | 0.01370 | 073 555 | 0 | 2 | -2 | 0 | 0 | 0 | 0 | 1.015896 | M |
| $Mf$ | 0.15642 | 075 555 | 0 | 2 | 0 | 0 | 0 | 0 | 0 | 1.098033 | M |
| $Q_1$ | 0.07216 | 135 655 | 1 | -3 | 1 | 1 | 0 | 0 | -90° | 13.398661 | M |
| $O_1$ | 0.37689 | 145 555 | 1 | -2 | 1 | 0 | 0 | 0 | -90° | 13.943036 | M |
| $P_1$ | 0.17554 | 163 555 | 1 | 0 | 1 | 0 | 0 | 0 | -90° | 14.958931 | S |
| $K_{1m}$ | 0.36233 | 165 555 | 1 | 0 | 1 | 0 | 0 | 0 | +90° | 15.041069 | M |
| $K_{1s}$ | 0.16817 | 165 555 | 1 | 0 | 1 | 0 | 0 | 0 | +90° | 15.041069 | S |
| $2N_2$ | 0.02301 | 235 755 | 2 | -4 | 2 | 2 | 0 | 0 | 0 | 27.895355 | M |
| $\mu_2$ | 0.02777 | 237 555 | 2 | -4 | 4 | 0 | 0 | 0 | 0 | 27.968208 | M |
| $N_2$ | 0.17387 | 245 655 | 2 | -3 | 2 | 1 | 0 | 0 | 0 | 28.439730 | M |
| $M_2$ | 0.90812 | 255 555 | 2 | -2 | 2 | 0 | 0 | 0 | 0 | 28.984104 | M |
| $L_2$ | 0.02567 | 265 455 | 2 | -1 | 2 | -1 | 0 | 0 | +180° | 29.528479 | M |
| $T_2$ | 0.02479 | 272 556 | 2 | 0 | -1 | 0 | 1 | 0 | 0 | 29.958933 | S |
| $S_2$ | 0.42286 | 273 555 | 2 | 0 | 0 | 0 | 0 | 0 | 0 | 30.000000 | S |
| $S_{2m}$ | 0.00072 | 273 555 | 2 | 0 | 0 | 0 | 0 | 0 | 0 | 30.000000 | M |
| $K_{2m}$ | 0.07858 | 275 555 | 2 | 0 | 2 | 0 | 0 | 0 | 0 | 30.082137 | M |
| $K_{2s}$ | 0.03648 | 275 555 | 2 | 0 | 2 | 0 | 0 | 0 | 0 | 30.082137 | S |
| $\eta_2$ | 0.00643 | 285 455 | 2 | 1 | 2 | -1 | 0 | 0 | 0 | 30.626512 | M |
| $2SM_2$ | - | 291 555 | 2 | 2 | -2 | 0 | 0 | 0 | 0 | 31.015896 | $2 \times S_2 - M_2$ |
| $MO_3$ | - | 345 555 | 3 | -4 | 3 | 0 | 0 | 0 | -90° | 42.927140 | $M_2 + O_1$ |
| $SO_3$ | - | 363 555 | 3 | -2 | 1 | 0 | 0 | 0 | -90° | 43.943036 | $S_2 + O_1$ |
| $MK_3$ | - | 365 555 | 3 | -2 | 3 | 0 | 0 | 0 | +90° | 44.025173 | $M_2 + K_1$ |
| $MN_4$ | - | 445 655 | 4 | -5 | 4 | 1 | 0 | 0 | 0 | 57.423834 | $M_2 + N_2$ |
| $M_4$ | - | 455 555 | 4 | -4 | 4 | 0 | 0 | 0 | 0 | 57.968208 | $2 \times M_2$ |
| $MS_4$ | - | 473 555 | 4 | -2 | 2 | 0 | 0 | 0 | 0 | 58.984104 | $M_2 + S_2$ |
| $MK_4$ | - | 475 555 | 4 | -2 | 4 | 0 | 0 | 0 | 0 | 59.066242 | $M_2 + K_2$ |
| $M_6$ | - | 655 555 | 6 | -6 | 6 | 0 | 0 | 0 | 0 | 86.952313 | $3 \times M_2$ |
| $2MS_6$ | - | 673 555 | 6 | -4 | 4 | 0 | 0 | 0 | 0 | 87.968208 | $2 \times M_2 + S_2$ |
| $2MK_6$ | - | 675 555 | 6 | -4 | 6 | 0 | 0 | 0 | 0 | 88.050346 | $2 \times M_2 + K_2$ |
| $M_8$ | - | 855 555 | 8 | -8 | 8 | 0 | 0 | 0 | 0 | 115.936417 | $4 \times M_2$ |
| $3MS_8$ | - | 873 555 | 8 | -6 | 6 | 0 | 0 | 0 | 0 | 116.952313 | $3 \times M_2 + S_2$ |
| $3MK_8$ | - | 875 555 | 8 | -6 | 8 | 0 | 0 | 0 | 0 | 117.034450 | $3 \times M_2 + K_2$ |

1) Solar (S) or lunar (M) tidal potential; for shallow-water tides: the combination of astronomical partial tides.

Table A.2: Additional Partial Tides.

|  | Coefficient | Doodson |  |  |  | Argument |  |  |  | Frequency |  |
|---|---|---|---|---|---|---|---|---|---|---|---|
| Tide | $k_{pt}$ | Number | $t$ | $s$ | $h$ | $p$ | $p_s$ | $N$ | $\phi$ | $\sigma_{pt}$ [°/hour] | Origin[1] |
| $Sta$ | 0.00427 | 058 554 | 0 | 0 | 3 | 0 | -1 | 0 | 0 | 0.123204 | S |
| $mf$ | 0.06481 | 075 565 | 0 | 2 | 0 | 0 | 0 | -1 | 0 | 1.100240 | M |
| $MStm$ | 0.00569 | 083 655 | 0 | 3 | -2 | 1 | 0 | 0 | 0 | 1.569554 | M |
| $Mtm$ | 0.02995 | 085 455 | 0 | 3 | 0 | -1 | 0 | 0 | 0 | 1.642408 | M |
| $mtm$ | 0.01241 | 085 465 | 0 | 3 | 0 | -1 | 0 | -1 | 0 | 1.644614 | M |
| $MSqm$ | 0.00478 | 093 555 | 0 | 4 | -2 | 0 | 0 | 0 | 0 | 2.113929 | M |
| $2Q_1$ | 0.00955 | 125 755 | 1 | -4 | 1 | 2 | 0 | 0 | -90° | 12.854286 | M |
| $\sigma_1$ | 0.01153 | 127 555 | 1 | -4 | 3 | 0 | 0 | 0 | -90° | 12.927140 | M |
| $q_1$ | 0.01360 | 135 645 | 1 | -3 | 1 | 1 | 0 | 1 | -90° | 13.396455 | M |
| $\rho_1$ | 0.01371 | 137 455 | 1 | -3 | 3 | -1 | 0 | 0 | -90° | 13.471514 | M |
| $o_1$ | 0.07105 | 145 545 | 1 | -2 | 1 | 0 | 0 | 1 | -90° | 13.940830 | M |
| $\tau_1$ | 0.00491 | 147 555 | 1 | -2 | 3 | 0 | 0 | 0 | +90° | 14.025173 | M |
| $o'_1$ | 0.01065 | 155 455 | 1 | -1 | 1 | -1 | 0 | 0 | +90° | 14.487410 | M |
| $M_1$ | 0.02964 | 155 655 | 1 | -1 | 1 | 1 | 0 | 0 | +90° | 14.496694 | M |
| $\chi_1$ | 0.00566 | 157 455 | 1 | -1 | 3 | -1 | 0 | 0 | +90° | 14.569548 | M |
| $\pi_1$ | 0.01029 | 162 556 | 1 | 0 | -2 | 0 | 1 | 0 | -90° | 14.917865 | S |
| $S_1$ | 0.00423 | 164 556 | 1 | 0 | 0 | 0 | -1 | 0 | +90° | 15.000002 | S |
| $k_{1m}$ | 0.07182 | 165 565 | 1 | 0 | 1 | 0 | 0 | -1 | +90° | 15.043275 | M |
| $\psi_1$ | 0.00423 | 166 554 | 1 | 0 | 2 | 0 | -1 | 0 | +90° | 15.082135 | S |
| $\phi_1$ | 0.00756 | 167 555 | 1 | 0 | 3 | 0 | 0 | 0 | +90° | 15.123206 | S |
| $\vartheta_1$ | 0.00566 | 173 655 | 1 | 1 | -1 | 1 | 0 | 0 | +90° | 15.512590 | M |
| $J_1$ | 0.02964 | 175 455 | 1 | 1 | 1 | -1 | 0 | 0 | +90° | 15.585443 | M |
| $SO_1$ | 0.00492 | 183 555 | 1 | 2 | -1 | 0 | 0 | 0 | +90° | 16.056964 | M |
| $OO_1$ | 0.01623 | 185 555 | 1 | 2 | 1 | 0 | 0 | 0 | +90° | 16.139102 | M |
| $oo_1$ | 0.01039 | 185 565 | 1 | 2 | 1 | 0 | 0 | -1 | +90° | 16.141308 | M |
| $\nu_1$ | 0.00311 | 195 455 | 1 | 3 | 1 | -1 | 0 | 0 | +90° | 16.683476 | M |
| $3N_2$ | 0.00259 | 225 855 | 2 | -5 | 2 | 3 | 0 | 0 | 0 | 27.350980 | M |
| $\epsilon_2$ | 0.00671 | 227 655 | 2 | -5 | 4 | 1 | 0 | 0 | 0 | 27.423834 | M |
| $\nu_2$ | 0.03303 | 247 455 | 2 | -3 | 4 | -1 | 0 | 0 | 0 | 28.512583 | M |
| $\gamma_2$ | 0.00273 | 253 755 | 2 | -2 | 0 | 2 | 0 | 0 | +180° | 28.911251 | M |
| $\alpha_2$ | 0.00314 | 254 556 | 2 | -2 | 1 | 0 | 1 | 0 | +180° | 28.943038 | M |
| $m_2$ | 0.03386 | 255 545 | 2 | -2 | 2 | 0 | 0 | 1 | +180° | 28.981898 | M |
| $\beta_2$ | 0.00276 | 256 554 | 2 | -2 | 3 | 0 | -1 | 0 | 0 | 29.025171 | M |
| $\delta_2$ | 0.00107 | 257 555 | 2 | -2 | 4 | 0 | 0 | 0 | 0 | 29.066242 | M |
| $\lambda_2$ | 0.00670 | 263 655 | 2 | -1 | 0 | 1 | 0 | 0 | +180° | 29.455625 | M |
| $k_{2m}$ | 0.00643 | 265 655 | 2 | -1 | 2 | 1 | 0 | 0 | 0 | 29.537763 | M |
| $2T_2$ | 0.00101 | 271 557 | 2 | 0 | -2 | 0 | 2 | 0 | 0 | 29.917866 | S |
| $R_2$ | 0.00354 | 274 554* | 2 | 0 | 1 | 0 | -1 | 0 | +180°* | 30.041067 | S |
| $k'_{2m}$ | 0.03423 | 275 565 | 2 | 0 | 2 | 0 | 0 | -1 | 0 | 30.084343 | M |
| $\zeta_2$ | 0.00123 | 283 655 | 2 | 1 | 0 | 1 | 0 | 0 | 0 | 30.553656 | M |
| $k''_{2m}$ | 0.00168 | 295 555 | 2 | 2 | 2 | 0 | 0 | 0 | 0 | 31.180170 | M |
| $MQ_3$ | - | 335 655 | 3 | -5 | 3 | 1 | 0 | 0 | -90° | 42.382765 | $M_2 + Q_1$ |
| $SP_3$ | - | 381 555 | 3 | 0 | -1 | 0 | 0 | 0 | -90° | 44.958931 | $S_2 + P_1$ |
| $SK_3$ | - | 383 555 | 3 | 0 | 1 | 0 | 0 | 0 | +90° | 45.041069 | $M_2 + K_1$ |
| $K_3$ | - | 385 555 | 3 | 0 | 3 | 0 | 0 | 0 | +90° | 45.123206 | $K_2 + K_1$ |
| $3MS_4$ | - | 437 555 | 4 | -6 | 6 | 0 | 0 | 0 | 0 | 56.952313 | $3 \times M_2 - S_2$ |
| $SN_4$ | - | 463 655 | 4 | -3 | 2 | 1 | 0 | 0 | 0 | 58.439730 | $S_2 - N_2$ |
| $3MN_4$ | - | 465 455 | 4 | -3 | 4 | -1 | 0 | 0 | 0 | 58.512583 | $3 \times M_2 - N_2$ |
| $S_4$ | - | 491 555 | 4 | 0 | 0 | 0 | 0 | 0 | 0 | 60.000000 | $2 \times S_2$ |
| $2MN_6$ | - | 645 655 | 6 | -7 | 6 | 1 | 0 | 0 | 0 | 86.407938 | $2 \times M_2 + N_2$ |
| $MSN_6$ | - | 663 655 | 6 | -5 | 4 | 1 | 0 | 0 | 0 | 87.423834 | $M_2 + S_2 + N_2$ |
| $MNK_6$ | - | 665 655 | 6 | -5 | 6 | 1 | 0 | 0 | 0 | 87.505971 | $M_2 + N_2 + K_2$ |
| $2SM_6$ | - | 691 555 | 6 | -2 | 2 | 0 | 0 | 0 | 0 | 88.984104 | $2 \times S_2 + M_2$ |
| $MSK_6$ | - | 693 555 | 6 | -2 | 4 | 0 | 0 | 0 | 0 | 89.066242 | $M_2 + S_2 + K_2$ |
| $3MN_8$ | - | 845 655 | 8 | -9 | 8 | 1 | 0 | 0 | 0 | 115.392042 | $3 \times M_2 + N_2$ |
| $2MSN_8$ | - | 863 655 | 8 | -7 | 6 | 1 | 0 | 0 | 0 | 116.407938 | $2 \times M_2 + S_2 + N_2$ |
| $2MNK_8$ | - | 865 655 | 8 | -7 | 8 | 1 | 0 | 0 | 0 | 116.490075 | $2 \times M_2 + N_2 + K_2$ |
| $2(MS)_8$ | - | 891 555 | 8 | -4 | 4 | 0 | 0 | 0 | 0 | 117.968208 | $2 \times M_2 + 2 \times S_2$ |
| $2MSK_8$ | - | 893 555 | 8 | -4 | 6 | 0 | 0 | 0 | 0 | 118.050316 | $2 \times M_2 + S_2 + K_2$ |

---

[1] Solar (S) or lunar (M) tidal potential; for shallow-water tides: the combination of astronomical partial tides.

## A.3 Additional Shallow-Water Tides

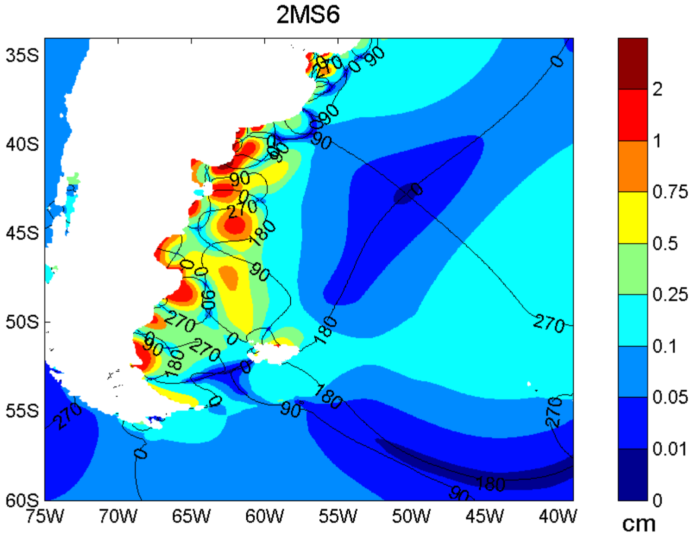

Figure A.1: Amplitudes and phases of the $2MS_6$ on the Patagonian Shelf.

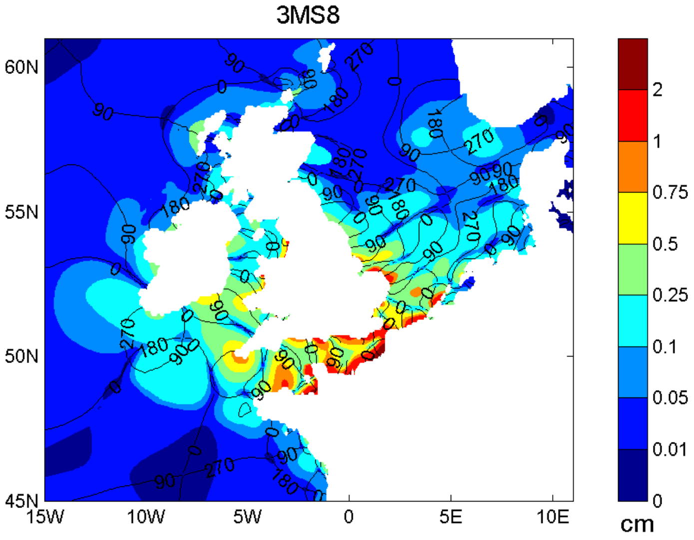

Figure A.2: Amplitudes and phases of the $3MS_8$ in the North Sea area.

## A.4 Notation of ERP

In Section 5.4 the results of this study where compared to measurements and shown as amplitudes and phases. The cited measurement studies, however, usually present results as cosine- and sine-values, i.e. as $cos_{pt} = A_{pt} \cdot \cos\phi_{pt}$ and $sin_{pt} = A_{pt} \cdot \sin\phi_{pt}$. For this study, the values have been recalculated to be presented in the amplitude/phase-notation. Values in $cos_{pt}$ and $sin_{pt}$ of value 0 have been omitted. The amplitudes are obtained through

$$A_{pt} = \sqrt{cos_{pt}^2 + sin_{pt}^2} \tag{A.15}$$

and the phases by

$$\phi_{pt} = tan^{-1}\left(cos_{pt} + sin_{pt}\right) + \phi_a \tag{A.16}$$

where $\phi_a$ refers to the $\phi$ in the argument of the given partial tides listed in Tables A.1 and A.2. Furthermore, phase values for both prograde and retrograde polar motion of the semi-diurnal tides listed in Herring and Dong (1994), Gipson (1996) and Rothacher et al. (1998) had to be corrected by $180°$.

Gipson (1996) describes the transformation of Doodson variables (normally used in ocean tide studies) into Woolard arguments (normally used in measurement studies). Performing this conversion revealed that the diurnal tide $N_1$ referred to in Gipson (1996) and Rothacher et al. (1998) is identical with the partial tide $\pi_1$ in Bartels (1957) and this study. The same holds for $\eta_1$ which is called $\nu_1$ in their study. It also helped labelling the partial tides in Herring and Dong (1994) which have not been specificly labelled.

# List of Figures

# List of Tables

# Bibliography

Accad, Y. and Pekeris, C.: Solution of the tidal equations for the $M_2$ and $S_2$ tides in the world oceans from a knowledge of the tidal potential alone, Phil. Trans. Roy. Soc. London, pp. 235–266, 1978.

Andersen, O.: Shallow water tides in the northwest European shelf region from TOPEX/POSEIDON altimetry, Journ. of Geoph. Res., 104, 7,729–7,741, 1999.

Arakawa, A. and Lamb, V.: Computational design of the basic dynamical processes of the UCLA General Circulation Model, Methods in Computational Physics, pp. 174–265, 1977.

Backhaus, J.: A semi-implicit scheme for the shallow water equations for application to shelf sea modeling, Cont. Sh. Res., pp. 243–254, 1983.

Backhaus, J.: A three-dimensional model for the simulation of the shelf sea dynamics, Dt. hydrogr. Z., pp. 165–187, 1985.

Barnes, R., Hide, R., White, A., and Wilson, C.: Atmospheric angular momentum fluctuations, length-of-day changes and polar motion, Proc. R. Soc. London, Ser. A, 363–380, 1983.

Bartels, J.: Gezeitenkräfte, Handbuch der Physik, Band XLVIII, Geophysik II, 1957.

Cartwright, D., Zetler, B., and Hamon, B.: Pelagic tidal constants, IAPSO Publ. Scient., 30, 1979.

Chao, B. and Ray, R.: Oceanic tidal angular momentum and Earth's rotation variations, Prog. Oceanog., 40, 399–421, 1997.

Chapront, J., Chapront-Touzé, M., and Francou, G.: A new determination of lunar orbital parameters, precession constant and tidal acceleration from LLR measurements, Astron. and Astroph., 387, 700–709, 2002.

Desai, S.: Ocean tides from TOPEX/POSEIDON altimetry with some geophysical applications, PhD thesis, Univ. of Colorado, 1996.

Egbert, G. and Ray, R.: Significant dissipation of tidal energy in the deep ocean inferred from satellite altimeter data, Nature, 405, 775–778, 2000.

Egbert, G., Bennett, A., and Foreman, M.: TOPEX/POSEIDON tides estimated using a global inverse model, Journ. of Geoph. Res., 99, 24,821–24,852, 1994.

Egbert, G., Ray, R., and Bills, B. G.: Numerical Modeling of the global semidiurnal tide in the present day and in the last glacial maximum, Journ. of Geoph. Res., 109, C03 003, doi:10.1029/2003JC001 973, 2004.

Emery, W. and Thompson, R.: Data analysis methods in physical oceanography, Pergamon Press, p. 634, 1998.

Gipson, J.: VLBI determination of neglected terms in high-frequency Earth orientation parameter variation, J. of Heoph. Res., 101, 28,051–28,064, 1996.

Gross, R.: The effect of ocean tides on the earth's rotation as predicted by the results of an ocean tide model, Geoph. Res. Letters, 20, 293–296, 1993.

Gross, R., Chao, B., and Desai, S.: Effect of long-period ocean tides on the Earth's polar motion, Prog. Oceanog., 40, 385–397, 1997.

Haas, R. and Wünsch, J.: Sub-diurnal earth rotation variations from the VLBI CONT02 campaign, Journ. of Geodyn., 41, 94–99, 2006.

Hellmich, A.: Ein rechenökonomisches Modul für ephemeridische Gezeitensimulationen, Diplomarbeit, TU Dresden, 2003.

Herring, T. and Dong, D.: Measurement of diurnal and semidiurnal rotational variations and tidal parameters of Earth, J. of Geoph. Res., 99, 18,051–18,071, 1994.

Hufschmidt, A.: Berechnung des Auflast- und Eigenanziehungspotentials in einem globalen Gezeitenmodell und Auswirkungen auf die Energiebilanz, Dissertation, Univ. of Hamburg, 1995.

IOC, IHO, and BODC: Centenary Edition of the GEBCO Digital Atlas, published on CD-ROM on behalf of the Intergovernmental Oceanographic Commission and the International Hydrographic Organization as part of the General Bathymetric Chart of the Oceans, British Oceanographic Data Centre, Liverpool, U.K., 2003.

Jayne, S. and St. Laurent, L.: Parameterizing tidal dissipation over rough topography, Geoph. Res. Let., 28, 811–814, 2001.

Kagan, B. A. and Sündermann, J.: Dissipation of tidal energy, paleotides, and the evolution of the earth-moon system, Adv. Geophys., 38, 179–266, 1996.

Kantha, L., Stewart, J., and Desai, S.: Long-period lunar fortnightly and monthly ocean tides, Journ. of Geoph. Res., 103, 12,639–12,647, 1998.

Le Provost, C.: A new sea truth data set for tides, ftp://meolipc.img.fr/pub/ST103, 1995.

Montenbruck, O.: Grundlagen der Ephemeridenberechnung, Verlag Sterne im Weltraum, 1987.

Müller, M.: Barotrope Eigenschwingungen im globalen Ozean unter Berücksichtigung des vollen Selbstanziehungs- und Auflasteffektes, Diplomarbeit, Univ. Hamburg, 2003.

Müller, M.: The full ocean loading and self attraction effect on the free oscillations of a barotropic ocean model, Geoph. Res. Let., in review.

Munk, W. and MacDonald, G.: The rotation of the earth, Cam. Univ. Press, New York, p. 323, 1960.

Nastula, J., Kolaczek, B., Weber, R., Boehm, J., and Schuh, H.: High resolution earth rotation parameters determined during the CONT02 campaign, IVS 2004 General Meeting Proceedings, pp. 408–412, 2004.

Newhall, X. X., Williams, J., and Dickey, J.: Tidal acceleration of the Moon, In: Brosche, P. and Sündermann, J. (Eds.): Earth's Rotation from Eons to Days, Springer Verlag, p. 51, 1990.

NOAA: Data Announcement 88-MGG-02, Digital relief of the Surface of the Earth, NOAA, National Geophysical Data Center, Boulder, Colorado, 1988.

Parke, M.: $O_1$, $P_1$, $N_2$ models of the global ocean tide on an elastic earth plus surface potential and spherical harmonic decompositions for $M_2$, $S_2$ and $K_1$, Mar. Geod., 6, 35–81, 1982.

Pohlmann, T.: Predicting the thermocline in a circulation model of the North Sea. Part I: model description, calibration, and verification, Cont. Shelf Res., pp. 131–146, 1996.

Pond, S. and Pickard, G. L.: Introductory Dynamical Oceanography (2nd edition), Pergamon Press, 1983.

Press, W., Flannery, B., and Teukolsky, S.: Numerical Recipes : The Art of Scientific Computing, Cambridge Univ. Pr., p. 818, 1987.

Richter, B.: Die Parametrisierung der Erdorientierung, Zeitschr. f. Vermessungswesen, 102, 109–119, 1995.

Rothacher, M., Beutler, G., Weber, R., and Hefty, J.: High-frequency variations in Earth rotation from Global Positioning System data, Journ. of Geoph. Res., 106, 13,711–13,738, 1998.

Schwiderski, E.: Global Ocean Tides, Part VII: The diurnal principal solar tide ($P_1$), NSWC TR 81 220, Dahlgren Virginia, 1981.

Seiler, U.: An investigation to the tides of the world ocean and their instantaneous angular momentum budgets, Mitt. Inst. Meeresk., Univ. Hamburg, 1989.

Seiler, U.: Periodic changes of the angular momentum budget due to the tides of the world ocean, Journ. of Geophys. Res., 96, 10,287–10,300, 1991.

Seitz, F.: Atmosphärische und ozeanische Einflüsse auf die Rotation der Erde - Numerische Untersuchungen mit einem dynamischen Erdsystemmodell, Diss. TU München, 2004.

Shum, C.: Accuracy assessment of recent ocean tide models, Journ. of. Geoph. Res., 102, 25,173–25,194, 1997.

Sovers, O., Jacobs, C., and Gross, R.: Measuring rapid ocean tidal Earth orientation variations with VLBI, Journ. of Geophys. Res., 98, 19,959–19,971, 1993.

Stephenson, F.: Pre-Telescopic Astronomical Observations, In: Brosche, P. and Sündermann, J. (Eds.): Tidal Friction and the Earth's Rotation, Springer Verlag, pp. 5–20, 1978.

Struve, O.: Astronomie. Einführung in ihre Grundlagen, De Gryuter, Berlin, 1962.

Sündermann, J. and Brosche, P.: Numerical Computation of Tidal Friction for Present and Ancient Oceans, In: Brosche, P. and Sündermann, J. (Eds.): Tidal Friction and the Earth's Rotation, Springer Verlag, pp. 125–144, 1978.

Thomas, M.: Gezeiten und Drehimpuls im Ozean während der letzten 21000 Jahre, Diplomarbeit, Univ. of Hamburg, 1996.

Thomas, M.: Ozeanisch induzierte Erdrotationsschwankungen - Ergebnisse eines Simultanmodells für Zirkulation und ephemeridische Gezeiten im Weltozean, Ph.D. Dissertation, Univ. of Hamburg, p. 129, 2001.

Wahr, J.: The effects of the atmosphere and the oceans on the earth's wobble - I theory, Geophys. J. R. Astron. Soc., pp. 451–487, 1982.

Walters, R., Goring, D., and Bell, R.: Ocean tides around New Zealand, New Zealand J. of Mar. and Freshw. Res., 35, 567–579, 2001.

Wilson, C. and Vicente, R.: An analysis of the homogeneous ILS polar motion series, Geophys. J. R. Astron. Soc., pp. 605–616, 1980.

Zahel, W.: Die Reproduktion gezeitenbedingter Bewegungsvorgänge im Weltozean mittels des hydrodynamisch-numerischen Verfahrens, Mitt. Inst. Meersk., Univ. Hamburg, 17, 1970.

Zahel, W.: A global hydrodynamic-numerical 1°-model of the ocean-tides; the oscillation system of the $M_2$-tide and its distribution of energy dissipation, Ann. Geophys., pp. 31–40, 1977.

Zahel, W.: The influence of solid Earth deformations on semidiurnal and diurnal ocean tides, In: Brosche P., Sündermann J. (Eds.), Tidal friction and the Earth's rotation, Springer Verlag, Berlin-Heidelberg-New York, pp. 98–124, 1978.

Zahel, W.: Assimilating ocean tide determined data into global tidal models, J. Mar. Syst., 6, 3–13, 1995.

Zahel, W. and Müller, M.: The computation of the free barotropic oscillations of a global ocean model including friction and loading effects, Ocean. Dyn., 55, 137–161, 2005.

Zahel, W., Gaviño, J., and Seiler, U.: Balances de Energía y Momento Angular de un Modelo Global de Mareas con Asimilacíon de Datos, GEOS, 20, 400–413, 2000.

Zharkov, V., Molodensky, S., Brzezinski, A., Groten, E., and Varga, P.: The earth and its rotation, Wichmann Verlag, Heidelberg, p. 501, 1996.

# Acknowledgements

I would like to thank my supervisor Prof. Dr. Jürgen Sündermann and my scientific advisors Prof. Dr. Wilfried Zahel, Dr. Maik Thomas and Dr. Ernst Maier-Reimer for their supervision, inspiration and steady support of my work. I further thank Dr. Maik Thomas for providing me with the tool for the calculation of the lunisolar tidal potential and for a good time in Dresden, Hamburg and Beijing.

I am very grateful to my friends and colleagues Dr. Tatjana Ilyina and Melissa Anne Pfeffer who have accompanied me through this doctoral work. They have essentially turned my manuscript into a thesis.

Further corrections and/or many helpful discussions over the last years I further owe to Stiig Wilkenskjeld, Malte Müller, Dr. Ulrich Körner, PD Dr. Thomas Pohlmann, Dr. Ulrike Seiler, Francesca Guglielmo, Felix Landerer and Regina Wegner.

I am glad to have met so many interesting people at the International Max Planck Research School on Earth System Modelling, the Institute of Oceanography and the Max Planck Institute of Meteorology.

This work has been funded by the International Max Planck Research School on Earth System Modelling.

**Publikationsreihe des MPI-M**
**„Berichte zur Erdsystemforschung“ , „*Reports on Earth System Science*“, ISSN 1614-1199**
**Sie enthält wissenschaftliche und technische Beiträge, inklusive Dissertationen.**

| | |
|---|---|
| **Berichte zur**<br>**Erdsystemforschung Nr.1**<br>Juli 2004 | **Simulation of Low-Frequency Climate Variability in the North Atlantic Ocean and the Arctic**<br>Helmuth Haak |
| **Berichte zur**<br>**Erdsystemforschung Nr.2**<br>Juli 2004 | **Satellitenfernerkundung des Emissionsvermögens von Landoberflächen im Mikrowellenbereich**<br>Claudia Wunram |
| **Berichte zur**<br>**Erdsystemforschung Nr.3**<br>Juli 2004 | **A Multi-Actor Dynamic Integrated Assessment Model (MADIAM)**<br>Michael Weber |
| **Berichte zur**<br>**Erdsystemforschung Nr.4**<br>November 2004 | **The Impact of International Greenhouse Gas Emissions Reduction on Indonesia**<br>Armi Susandi |
| **Berichte zur**<br>**Erdsystemforschung Nr.5**<br>Januar 2005 | **Proceedings of the first HyCARE meeting, Hamburg, 16-17 December 2004**<br>Edited by Martin G. Schultz |
| **Berichte zur**<br>**Erdsystemforschung Nr.6**<br>Januar 2005 | **Mechanisms and Predictability of North Atlantic - European Climate**<br>Holger Pohlmann |
| **Berichte zur**<br>**Erdsystemforschung Nr.7**<br>November 2004 | **Interannual and Decadal Variability in the Air-Sea Exchange of CO2 - a Model Study**<br>Patrick Wetzel |
| **Berichte zur**<br>**Erdsystemforschung Nr.8**<br>Dezember 2004 | **Interannual Climate Variability in the Tropical Indian Ocean: A Study with a Hierarchy of Coupled General Circulation Models**<br>Astrid Baquero Bernal |
| **Berichte zur**<br>**Erdsystemforschung Nr9**<br>Februar 2005 | **Towards the Assessment of the Aerosol Radiative Effects, A Global Modelling Approach**<br>Philip Stier |
| **Berichte zur**<br>**Erdsystemforschung Nr.10**<br>März 2005 | **Validation of the hydrological cycle of ERA40**<br>Stefan Hagemann, Klaus Arpe and Lennart Bengtsson |
| **Berichte zur**<br>**Erdsystemforschung Nr.11**<br>Februar 2005 | **Tropical Pacific/Atlantic Climate Variability and the Subtropical-Tropical Cells**<br>Katja Lohmann |
| **Berichte zur**<br>**Erdsystemforschung Nr.12**<br>Juli 2005 | **Sea Ice Export through Fram Strait: Variability and Interactions with Climate**-<br>Torben Königk |
| **Berichte zur**<br>**Erdsystemforschung Nr.13**<br>August 2005 | **Global oceanic heat and fresh water forcing datasets based on ERA-40 and ERA-15**<br>Frank Röske |
| **Berichte zur**<br>**Erdsystemforschung Nr.14**<br>August 2005 | **The** HAM**burg** O**cean** C**arbon** C**ycle Model HAMOCC5.1 - Technical Description Release 1.1**<br>Ernst Maier-Reimer, Iris Kriest, Joachim Segschneider, Patrick Wetzel |
| **Berichte zur**<br>**Erdsystemforschung Nr.15**<br>Juli 2005 | **Long-range Atmospheric Transport and Total Environmental Fate of Persistent Organic Pollutants - A Study using a General Circulation Model**<br>Semeena Valiyaveetil Shamsudheen |

**Publikationsreihe des MPI-M**
**„Berichte zur Erdsystemforschung“ , „*Reports on Earth System Science*“, ISSN 1614-1199**
**Sie enthält wissenschaftliche und technische Beiträge, inklusive Dissertationen.**

| | |
|---|---|
| **Berichte zur Erdsystemforschung Nr.16**<br>Oktober 2005 | **Aerosol Indirect Effect in the Thermal Spectral Range as Seen from Satellites**<br>Abhay Devasthale |
| **Berichte zur Erdsystemforschung Nr.17**<br>Dezember 2005 | **Interactions between Climate and Land Cover Changes**<br>Xuefeng Cui |
| **Berichte zur Erdsystemforschung Nr.18**<br>**Januar 2006** | **Rauchpartikel in der Atmosphäre: Modellstudien am Beispiel indonesischer Brände**<br>Bärbel Langmann |
| **Berichte zur Erdsystemforschung Nr.19**<br>**Februar 2006** | **DMS cycle in the ocean-atmosphere system and its response to anthropogenic perturbations**<br>Silvia Kloster |
| **Berichte zur Erdsystemforschung Nr.20**<br>**Februar 2006** | **Held-Suarez Test with ECHAM5**<br>Hui Wan, Marco A. Giorgetta, Luca Bonaventura |
| **Berichte zur Erdsystemforschung Nr.21**<br>**Februar 2006** | **Assessing the Agricultural System and the Carbon Cycle under Climate Change in Europe using a Dynamic Global Vegetation Model**<br>Luca Criscuolo |
| **Berichte zur Erdsystemforschung Nr.22**<br>**März 2006** | **More accurate areal preciption over land and sea, APOLAS Abschlussbericht**<br>K. Bumke, M. Clemens, H. Graßl, S. Pang, G. Peters, J.E.E. Seltmann, T. Siebenborn, A. Wagner |
| **Berichte zur Erdsystemforschung Nr.23**<br>**März 2006** | **Modeling cold cloud processes with the regional climate model REMO**<br>Susanne Pfeifer |
| **Berichte zur Erdsystemforschung Nr.24**<br>**Mai 2006** | **Regional Modeling of Inorganic and Organic Aerosol Distribution and Climate Impact over Europe**<br>Elina Marmer |
| **Berichte zur Erdsystemforschung Nr.25**<br>**Mai 2006** | **Proceedings of the 2nd HyCARE meeting, Laxenburg, Austria, 19-20 Dec 2005**<br>Edited by Martin G. Schultz and Malte Schwoon |
| **Berichte zur Erdsystemforschung Nr.26**<br>**Juni 2006** | **The global agricultural land-use model KLUM – A coupling tool for integrated assessment**<br>Kerstin Ellen Ronneberger |
| **Berichte zur Erdsystemforschung Nr.27**<br>**Juli 2006** | **Long-term interactions between vegetation and climate -- Model simulations for past and future**<br>Guillaume Schurgers |
| **Berichte zur Erdsystemforschung Nr.28**<br>**Juli 2006** | **Global Wildland Fire Emission Modeling for Atmospheric Chemistry Studies**<br>Judith Johanna Hoelzemann |
| **Berichte zur Erdsystemforschung Nr.29**<br>**November 2006** | **$CO_2$ fluxes and concentration patterns over Eurosiberia: A study using terrestrial biosphere models and the regional atmosphere model REMO**<br>Caroline Narayan |

**Publikationsreihe des MPI-M**
**„Berichte zur Erdsystemforschung“ , „*Reports on Earth System Science*“, ISSN 1614-1199**
**Sie enthält wissenschaftliche und technische Beiträge, inklusive Dissertationen.**

| | |
|---|---|
| **Berichte zur<br>Erdsystemforschung Nr.30<br>November 2006** | **Long-term interactions between ice sheets and climate under anthropogenic greenhouse forcing<br>Simulations with two complex Earth System Models**<br>Miren Vizcaino |
| **Berichte zur<br>Erdsystemforschung Nr.31<br>November 2006** | **Effect of Daily Surface Flux Anomalies on the Time-Mean Oceanic Circulation**<br>Balan Sarojini Beena |
| **Berichte zur<br>Erdsystemforschung Nr.32<br>November 2006** | **Managing the Transition to Hydrogen and Fuel Cell Vehicles – Insights from Agent-based and Evolutionary Models –**<br>Malte Schwoon |
| **Berichte zur<br>Erdsystemforschung Nr.33<br>November 2006** | **Modeling the economic impacts<br>of changes in thermohaline circulation<br>with an emphasis on the Barents Sea fisheries**<br>Peter Michael Link |
| **Berichte zur<br>Erdsystemforschung Nr.34<br>November 2006** | **Indirect Aerosol Effects Observed from Space**<br>Olaf Krüger |
| **Berichte zur<br>Erdsystemforschung Nr.35<br>Dezember 2006** | **Climatological analysis of planetary wave propagation in Northern Hemisphere winter**<br>Qian Li |

ISSN 1614-1199